Distribution of petrogenic aromatic hydrocarbons across the seawater-ice-atmosphere interface

By

Katarzyna Polcwiartek

A Thesis submitted to the Faculty of Graduate and Postdoctoral Studies
of The University of Manitoba

In partial fulfillment of the requirements of the degree of

DOCTOR OF PHILOSOPHY

Department of Environment and Geography

University of Manitoba

Winnipeg

Abstract

The Arctic is experiencing rapid changes due to global warming, making it possible for enhanced industrial activities in the region. The increasing maritime shipping, oil and gas exploration and extraction activities, and other developments increase the risk of oil spills in ice-covered Arctic waters. Among the oil components, aromatic hydrocarbons are of particular concern due to their widely known toxic effects on marine ecosystems. The transport and fate of petrogenic aromatic hydrocarbons in Arctic sea ice are largely controlled by their physicochemical properties and sea ice dynamics. Yet, the interplay of those properties and changing sea ice conditions in the distribution of petrogenic aromatic hydrocarbons across the seawater-ice-atmosphere interface remains poorly understood. This thesis investigates the mechanisms governing the distribution of petrogenic aromatic hydrocarbons in sea ice and across the seawater-ice-atmosphere interface through a series of outdoor microcosm and mesocosm experiments. The distribution of aromatic hydrocarbons across the ice column from an encapsulated oil lens, as well as their exchange with the atmosphere and the underlying seawater, differ depending on the compound. Specifically, low-molecular-weight aromatic hydrocarbons, such as alkylbenzenes and less-substituted alkylnaphthalenes, are found to partition to air inclusions in sea ice and subsequently follow air bubble dynamics, resulting in substantial losses to the atmosphere. Moderate-molecular-weight aromatic hydrocarbons, including more-substituted alkylnaphthalenes and three-ring polycyclic aromatic hydrocarbons, preferentially dissolve in sea ice brine and subsequently migrate downward to the water column. High-molecular-weight four- to five-ring polycyclic aromatic hydrocarbons tend to interact with particulate organic matter immobilized in brine channels, resulting in their accumulation and retention in sea ice. Furthermore, it is shown that the effects of temperature and salinity on the partitioning behaviour of polycyclic aromatic hydrocarbons in sea ice and freezing seawater are substantially more complex than those at temperatures above 0°C. Overall, this thesis provides new and in-depth insights into the mechanisms and distribution pathways of petrogenic aromatic hydrocarbons with varying physicochemical properties in the sea ice environment. These results will advance and improve oil spill weathering modelling and toxicity assessment, therefore contributing to the development of a suitable oil spill response strategy in the rapidly changing Arctic Ocean.

Acknowledgements

I would like to thank my advisors and mentors, Dr. Feiyue Wang and Dr. Gary Stern, for the opportunity to pursue this research, as well as their constant support, encouragement and guidance, and for believing in me throughout this journey, especially in the last stages of my thesis. I am exceptionally grateful for your wisdom, time, good word and mentorship. I feel honoured to have had the opportunity to work under your wings.

I would also like to thank my advisory committee members, Dr. Gregg Tomy and Dr. Mark Hanson, for their time, enlightening insights into my research and constructive discussions throughout the years.

Special thanks go to my colleagues, especially Debbie Armstrong, for her support and lifting my spirits, to Dave Binnie, without whose expertise and support my SERF experiments would not have been possible, and to Dr. Zhiyuan Gao for our conversations, words of wisdom and encouragement, and collegiality.

A huge thank you to all my friends at CEOS and beyond, in particular to my dear friend Aura Diaz, who has accompanied me every step of the way through the difficulties and challenges in a PhD student's life, for all the eye-opening chats we shared and for always having my back.

A heartfelt thank you to Dr. Cathrin Veenaas for her friendship and for being my lab buddy during those long days and nights in the lab.

I would also like to thank my family and loved ones for their exceptional support and faith in me throughout this endeavour. Most importantly, this work could not have been done without my life-partner and best friend, Piotr Ahmad, who shared every step and idea of this journey with me, for his endless support and for constantly believing in me.

I am also grateful to Dr. Monika Pućko for introducing me to CEOS and sea-ice research at the beginning of my studies.

Lastly, I would like to acknowledge the financial support from the Natural Sciences and Engineering Research Council (NSERC) of Canada, the Canada Research Chairs (CRC) Program, Genome Canada, and Genome Prairie.

Dedication

This doctoral thesis is dedicated to the loving memory of my Grandpa Ignacy for his unwavering love for the Arctic.

And to my younger self, who had the courage, stubborn bravery and foolish perseverance to see this journey through.

Table of Contents

CHAPTER 3 DISTRIBUTION OF DIESEL AND AROMATIC HYDROCARBONS IN DIESEL-IN-ICE SPILL SCENARIO: A MICROCOSM STUDY 60

List of Tables

List of Figures

were calculated relative to the initial amounts of diesel fuel/TAHs injected into the microcosms on day 0.

Figure 3.5. Heatmap showing variations in the vertical distribution of the 46 aromatic hydrocarbons expressed as the relative fraction (f; %) of each compound in the water, the top, middle and bottom ice core sections, and the air (potential loss) throughout the study. The air (loss) percentage was estimated from the difference between the original amount of each analyte in diesel on day 0 and the amount detected in the microcosms on each sampling occasion. (Yellow: f = 50%; dark green: f = 0%; dark red: f = 100%).

Figure 3.6. Estimated cumulative mass of TAHs (m_{TAHs}; displayed as bars) and mass flux of TAHs (F_{TAHs}; displayed as curves) that occurred between the two consecutive sampling events to the air (a) and to the water column (b).

Figure 3.7. Schematic summary of the temporal and spatial distribution of diesel and its aromatic hydrocarbons across the seawater-ice-atmosphere interface in a diesel-in-ice microcosm under cold winter conditions.

Figure 4.1. A schematic (a) and a photograph (b) of the experimental fiberglass tub used to carry out the crude oil-in-sea-ice mesocosm study at the Sea-ice Environmental Research Facility, Winnipeg, Canada. Also shown are the locations of collected brine (blue circles) and surface sea ice (orange triangle) samples.

Figure 4.2. Vertical profiles of temperature (a), salinity (b), and brine volume fraction (c) across the sea ice column (circle symbols), in the brine (triangle symbols) and the water column (square symbols) in the mesocosm on various sampling days. The uppermost point on the y-axis corresponds to the air-ice interface.

Figure 4.3. Ratios of analyte abundances in the surface sea ice samples on day 2 to those on day 3 (blue bars), and on day 6 to those on day 3 (yellow bars).

Figure 4.4. Chemical composition profiles of the studied aromatic hydrocarbons in the fresh crude oil mixture (a) and in the sea ice core section samples collected from different ice depths on day 15 (b-d).

Figure 4.5. Heat maps illustrating variations in the R_{TM} (ratio of concentrations in the top to middle ice core sections) and R_{BM} (ratio of concentrations in the bottom to middle ice core sections) ratio values of the 42 aromatic hydrocarbons during the four sampling events. The middle ice core sections correspond to values of 1.0 and are displayed in grey. Note that cells corresponding to undetected compounds are displayed in white. (Blue: $R < 1$; red: $R > 1$).

Figure 4.6. Ratios of analyte concentrations in the brine samples collected on day 20 to those on day 24. The brine samples extracted from the 15-cm sump-hole are shown in orange, and those in the 30-cm sump-hole are displayed in blue.

Figure 4.7. A schematic summary of the transport processes driving the distribution of crude oil alkylbenzenes and alkylnaphthalenes. R_{TM}: concentration ratio of a compound in the top ice section relative to that in the middle; R_{BM}: concentration ratio of a compound in the bottom ice section relative to that in the middle. (Blue: $R < 1$; red: $R > 1$).

List of Abbreviations and Acronyms

AHs: aromatic hydrocarbons
BTEX: benzene-toluene-ethylbenzene-xylene
CEPA: Canadian Environmental Protection Act
CMO: Churchill Marine Observatory
EPA: Environmental Protection Agency
FYI: first-year ice
GC: gas chromatograph
HCH: hexachlorocyclohexane
HFO: heavy fuel oil
HMW: high-molecular-weight
ISB: *in-situ* burning
K_d: distribution/partition coefficient
K_H: Henry's Law Constant
K_{OA}: octanol-air partition coefficient
K_{OW}: octanol-water partition coefficient
LLE: liquid-liquid extraction
LMW: low-molecular-weight
LOQ: limit of quantification
MAHs: monoaromatic hydrocarbons
MDL: method detection limit
MDO: marine diesel oil
MGO: marine gas oil
MMW: moderate-molecular-weight
MS: mass spectrometer
MS/MS: triple quadrupole mass spectrometer
MYI: multi-year ice
NIST: National Institute of Standards and Technology
NSR: Northern Sea Route

NWP: Northwest Passage

OSIM: Ocean-Sea Ice Mesocosm

PAHs: polycyclic aromatic hydrocarbons

PFAS: per- and polyfluoroalkyl substances

POC: particulate organic carbon

POM: particulate organic matter

RRF: relative response factor

S_{aq}: aqueous solubility

SARA: saturates-aromatics-resins-asphalthenes

SERF: Sea-ice Environmental Research Facility

SHS: static headspace

SIM: selected ion monitoring

SPE: solid phase extraction

TAHs: total aromatic hydrocarbons

TEQ: Toxic Equivalency

QSAR: Quantitative Structure–Activity Relationship

USGS: United States Geological Survey

V_B: brine volume fraction

V_P: vapour pressure

Chapter 1 Introduction

The chapter begins with the thesis research objectives and hypotheses. This is followed by an overview of the rapidly changing Arctic Ocean and ongoing and projected industrial developments, and a summary of the current state of knowledge on the fate and behaviour of oil spills in ice-covered waters, with a special emphasis on the environmental fate of petrogenic aromatic hydrocarbons. I conclude with the identification of critical knowledge gaps in the field. Finally, the structure of the thesis is introduced.

1.1 Thesis Objectives and Research Hypotheses

The overarching objective of this thesis is to address several critical knowledge gaps in the understanding of the mechanistic behaviour and pathways of petrogenic aromatic hydrocarbons in the sea ice environment. Keeping in mind the role of physicochemical properties of aromatic hydrocarbons and the role of sea ice dynamics in their overall distribution tendencies, this thesis tests the following three research hypotheses:

a) Polycyclic aromatic hydrocarbons of varying physicochemical properties interact with sea ice-associated particulate organic matter to different extents;
b) Aromatic hydrocarbons of varying physicochemical properties in oils encapsulated in sea ice are distributed across the seawater-ice-atmosphere interface through different mechanisms; and,
c) The type of spilled petroleum product (crude oil *vs* diesel fuel) does not impact the distribution patterns of individual aromatic hydrocarbons in an oil-in-ice spill scenario.

1.2 General Background

1.2.1 Risks of industrial development of the Arctic due to climate change

In the era of global warming, the Arctic is undergoing swift climate change. The rapid loss of sea ice in the Arctic makes this region more accessible to anthropogenic activities. As such, resource development, maritime shipping and transportation, as well as tourism, have already increased and are projected to further increase in and around the Arctic (Dawson et al., 2018; Dawson et al., 2016; Lackenbauer and Lajeunesse, 2014; Stewart et al., 2013; Stewart et al., 2007). In line with these changes, there is an increasing risk of uncontrolled release of hydrocarbons in the region.

1.2.1.1 Climate change-driven sea ice decline in the Arctic

Under the changing climate, the Arctic is warming at a faster rate than any other place on Earth. Recent studies report that since 1979, the Arctic region has warmed almost four times the rate relative to the rest of the globe (Rantanen et al., 2022). One of the greatest indicators of increasing temperatures in the region is the change in the icescape: perennial sea ice is transitioning into annual ice, the extent and thickness of the sea ice cover are declining, and the length of the ice-free season is increasing (Babb et al., 2023; Stroeve et al., 2007; Stroeve et al., 2012; Stroeve et al., 2014).

For the past few decades, the summer Arctic sea ice extent has been declining at a rate of 12.2% per decade relative to the average between 1981 and 2010 (NASA, 2025). Since 1979, the Arctic sea ice summer minimum (measured in September) decreased from more than 16,000 to 4,000 km^3 in the recent summers (Gascard et al., 2019), giving rise to nearly a 75% decrease in the total volume of Arctic sea ice during summer. Current global climate models project that the Arctic Ocean will be seasonally ice-free before mid-century (Notz and Stroeve, 2018).

1.2.1.2 Maritime shipping activities

Greater accessibility of the Arctic Ocean has contributed to enhanced marine transportation and shipping activities (Andrews et al., 2017; Dawson et al., 2018; Pizzolato et al., 2014). Specifically, between 2013 and 2024, the number of ships navigating through Arctic waters increased by 37%, with the largest number of ships recorded in September, which coincides with the lowest extent of sea ice during that time. Additionally, the distance sailed by vessels in Arctic waters increased from 6.1 million to 12.7 million nautical miles, giving rise to a 108% increase since 2013 (Arctic Council, 2025). In the Canadian Arctic alone, ship traffic showed more than a threefold increase since 1990 (Dawson et al., 2018; Pizzolato et al., 2016).

Currently, shipping in Arctic marine waters is focused primarily on the transport of goods to isolated Northern communities and industrial facilities, natural resource development, ice-breaker support for sealift traffic, research activities, supply of offshore drilling operations, as well as transportation of ore and crude oil by tankers (AMAP, 1998). Furthermore, in recent years, a noticeable increase in high-end tourism and cruising activities has been observed throughout the Arctic, including the Canadian Arctic (Dawson et al., 2018; Johnston et al., 2012; Stewart and Dawson, 2011), Svalbard and Greenland (MOSJ, 2023), with the number of passengers in 2022 nearly as high as at the levels before the Coronavirus pandemic in some areas (MOSJ, 2023).

Retreating sea ice cover in the Arctic has implications for longer navigation periods, and the potential for easier and safer navigation through historically inaccessible polar corridors, in particular the Northern Sea Route (NSR) and the Northwest Passage (NWP). Both routes are increasingly perceived as cost-effective alternatives to Suez or Panama Canal routes (Stroeve et al., 2012) as they reduce the length of other trade lanes by up to 50% (Eguíluz et al., 2016).

1.2.1.3 Oil and gas exploration and production activities

Non-renewable fossil fuels, such as crude oil and natural gas, are by far the most commonly used energy sources. Despite the emphasis on the development of technologies for sustainable and renewable forms of energy, and the gradual depletion of fossil fuel reserves, oil is expected to remain a primary fuel for the upcoming decades. Thus, petroleum companies venture into more challenging and remote regions, seeking natural resource reserves for potential future exploration.

In 2008, the United States Geological Survey (USGS) revealed that 22% of the world's undiscovered, technically recoverable oil and gas resources may be found in the area north of the Arctic Circle (USGS, 2008). If extracted, these resources would cover the world's crude oil consumption demand for about 8 years, assuming the current global fuel source structure is maintained. Climate change-induced sea ice loss in the Arctic makes these reserves potentially available for future exploitation, which in turn makes oil and gas exploration and production activities of special interest.

By 2007, there had been more than 400 oil and gas fields developed north of the Arctic Circle, with most of these fields located within the West Siberian Basin of Russia and on the North Slope of Alaska. Offshore wells had also been drilled, mostly within the Mackenzie Delta, the Barents Sea, the Sverdrup Basin, and offshore Alaska. However, the majority remain undeveloped (Bishop et al., 2011; Gautier et al., 2009). Offshore oil and gas activities have largely been suspended within the Arctic territories of Canada (Shapovalova and Stephen, 2019) and Greenland (Christiansen, 2021). In Alaska, offshore oil exploration was abandoned in 2024 as a result of Shell's failed trials of well drilling in the Chukchi Sea (Henderson and Loe, 2014). Furthermore, in 2016, both the U.S. and Canada issued a moratorium on new oil and gas leasing in their Arctic seawaters over environmental concerns. While in the Canadian Arctic waters oil exploration and production activities are prohibited indefinitely, in the U.S., the current Trump administration has approved oil leasing in Arctic waters (Miller, 2025). Oil and gas exploration on the other side of the Arctic, however, presents a completely different picture. For example, Arctic offshore oil and gas exploration operations in Norway and Russia are concentrated in the Barents and Kara Seas, where extensive geological exploration and extraction are ongoing (Agarkov et al., 2019; Carayannis et al., 2021; Dzyublo et al., 2021).

1.2.1.4 Oil spill likelihood in the Arctic Ocean

Currently, the most probable scenarios resulting in uncontrolled release of petroleum hydrocarbons in the Arctic Ocean include crude oil production operation mishaps (e.g., offshore oil platform and well blowouts, and pipeline ruptures), and ship-source spills (e.g., vessel collision, grounding, or sinking during transportation, and transfer of fuel from vessels to communities). The latter could potentially release oil distillates (products created by refining crude oil), in particular diesel fuel, which is abundantly transported to Northern communities, who rely on it as a source of heat and energy. Moreover, residual fuels (heavy leftover fractions of crude oil refining; e.g., heavy fuel oil (HFO)) and marine distillate fuels (blends of distillate and residual fuels; e.g., marine gas oil (MGO) and marine diesel oil (MDO)), used to operate vessels travelling through the Arctic, could also be accidentally discharged during shipping activities (Comer et al., 2016; Daling et al., 2020; PAME, 2020). Substantial amounts of hydrocarbons in the region may also originate from natural oil seeps, land-based discharges (e.g., refineries, municipal wastewater, industrial wastewater), and runoff (e.g., urban runoff, combustion of wood and fossil fuels), and riverine sources (AMAP, 1998). Additionally, oil storage tanks, pipelines and installations built on land, especially on permafrost, are also susceptible to collapse, resulting in uncontrolled release of petroleum that could affect both freshwater and marine ecosystems. This is demonstrated by a recent oil spill incident in the sub-Arctic, which took place in 2020 near Norilsk City in the Taimyr region, Russia. The Norilsk leak occurred due to a collapse of a diesel fuel storage tank built upon permafrost (Bezmaternykh et al., 2021), discharging over 206 thousand barrels of diesel oil, making it the largest oil spill in the Arctic and contaminating Lake Pyasino, which is connected to the Kara Sea *via* the Pyasina River (Glyaznetsova et al., 2021; Tysiąc et al., 2022).

Overall, the risk of an oil spill occurring in Arctic waters is significantly lower than for Southern areas due to smaller traffic volume and less substantial oil and gas activities in the region; however, the Exxon Valdez incident in 1989 in Prince William Sound, Alaska, during which over 37,000 m^3 of crude oil were spilled to the Northeast Pacific from an oil supertanker, serves as a reminder that the Arctic Ocean is not immune to such spills. The consequences of a larger Arctic marine spill could potentially be devastating for food security and human health, particularly to coastal Inuit and other Indigenous communities, and cause high social, environmental and economic costs.

1.2.2 Aromatic hydrocarbons in the Arctic

Petroleum oils are arguably one of the most complex mixtures in the world, consisting of thousands of molecules of plant, animal, or mineral origin (Pampanin and Sydnes, 2013; Wang and Stout, 2016). The chemical composition of oils is dominated by hydrocarbons comprised exclusively of carbon and hydrogen atoms in their structures, with a substantially lower number of non-hydrocarbons containing heteroatoms (e.g., nitrogen, sulphur, oxygen) or metals (e.g., iron, nickel, and vanadium).

Oil constituents are generally categorized based on their structure, into four groups collectively referred to as SARA fractions: saturates (S) exhibiting straight- and branched-chain or cyclic saturated structures; aromatics (A) with structures based on benzene ring; resins (R) encompassing polar compounds built from heterocyclic compounds; and asphaltenes (A) containing heterocyclic compounds on a high-molecular-weight spectrum. In addition to the

SARA groups, oils can contain minor amounts of metals (e.g., nickel, vanadium, and chromium) and organometallic compounds (Lee et al., 2015).

Among these four fractions, special concerns arise around aromatic hydrocarbons (AHs), in particular monoaromatic (MAHs) and polycyclic aromatic hydrocarbons (PAHs), as they are primarily associated with the toxicity of petroleum (Johnson et al., 2018; Pampanin and Sydnes, 2013; Ucan-Marin and Dupuis, 2015). Below, both groups are described in more detail.

1.2.2.1 Monoaromatic hydrocarbons

MAHs are unsaturated compounds with a structure based on a single benzene ring that contributes to their high stability and persistence in the environment (Fingas, 2015). There can be one or more alkyl groups attached to carbon atoms in the ring structure in different isomeric positions. Overall, less-substituted MAHs represent the most volatile and water-soluble fraction in oils; therefore, they are among the most readily bioavailable oil components to the local biota. Their high volatility contributes to their short-term presence and lower persistence in the environment.

The most abundant and, therefore, studied MAHs in petroleum are benzene, toluene, ethylbenzene, and the three xylene isomers (*p*-, *m*-, and *o*-xylenes) referred collectively as BTEX compounds; their structures are displayed in Figure 1.1. BTEX compounds are well-documented to exhibit toxic, carcinogenic and neurotoxic effects on living organisms (Gagnaire and Langlais, 2005; Heinrich, 2003) and often are linked with mortality observed during the first few hours to a few days after an oil spill (Dupuis & Ucan-Marin, 2015). Therefore, in the mid-1980s, the US Environmental Protection Agency (EPA) placed benzene, toluene and ethylbenzene on its list of toxic “Priority Pollutants” (USEPA, 1987), whereas in 1999, the Canadian Environmental Protection Act (CEPA) placed BTEX compounds on its First Priority Substances List (CEPA, 1999). On average, BTEX compounds comprise up to 2.5% of crude oil (by weight; %wt), and 15–25% of gasoline composition (%wt) (Ucan-Marin and Dupuis, 2015; Williams et al., 2006).

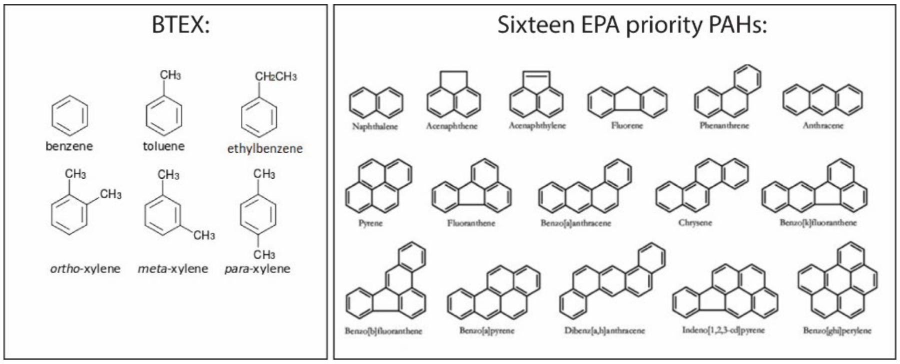

Figure 1.1. The structures of BTEX compounds and sixteen priority PAHs.

In addition to the well-studied BTEX series, many oils contain more-substituted homologues of benzene, such as C_3–C_8-alkylbenzene sequences, though they are often present in oil in smaller proportions than BTEX compounds (Wang et al., 1995). Several studies have shown that alkylbenzenes (e.g., propylbenzenes and trimethylbenzenes) tend to bioaccumulate and pose high acute toxicity effects in aquatic biota (for review see Peng et al., 2021), as well as contribute to chronic adverse effects on the central nervous system in rats (Wiaderna et al., 2002). However, to date, scarce data exist on the fate of more-substituted alkylbenzenes following an oil spill in aquatic environments (Wang et al., 1995); thus, their biological effects remain unknown.

1.2.2.2 Polycyclic aromatic hydrocarbons

PAHs contain two or more fused benzene rings in their structure. Just like in the case of MAHs, there can be one or more alkyl groups attached to the benzene rings in different isomeric positions, affecting their physicochemical properties (Ucan-Marin and Dupuis, 2015). PAHs may comprise between near 0 to 50% of the composition of oil (%wt), depending on the petroleum product (Ucan-Marin and Dupuis, 2015). For instance, on average, PAHs comprise ~1% of crude oil composition (Williams et al., 2006) with a greater proportion from the alkylated homologues of LMW PAHs (NRC, 2003). On the contrary, in HFO, PAHs typically represent between 30 and 50% of the product by weight (Ucan-Marin and Dupuis, 2015).

PAHs are of particular public concern due to their continuous release to the environment (from petrogenic and pyrogenic sources), relatively high persistence, and potent adverse effects on marine biota and humans (AMAP, 1998; Yan et al., 2004). In addition to BTEX compounds, 16 parent PAHs (naphthalene, acenaphthylene, acenaphthene, fluorene, phenanthrene, anthracene, fluoranthene, pyrene, benzo[*a*]anthracene, chrysene, benzo[*b*]fluoranthene, 3 benzo[*k*]fluoranthene, benzo[*a*]pyrene, dibenz(ah)anthracene, benzo[*ghi*]perylene, indeno[1,2,3-*cd*]pyrene) along with their alkylated homologues were placed on the priority pollutant list by the US EPA (USEPA, 1987) and on the CEPA First Priority Substances List (CEPA, 1999). Recently, PAHs have also been classified as chemicals of emerging Arctic concern (CEAC), given their increasing emissions and persistence in the marine Arctic waters (AMAP, 2017). The structures of the 16 priority PAHs are presented in Figure 1.1.

The biological effects of PAHs are related to the size and structure of their molecules. Specifically, PAHs composed of two to three aromatic rings (e.g., naphthalene, phenanthrene), collectively referred to as low-molecular-weight (LMW) PAHs, are relatively more volatile and more water-soluble, and are often associated with acute toxicity and genotoxicity, though with a low potential for carcinogenicity (NTP, 2011). Conversely, high-molecular-weight (HMW) PAHs consisting of at least four aromatic rings in the structure (e.g., pyrene, benzo(a)pyrene) are less volatile and water soluble relative to LMW PAHs. As a result, they are more persistent in the environment, tend to degrade slowly and therefore contribute more to chronic toxicity to marine biota (Bornstein et al., 2014; Carls et al., 1999; Hodson et al., 2007; Noh et al., 2018). They are also frequently associated with high mutagenicity and carcinogenicity (NTP, 2011), and can bioaccumulate in aquatic organisms (Liu et al., 2023; Meador et al., 1995).

Among PAHs, the alkylated homologues are more persistent in the environment than their unsubstituted counterparts (Barron and Holder, 2003). They are also considered to be (in some cases up to ten times) more toxic to marine fauna than their parent congeners (Johnson et al., 2018; Turcotte et al., 2011). However, to date, scientific efforts have primarily focused on the fate and biological effects of parent PAHs, overlooking the behaviour and effects of alkylated homologues, which in turn contributes to the underestimation of the overall toxic potential of spilled oils.

While the greatest threat from AHs release to the marine Arctic cryosphere comes from oil spills related to shipping and local oil exploration, as well as natural oil seeps, PAHs may be also transported to Arctic waters from lower latitudes through long-range atmospheric transport and oceanic circulation, as well as by northward flowing rivers, and transpolar ice drift (Ma et al., 2013; Zhang et al., 2023). In addition to petroleum-related affairs, PAHs can enter the remote

Arctic region from combustion and wildfires. PAHs formed during the incomplete combustion of natural and anthropogenic sources are known as pyrogenic PAHs (AMAP, 2010).

1.2.3 Environmental fate of aromatic hydrocarbons across the ocean-ice-atmosphere interface

1.2.3.1 Interphase partitioning

Environmental fate of AHs is largely controlled by interphase partitioning, a term which describes their tendency to distribute in one phase (e.g., air, water, organic matter, mineral solids, and organisms) over the other. Partitioning of AHs between different phases of the environment has implications for their bioavailability, exposure pathways to the local biota, and toxicity. Chemical partitioning is typically based on a solubility-driven distribution of solute between two or more immiscible phases (Mackay and Wania, 1995; Schwarzenbach et al., 2016) and can be quantitatively expressed as a distribution or partition coefficient (K_d). Practically, K_d is often related to the octanol-water partition coefficient (K_{OW}) and octanol-air partition coefficient (K_{OA}). K_{OW} is defined as the ratio of a compound's concentrations in octanol (a proxy used for organic phases, such as particles, vegetation and soil) and water at equilibrium. It is used to predict compound partitioning tendencies between organic and aqueous phases (hydrophobicity), as well as propensity for bioaccumulation (Schwarzenbach et al., 2016). Meanwhile, K_{OA} describes the tendency of a compound to distribute between octanol and air at equilibrium (Schwarzenbach et al., 2016).

Among the key properties controlling a compound's distribution between the environmental phases are vapour pressure (V_P), aqueous solubility (S_{aq}), and Henry's Law Constant (K_H). Specifically, V_P is defined as the pressure exerted by the vapour of a substance at equilibrium with its pure condensed form (Schwarzenbach et al., 2016), and it describes the propensity of a compound to migrate to and from gaseous phases. S_{aq} is defined as the concentration of a chemical in the aqueous phase when the solution is in equilibrium with the pure form of a compound at a specific temperature and pressure (Schwarzenbach et al., 2016). Lastly, K_H describes how a compound is distributed between gaseous and aqueous phases at equilibrium and is defined as the ratio of a compound's partial pressure and its molar concentration in the aqueous solution (Schwarzenbach et al., 2016).

Physicochemical properties, and therefore the overall distribution of a chemical between the environmental compartments, in particular those involving air to condensed phase partitioning, are strongly impacted by temperature. At low temperatures, partition coefficients of AHs from the atmosphere to seawater, soil and biota increase substantially, thus contributing to elevated ecosystem concentrations (Macdonald et al., 2000). Unlike in the case of temperature, the presence of salt has a less profound effect on the partitioning of AHs (Whitehouse, 1984). In general, the addition of salt reduces the aqueous solubilities of AHs (Berkowitz, 2008), contributing to their preferential distribution in either gaseous or organic phases.

In multi-compartment environments, such as icy Arctic waters, the distribution of AHs becomes more complex and therefore more challenging to project. Environmental behaviour models based on two or more partition coefficients may be used to project the transport and fate of released hydrocarbons. However, the availability of empirically determined distribution coefficients for many organic contaminants, including AHs, across the environmental compartments of Arctic ice-covered waters is extremely limited.

1.2.3.2 Role of sea ice in the distribution and transport of contaminants across the ocean-ice-atmosphere interface

Sea ice is a highly heterogeneous material consisting of multiple environmental phases in a confined space, such as air inclusions, brine (concentrated, saline aqueous phase), solid ice crystal matrix, and particulate matter (for review, see Thomas, 2016). During ice growth, the volume and content of its internal phases change in line with temperature and salinity. It also undergoes desalination processes, which contribute to its highly dynamic nature. Desalination processes occur through brine expulsion, gravity drainage and flushing. Brine expulsion is an upward migration of brine to the ice-snow interface driven by internal pressure created from ice formation. Gravity brine drainage is driven by the high density of concentrated brine and it dominates throughout the ice growth period, whereas flushing usually occurs during spring ice melt and is forced by surface snow or ice melt (Cox and Weeks, 1975).

As sea ice forms and grows, a fraction of contaminants dissolved in seawater is rejected (just like major salt ions) from the ice crystal matrix due to size restrictions, a phenomenon known as freeze rejection. Contaminant incorporation within the ice matrix lattice is a very minor process, as it could lead to large defects in the crystal structure. The rejected portion of dissolved contaminants is released to the water column, whereas the remaining fraction is retained in brine pockets and channels. A portion of aquatic particles in seawater from which the ice is growing may also enter the ice, and in turn, contaminants bound to them. This mechanism is known as particle entrapment (Wang et al., 2017).

During their residence in sea ice, chemicals can be present as gases in air inclusions, species dissolved in brine or attached to the internal ice crystal surfaces and/or ice particles. Moreover, depending on their physicochemical properties and the geophysical characteristics of the ice, contaminants may repartition between the ice compartments. They may also be further exchanged with the underlying seawater or the overlying atmosphere through sea ice dynamics. For instance, gaseous contaminants can be transported to the atmosphere through convection with brine, diffusion with the concentration gradient (in the dissolved state within the brine), and upward buoyant air bubble transfer (in the gaseous state within the brine), similar to that of CO_2, CH_4, and O_2 (Tison et al., 2017). Dissolved contaminants accommodated within brine channels and pockets can be transported to either snow through brine expulsion or can be transferred to the underlying seawater *via* downward brine drainage (Wang et al., 2017).

For brine and air bubble-mediated transport processes across the ocean-ice-atmosphere interface to occur, a certain level of sea ice permeability, often expressed as brine volume fraction (V_B; defined as the fraction of brine relative to the total ice volume), is required. In general, brine movements are expected to occur for brine volume fractions of at least 5% (Golden et al., 1998; Golden et al., 2007), whereas for upward bubble migration, a brine volume fraction of 7% is necessary (Zhou et al., 2013). Diffusive transport across porous sea ice has been suggested as an alternative pathway for gas exchange between seawater and the atmosphere in the absence of brine drainage (Loose et al., 2011).

Unlike gaseous and dissolved contaminants, particle-bound chemicals entrapped in sea ice are less prone to redistribution to the water column, due to particle immobilization, contributing to their enrichment in the ice cover relative to less particle-reactive species, as has been shown for mercury (Chaulk et al., 2011). Moreover, particle-reactive hydrophobic compounds may additionally undergo sorption onto solid ice interstitial surfaces, which will also lead to their preservation in sea ice (Garnett et al., 2021; Garnett et al., 2019; Pućko et al., 2015). Ultimately, particle- and ice-surface-associated compounds will likely be released in a substantial fraction during sea ice melt rather than during its growth, as demonstrated previously for snow samples (Meyer et al., 2009a, 2009b). Since particle- and ice-surface-bound compounds are held back from being washed out early from the ice, they will likely contribute to prolonged exposure for sea ice communities. Nonetheless, the role of aquatic particulate organic matter (POM) in the entrapment and distribution of particle-reactive contaminants in sea ice, as well as the mechanisms driving that process, remain poorly understood.

1.2.3.3 Exposure pathways for aromatic hydrocarbons

Diffusion of dissolved aromatic fractions across biological membranes (e.g., gills, skin, and other membranes) presents an important exposure pathway for aquatic biota. In general, bioavailability of dissolved AHs is greater relative to that of particle-associated species (NRC 2003). Furthermore, dissolved fraction concentrations appear to be better predictors of a compound's potential for accumulation in live tissues (Pruell et al., 1986). Unlike dissolved AHs, particle- and sediment-associated congeners can be available to benthic biota (e.g., invertebrates, benthic fish and deposited fish eggs), either through ingestion or direct contact, presenting another pivotal exposure pathway (CCME, 1999).

Availability of AHs to aquatic and sea ice biota is directly associated with their physicochemical properties, environmental parameters (e.g., presence of particulate and dissolved matter, temperature, and salinity), as well as biological factors (e.g., feeding characteristics of an organism). Specifically, MAHs and LMW PAHs (e.g., two- to three-ring PAHs) are relatively water-soluble, therefore potentially more available to biota by diffusion through membranes (French-McCay, 2004). Conversely, hydrophobic HMW PAHs with high log K_{OW} values (e.g., > 5; four-and more-ring PAHs) will preferentially bind to particulate matter; thus, they will interact with biota through contact or diet (CCME, 1999). Overall, low temperatures enhance bioaccumulation of PAHs (AMAP, 1998).

The role of physicochemical properties of AHs in their availability to marine organisms indicates the importance of a better understanding of their partitioning behaviours in sea ice and surrounding cold Arctic waters. Quantitative data on fluxes of AHs within and outside of sea ice would be beneficial for accurate predictions of AH effects and exposures.

1.2.4 Behaviour and fate of oil and its aromatic hydrocarbons in ice-covered waters

In-depth understanding of the behaviour and fate of oil and its constituents in aquatic environments is a crucial component of oil spill detection, damage assessment, and oil spill response strategies. Below, a summary of the overall behaviour of oil in, on, and under sea ice is presented (summarized in Figure 1.2).

1.2.4.1 Oil weathering

Oil exposed to aquatic environments will be subjected to various physical, chemical and biological processes collectively referred to as weathering. These include evaporation to air, dispersion and dissolution in water, emulsification with water, photo-oxidation, interactions with particles and sedimentation, ingestion by biota, and biodegradation (NRC, 2014). These processes often act simultaneously and can be self-competing, depending on the oil spill scenario. Weathering progressively alters the chemical and physical properties of the exposed oil, thus its behaviour and ultimate fate in the environment. This further impacts the window of opportunity for first responders and the applicability of oil spill response strategies.

Given the complex composition of oil, weathering processes will selectively impact oil constituents to varying degrees. Specifically, evaporation immediately affects the most volatile among petrogenic AHs, such as MAHs (Lee et al., 2011), contributing to their substantial loss within hours following an oil spill (Mishra and Kumar, 2015). Depending on the content of AHs in a spilled fuel, their loss from an oil film may have a substantial impact on the bulk properties of the remaining oil (e.g., viscosity, density, flash point), hence impacting the applicability of an oil spill clean-up method. Conversely, dissolution in seawater impacts relatively water-soluble parent and alkylated LMW PAHs. However, dissolution is not considered to cause a significant loss of AHs relative to evaporation (Riazi and Edalat, 1996). Sorption to organic matter, on the other hand, affects parent and alkylated PAHs consisting of four or more benzene rings (Payne et al., 2003), the latter having a higher tendency to interact with particles and greater persistence in sediments following sedimentation (Gearing and Gearing, 1983). In general, sorption of AHs onto organic matter is not considered to substantially contribute to the overall mass balance of aromatic compounds following an oil spill. Nonetheless, both dissolution and interactions with particulate matter are crucial exposure pathways of AHs to the local biota.

Regardless of latitude, oil released in the marine environment will be subjected to similar weathering processes. The extent and rate of weathering processes, however, will differ depending on oil type, environmental conditions (e.g., wind and wave conditions, temperature and sunlight), the properties of seawater (e.g., salinity, temperature), and most importantly, the presence and dynamics of sea ice in high latitudes. In polar seas, most of the weathering processes will be slowed down or eliminated (e.g., evaporation, dispersion, emulsification, biodegradation) due to low temperatures, limited mixing energy and hindered spreading of oil. Meanwhile, other processes (e.g., sedimentation, sinking) may be enhanced due to increased viscosity and density of oil at low temperatures (Lee et al., 2015).

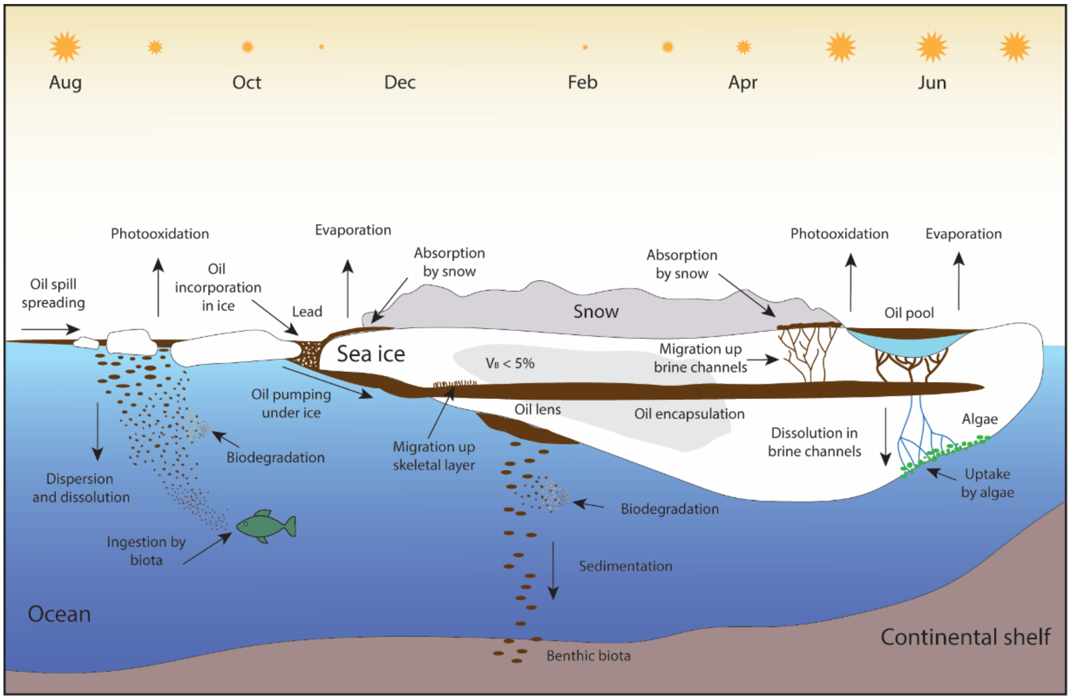

Figure 1.2. A schematic showing the overall behaviour of oil in ice-covered waters. Source: adapted from Wang et al., 2017.

1.2.4.2 Behaviour of oil in ice-covered waters

Oil spilled in icy Arctic waters will interact with sea ice in a variety of ways, depending on the amount and type of oil spilled, the source of discharge, environmental circumstances, as well as implemented response and remediation methods (Afenyo et al., 2016). Moreover, each oil spill scenario in ice-covered waters comes with its own weathering characteristics.

Oil spill in broken ice

The behaviour of oil spilled in broken ice during summer will largely depend on the extent of ice coverage. Specifically, if less than 30% of the sea surface is covered with ice, the oil slick will spread essentially the same as in open water, whereas at ice concentrations greater than 30%, the oil will be contained between ice floes and its movement will be restricted to the ice drift. Slush ice will additionally restrict the spreading of the oil slick (Venkatesh et al., 1990). The hindered spreading of oil will contribute to an increase in oil film thickness compared to open-water oil slicks, therefore reducing the rate and extent of evaporative transfer of MAHs, LMW PAHs and other volatile oil components (Brandvik and Faksness, 2009). Depending on the state of the sea and the properties of the released product, oil may be subjected to dispersion, resulting in enhanced dissolution of water-soluble AHs. Upon exposure to seawater, AHs may interact with suspended particulate matter as well, with potential for subsequent sinking. Additionally, uptake by biota, biodegradation and photooxidation may also affect AHs to a certain degree during oil's containment between ice floes.

Oil spill under freezing conditions

If oil is released in narrow linear cracks in the ice (leads) under freezing conditions, a portion of it may be incorporated within the newly forming ice. At high ice growth rates (e.g., > 12 cm s^{-1}), the oil will be pushed onto the ice surface (which is known as "lead pumping") (Cammaert, 1980), facilitating evaporative transfer of AHs to the air and photooxidation. At lower ice growth rates, the oil will likely be forced under the ice surface to the water (Cammaert, 1980), therefore largely ceasing evaporation, and potentially enhancing the potential of AHs for dissolution and interactions with particulate matter and seawater microorganisms.

Oil spill under growing ice

Oil released from a subsurface well or pipeline blowout under a continuous layer of ice will disperse into small droplets (< 1 cm in diameter), which will rise to the under-ice surface due to the density contrast with seawater (Wilkinson et al., 2017). Upon contact with the bottom of the ice, the oil droplets will form lenses (1–20 cm thick) in under-ice cavities, with the potential to infiltrate the porous bottommost layer of the ice (Karlsson et al., 2011; Oggier et al., 2020; Petrich et al., 2013). If a spill occurs during the ice growth season, the oil pool may become completely entrapped in sea ice cover within hours to days (NRC, 2014), limiting its further spreading. If ice is porous enough ($V_B > 5\%$), the oil may migrate towards the air-ice interface largely through brine channels (Karlsson et al., 2011; Oggier et al., 2020). Otherwise, it will primarily remain in place until the spring season, largely impeding the extent of weathering processes (Payne et al., 1991b). Subsequently, during spring melt, the oil will pool onto the ice surface, facilitating more profound weathering. The oil pooling will occur through a density-driven upward migration of oil *via* the warming and expanding brine channels or through ablation of the ice surface down to the oil pool (Fingas and Hollebone, 2003).

Transport of AHs from encapsulated oil may occur in growing sea ice through their dissolution in sea ice brine, followed by drainage of brine and associated compounds to the adjacent water column (Desmond et al., 2019; Faksness and Brandvik, 2008b; Vergeynst et al., 2019). In a study performed by Faksness and Brandvik (2008a), PAHs transported downward through the ice column showed a concentration gradient over time and a decrease in the concentration with ice depth. While the total PAH concentrations ranged between 2 and 16 $\mu g\ L^{-1}$, the exposure time reached nearly four months, suggesting potential for adverse effects to the local biota. Furthermore, due to its high density, cold and saline brine rejected from the growing ice matrix may sink to the deep ocean under quiescent conditions; AHs accommodated in the brine may therefore be transported in line with it to the seafloor, where they could persist for several months with potential for migration to benthic ecosystems (Payne et al., 1991a).

During the oil encapsulation in sea ice, AHs may also be subjected to transformation processes, in particular, biodegradation and photooxidation (Desmond et al., 2021; Vergeynst et al., 2019). Given the tendency of HMW PAH to attach to organic matter, they may potentially interact with ice-associated particles. However, so far, scientific efforts have not addressed the potential of these interactions and their effects on the local fauna and flora.

Overall, the presence of sea ice complicates the fate and behaviour of oil spills in polar oceans. Therefore, sea ice is often perceived as an obstacle in oil spill recovery and mitigation response, as well as in oil spill detection and monitoring. Conversely, by providing natural containment, sea ice cover facilitates a reduced rate and extent of oil spreading and most of the weathering processes, especially evaporation. This, in turn, contributes to decreased water uptake and evaporation, and a lower pour point, ultimately extending the time window for oil spill response activities, such as *in-situ* burning (ISB) (Fritt-Rasmussen et al., 2015), or chemical dispersion (Brandvik et al., 2006).

1.3 Knowledge Gaps

Several knowledge gaps substantially limit our understanding of how individual AHs move within the complex and dynamic sea ice, let alone their pathways, fate and exposures in sea ice infested with oil spills. The following section presents critical knowledge gaps pertaining to the fate and behaviour of AHs across the seawater-ice-atmosphere interface (summarized in Figure 1.3).

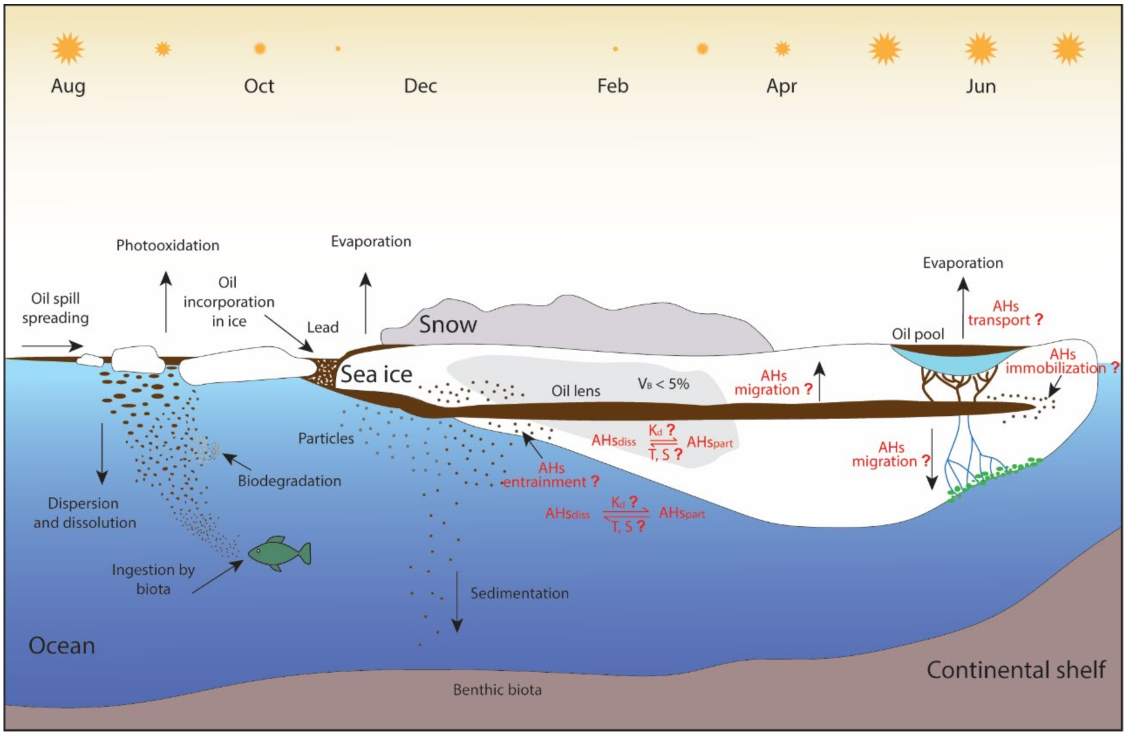

Figure 1.3. A conceptual schematic showing critical knowledge gaps pertaining to the behaviour of aromatic hydrocarbons (AHs) in sea ice. K_d, distribution coefficient; T, temperature; S, salinity; AHs_{diss}, dissolved aromatic hydrocarbons; AHs_{part}, particle-bound aromatic hydrocarbons; V_B, brine volume fraction.

1.3.1 Uncertainties regarding the mechanisms of aromatic hydrocarbon partitioning behaviour in the sea ice environment

The overall transport and distribution behaviour of AHs in the marine cryosphere can be inferred, to a limited extent, from studies describing some behavioural aspects of other organic contaminants, such as hexachlorocyclohexane (HCH) and per- and polyfluoroalkyl substances (PFAS) (Garnett et al., 2021; Garnett et al., 2019; Pućko et al., 2010a; Pućko et al., 2010b). However, substantial uncertainties exist around the mechanisms driving organic contaminant partitioning between various sea ice compartments, as well as a quantitative description of these processes (Mackay and Wania, 1995). More specifically, to date, scientific efforts have not addressed the partitioning of AHs between sea ice-associated particles and ice fluids, despite the general assumption that particles may have the potential to retain HMW PAHs in sea ice, therefore posing prolonged chronic exposure to the ice-associated biota (Yunker and Macdonald, 1995).

A more comprehensive understanding of these processes would vastly improve the assessment of the biological effects of AHs in sea ice and would be a prerequisite to the advancement of toxicity assessment models. This is particularly important since the existing data pertaining to the particle-liquid partition coefficients of some organic contaminants in marine ecosystems indicates an orders of magnitude greater propensity for the particulate matter than what would be assessed from commonly used organic matter partitioning models (Broman et al., 1991; Bucheli and Gustafsson, 2001).

Furthermore, empirical determination of distribution coefficients between particles and liquid phases (e.g., sea ice brine) for AHs, amongst other distribution coefficients, as well as their relations with thermodynamic properties of sea ice, are required to better appreciate the implications of the effects of altering climate in the Arctic environment.

1.3.2 Uncertainties regarding the transport and fate of aromatic hydrocarbons during oil spills in sea ice

A large body of knowledge has been generated since the 1970s on the mechanistic behaviour of oil in ice-covered polar oceans (for review see NRC, 2014); however, more clarity is required on the role of sea ice in the fractionation of toxic AHs from encapsulated oil lens, as well as their pathways across the seawater-ice-atmosphere interface. Specifically, it is not clear how the physicochemical properties of AHs, in concert with the geophysical characteristics of sea ice, determine which bulk ice compartment AHs are likely to partition to. Ultimately, it remains uncertain how they are further exchanged between seawater, sea ice and the atmosphere during the oil's residence in the ice cover. This is largely due to a sparse number of studies and limited quantitative data available with respect to the migration patterns of AHs in sea ice (Desmond et al., 2019; Faksness and Brandvik, 2008a, 2008b; Saltymakova et al., 2024). Thus, the comprehension of the biological effects of oil spills in Arctic waters on the local biota is hindered.

PAHs, in particular parent counterparts, have been at the forefront of oil spill research in aquatic environments. Meanwhile, rather limited efforts have been undertaken to quantitatively describe behaviours of alkylated PAHs, despite their now well-recognized greater potential for adverse effects than that of their parent counterparts. Additionally, the behaviour of the most volatile oil fractions, such as BTEX compounds and other alkylbenzenes, has also been somewhat overlooked in oil spill research, largely because of their rapid loss to the atmosphere. However, following entrapment of spilled oil within sea ice cover in Arctic waters, the potential for evaporation of AHs will be substantially hindered. As a result, their potential for dissolution in sea ice brine will likely increase, contributing to greater exposure on the ice and adjacent seawater biota (Payne et al., 1991a). Hence, for the toxicity assessment models to accurately forecast effects of oil spills on the Arctic marine organisms, quantitative studies including MAHs and alkylated PAHs are much more needed.

Quantitative data on oil weathering processes, especially on transport and dynamics of different types of oil and their components in the environment, with particular emphasis on oils abundantly transported within the Arctic (e.g., diesel fuel), is necessary for improvement and validation of algorithms in the current regional oil weathering models or development of new computations. These, in turn, are required for accurate oil spill detection and monitoring technologies, as well as for the implementation of proper oil spill clean-up strategies. Meanwhile, scientific efforts in this field are just in their infancy, emphasizing the need for further studies.

1.4 Thesis Structure

This Ph.D. thesis consists of five chapters. Chapter 1 (this chapter) provides a survey of the current state of knowledge and existing gaps on the topic of the fate and behaviour of AHs of petroleum in sea ice environments. Chapters 2 to 4 are individual manuscript-styled chapters based on a series of outdoor micro- and meso-scale experiments I carried out at the Sea-ice Environmental Research Facility (SERF) at the University of Manitoba during winter seasons of 2018, 2019 and 2020. These three chapters were designed to fill in the knowledge gaps highlighted in Section 1.3; each chapter consists of an abstract, introduction, methodology, results, discussion, and conclusions. Lastly, Chapter 5 provides a summary of the main findings and a reflection on encountered challenges and recommendations for future studies.

Chapter 2 investigates the fundamental mechanisms driving the distribution of four PAHs (naphthalene, phenanthrene, pyrene, benzo(a)pyrene) in experimental sea ice and seawater by studying their interphase partitioning between the aqueous phases (seawater, bulk sea ice) and particulate humic acid (a proxy for natural particulate organic carbon (POC)) over a 19-day ice growth period in outdoor microcosm-based experiment. The chapter provides the first empirical determination of the POC-aqueous phase partition coefficients, K_d, of the four PAHs in seawater and sea ice, and examines the combined effect of temperatures below 0°C and elevated salinities on the PAH K_ds. This study validates the use of the microcosm approach to probe the fundamental processes occurring in the sea ice environment. The results from this study were published in *Environmental Science and Technology* (Polcwiartek et al., 2025).

Chapter 3 builds on Chapter 2 by using the same microcosm approach to investigate the short-term (15 days) distribution behaviour and dynamics of a complex mixture of diesel fuel in a diesel-in-ice outdoor experiment. The study reports the temporal evolution of the transport of bulk diesel and its 46 AHs between the experimental seawater and sea ice, as well as estimated potential atmospheric loss, providing an important dataset that can aid remote sensing-based oil detection and monitoring technologies, oil weathering and toxicity assessment models. This chapter also investigates relationships between the relative fractions of individual AHs in seawater, sea ice, and potential losses with their respective K_{OW} and K_H values, shedding light on the role of physicochemical properties of AHs in their transport and distribution patterns in such complex and dynamic environments as young growing sea ice. The research paper based on this chapter is in preparation for journal submission.

Chapter 4 is an extension of Chapters 2 and 3. Here, we apply a larger-scale approach, namely a mesocosm-based experiment, to study a longer-term distribution behaviour of the most volatile and water-soluble AHs in a crude oil-in-ice spill scenario. The chapter investigates the downward and upward distribution of 39 AHs, specifically BTEX compounds and other alkylbenzenes, as well as alkylnaphthalenes, in the experimental sea ice cover from an encapsulated crude oil lens over a 77-day ice growth-melt season. Moreover, this work derives empirical equations predicting the relative concentrations of the studied AHs from their respective K_{OW} and K_H values, contributing to the improvement of the existing toxicity assessment models developed for oil component transport in sea ice environments. The research paper for this chapter is in preparation for journal submission.

References

Afenyo, M., Veitch, B., & Khan, F. 2016. A state-of-the-art review of fate and transport of oil spills in open and ice-covered water. Ocean Engineering, 119: 233-248.

Agarkov, S., Matviishin, D., & Gutman, S. 2019. Environmental status of continental shelf in the Pechora Sea: analysis and recommendations. IOP conference series. Earth and Environmental Science, 302: 121–144.

AMAP. 1998. Assessment Report: Arctic Pollution Issues. Arctic Monitoring and Assessment Programme (AMAP). Oslo, Norway. xii–859.

AMAP. 2010. Assessment 2007: Oil and Gas Activities in the Arctic – Effects and Potential Effects. Volume 2. Arctic Monitoring and Assessment Programme (AMAP). Oslo, Norway. vii–277.

AMAP. 2017. Chemicals of Emerging Arctic Concern. Summary for Policy-makers. Arctic Monitoring and Assessment Programme (AMAP). Oslo, Norway. 16.

Andrews, J., Babb, D., & Barber, D. G. 2017. Climate change and sea ice: Shipping accessibility on the marine transportation corridor through Hudson Bay and Hudson Strait (1980–2014). Elementa: Science of the Anthropocene, 5: 15.

Arctic Council. 2025. Arctic Shipping on the Rise: What Trends Can Tell Us. https://arctic-council.org/news/arctic-shipping-what-trends-can-tell-us/#:~:text=May%2012%2C%202025&text=Access%20to%20the%20Arctic%20Ocean,previously%20difficult%20to%20reach%20regions. Accessed June 10, 2025.

Babb, D. G., Galley, R. J., Kirillov, S., Landy, J. C., Howell, S. E. L., Stroeve, J. C., Meier, W., Ehn, J. K., & Barber, D. G. 2023. The Stepwise Reduction of Multiyear Sea Ice Area in the Arctic Ocean Since 1980. Journal of Geophysical Research: Oceans, 128: 1–19.

Barron, M. G., & Holder, E. 2003. Are Exposure and Ecological Risks of PAHs Underestimated at Petroleum Contaminated Sites?. Human and Ecological Risk Assessment, 9: 1533-1545.

Berkowitz, B. D., I.; Yaron, B. 2008. Contaminant Partitioning in the Aqueous Phase. In B. Berkowitz (Ed.). Contaminant geochemistry: interactions and transport in the subsurface environment. Springer Berlin Heidelberg: 127–141.

Bezmaternykh, D. M., Puzanov, A. V., Kotovshchikov, A. V., Drobotov, A. V., & Tolomeev, A. P. 2021. Hydrochemical Indicators of Water Quality in the Norilsk–Pyasino Lake–River

System after a Diesel Fuel Spill at Norilsk Heat and Power Plant 3 in 2020. Contemporary Problems of Ecology, 14: 323–334.

Bishop, Bremner, Laake, A., Strobia, Parno, & Utskot. 2011. Petroleum Potential of the Arctic: Challenges and Solutions, 22.

Bornstein, J. M., Adams, J., Hollebone, B., King, T., Hodson, P. V., & Brown, R. S. 2014. Effects-driven chemical fractionation of heavy fuel oil to isolate compounds toxic to trout embryos. Environmental Toxicology and Chemistry, 33: 814–824.

Brandvik, P., Sørheim, K., Singsaas, I., & Reed, M. 2006. Short state-of-the-art report on oil spills in ice-infested waters. Oil in ice - JIP. SINTEF.

Brandvik, P. J., & Faksness, L.-G. 2009. Weathering processes in Arctic oil spills: meso-scale experiments with different ice conditions. Cold Regions Science and Technology, 55: 160–166.

Broman, D., Naef, C., Rolff, C., & Zebuehr, Y. 1991. Occurrence and dynamics of polychlorinated dibenzo-p-dioxins and dibenzofurans and polycyclic aromatic hydrocarbons in the mixed surface layer of remote coastal and offshore waters of the Baltic. Environmental Science and Technology, 25: 1850–1864.

Bucheli, T. D., & Gustafsson, Ö. 2001. Ubiquitous observations of enhanced solid affinities for aromatic organochlorines in field situations: Are in situ dissolved exposures overestimated by existing partitioning models?. Environmental Toxicology and Chemistry, 20: 1450–1456.

Cammaert, A. B. 1980. Oil and Gas under Ice Laboratory Study. No. RWC17. Canadian Marine Drilling Ltd. and Canada Environmental Protection Service.

Canadian Council of Ministers of the Environment. 1999. Canadian water quality guidelines for the protection of aquatic life - Polycyclic aromatic hydrocarbons.

Canadian Environmental Protection Act. 1999. Canadian Environmental Protection Act: First Priority Substances List.

Carayannis, E. G., Ilinova, A., & Cherepovitsyn, A. 2021. The Future of Energy and the Case of the Arctic Offshore: The Role of Strategic Management. Journal of Marine Science and Engineering, 9: 134.

Carls, M. G., Rice, S. D., & Hose, J. E. 1999. Sensitivity of fish embryos to weathered crude oil: Part I. Low-level exposure during incubation causes malformations, genetic damage, and mortality in larval Pacific herring (Clupea pallasi). Environmental Toxicology and Chemistry, 18: 481–493.

Chaulk, A., Stern, G. A., Armstrong, D., Barber, D. G., & Wang, F. 2011. Mercury distribution and transport across the ocean-sea-ice-atmosphere interface in the Arctic Ocean. Environmental Science and Technology, 45: 1866–1872.

Christiansen, F. G. 2021. Greenland petroleum exploration history: Rise and fall, learnings, and future perspectives. Resources Policy, 74: 102–425.

Comer, B., Olmer, N., & Mao, X. 2016. Heavy fuel oil use in Arctic shipping in 2015. Accessed in June 2025.

Cox, G. F. N., & Weeks, W. F. 1975. Brine drainage and initial salt entrapment in sodium chloride ice. Polar Continental Shelf Project (Canada).

Daling, P. S., Cooper, D., Buist, I., Faksness, L. G., Altin, D., Pettersen, T., & Bakken, O. M. 2020. Characterization of Low Sulfur Fuel Oils (LSFO) – A new generation of marine fuel oils.

Dawson, J., Pizzolato, L., Howell, S. E. L., Copland, L., & Johnston, M. E. 2018. Temporal and Spatial Patterns of Ship Traffic in the Canadian Arctic from 1990 to 2015. Arctic, 71: 15–26.

Dawson, J., Stewart, E. J., Johnston, M. E., & Lemieux, C. J. 2016. Identifying and evaluating adaptation strategies for cruise tourism in Arctic Canada. Journal of Sustainable Tourism, 24: 1425–1441.

Desmond, D. S., Saltymakova, D., Neusitzer, T. D., Firoozy, N., Isleifson, D., Barber, D. G., & Stern, G. A. 2019. Oil behavior in sea ice: Changes in chemical composition and resultant effect on sea ice dielectrics. Marine Pollution Bulletin, 142: 216–233.

Desmond, D. S., Saltymakova, D., Smith, A., Wolfe, T., Snyder, N., Polcwiartek, K., Bautista, M., Lemes, M., Hubert, C. R. J., Barber, D. G., Isleifson, D., & Stern, G. A. 2021. Photooxidation and biodegradation potential of a light crude oil in first-year sea ice. Marine Pollution Bulletin, 165: 112–154.

Dzyublo, A. D., Sidorov, V. V., Zonn, M. S., & Agadzhanyants, I. G. 2021. The Oil and Gas Potential of the Ordovician–Lower Frasnian Megacomplex of the Pechora Sea Shelf. Moscow University Geology Bulletin, 76: 538–549.

Eguíluz, V. M., Fernández-Gracia, J., Irigoien, X., & Duarte, C. M. 2016. A quantitative assessment of Arctic shipping in 2010–2014. Scientific Reports, 6: 30682.

Environmental Monitoring of Svalbard and Jan Mayen (MOSJ). 2025. Marine and coastal tourism. https://mosj.no/en/indikator/influence/traffic/cruise-and-coastal-tourism/. Accessed June 10, 2025.

Faksness, L.-G., & Brandvik, P. J. 2008a. Distribution of water-soluble components from Arctic marine oil spills – A combined laboratory and field study. Cold Regions Science and Technology, 54: 97–105.

Faksness, L.-G., & Brandvik, P. J. 2008b. Distribution of water-soluble components from oil encapsulated in Arctic sea ice: Summary of three field seasons. Cold Regions Science and Technology, 54: 106–114.

Fingas, M. 2015. Introduction to Oil Chemistry and Properties. In Handbook of Oil Spill Science and Technology. John Wiley & Sons. 51–77.

Fingas, M. F., & Hollebone, B. P. 2003. Review of behaviour of oil in freezing environments. Marine Pollution Bulletin, 47: 333–340.

French-McCay, D. P. 2004. Oil spill impact modeling: Development and validation. Environmental Toxicology and Chemistry, 23: 2441–2456.

Fritt-Rasmussen, J., Wegeberg, S., & Gustavson, K. 2015. Review on Burn Residues from In Situ Burning of Oil Spills in Relation to Arctic Waters. Water, air, and soil pollution, 226: 1-12.

Gagnaire, F., & Langlais, C. 2005. Relative ototoxicity of 21 aromatic solvents. Archives of Toxicology, 79: 346–354.

Garnett, J., Halsall, C., Thomas, M., Crabeck, O., France, J., Joerss, H., Ebinghaus, R., Kaiser, J., Leeson, A., & Wynn, P. M. 2021. Investigating the Uptake and Fate of Poly- and Perfluoroalkylated Substances (PFAS) in Sea Ice Using an Experimental Sea Ice Chamber. Environmental Science and Technology, 55: 9601–9608.

Garnett, J., Halsall, C., Thomas, M., France, J., Kaiser, J., Graf, C., Leeson, A., & Wynn, P. 2019. Mechanistic Insight into the Uptake and Fate of Persistent Organic Pollutants in Sea Ice. Environmental Science and Technology, 53: 6757–6764.

Gascard, J. C., Zhang, J., & Rafizadeh, M. 2019. Rapid decline of Arctic sea ice volume: Causes and consequences. The Cryosphere Discuss., 2019: 1–29.

Gautier, D. L., Bird, K. J., Charpentier, R. R., Grantz, A., Houseknecht, D. W., Klett, T. R., Moore, T. E., Pitman, J. K., Schenk, C. J., Schuenemeyer, J. H., Sørensen, K., Tennyson, M. E., Valin, Z. C., & Wandrey, C. J. 2009. Assessment of Undiscovered Oil and Gas in the Arctic. Science (American Association for the Advancement of Science), 324: 1175-1179.

Gearing, J. N., & Gearing, P. J. 1983. Suspended Load and Solubility Affect Sedimentation of Petroleum Hydrocarbons in Controlled Estuarine Ecosystems. Canadian journal of fisheries and aquatic sciences, 40: 54–62.

Glyaznetsova, Y. S., Nemirovskaya, I. A., & Flint, M. V. 2021. Study of the Effects of an Accidental Diesel Fuel Spill in Norilsk. Doklady Earth Sciences, 501: 994–999.

Golden, K. M., Ackley, S. F., & Lytle, V. I. 1998. The Percolation Phase Transition in Sea Ice. Science, 282: 2238–2241.

Golden, K. M., Eicken, H., Heaton, A. L., Miner, J., Pringle, D. J., & Zhu, J. 2007. Thermal evolution of permeability and microstructure in sea ice. Geophysical Research Letters, 34: 1–6.

Heinrich, M. 2003. IARC Monographs on the Evaluation of Carcinogenic Risks to Humans: Some Traditional Herbal Medicines, Some Mycotoxins, Naphthalene and Styrene: IARC Working Group on the Evaluation of Carcinogenic Risks to Humans, 2002, Lyon (France), International Agency for Research on Cancer (IARC) IARC Monographs on the Evaluation of Carcinogenic Risks to Humans, 82: 1–594.

Henderson, J., & Loe, J. 2014. The Prospects and Challenges for Arctic Oil Development (Publisher's version). The Oxford Institute for Energy Studies, 1–60.

Hodson, P. V., Qureshi, K., Noble, C. A. J., Akhtar, P., & Brown, R. S. 2007. Inhibition of CYP1A enzymes by α-naphthoflavone causes both synergism and antagonism of retene toxicity to rainbow trout (Oncorhynchus mykiss). Aquatic Toxicology, 81: 275–285.

Johnson, W., Idowu, I., Francisco, O., Marvin, C., Thomas, P. J., Stetefeld, J., & Tomy, G. T. 2018. Enumeration of the constitutional isomers of environmentally relevant substituted polycyclic aromatic compounds. Chemosphere, 202: 9–16.

Johnston, A., Johnston, M., Stewart, E., Dawson, J., & Lemelin, H. 2012. Perspectives of decision makers and regulators on climate change and adaptation in expedition cruise ship tourism in Nunavut. Northern Review (Whitehorse), 35: 1–69.

Karlsson, J., Petrich, C., & Eicken, H. 2011. Oil entrainment and migration in laboratory-grown saltwater ice. Proceedings of the International Conference on Port and Ocean Engineering under Arctic Conditions, POAC, 1: 88–97.

Lackenbauer, W., & Lajeunesse, A. 2014. On Uncertain Ice: The Future of Arctic Shipping and the Northwest Passage. The School of Public Policy. Canadian Defence & Foreign Affairs Institute, 1–11.

Lee, K., Boudreau, M., Bugden, J., Burridge, L., Cobanli, S. E., Courtenay, S., Grenon, S., Hollebone, B., Kepkay, P., Li, Z., Lyons, M., Niu, H., King, T., MacDonald, S., McIntyre, E. C., Robinson, B., Ryan, S. A., & Wohlgeschaffen, G. 2011. State of Knowledge Review of Fate and Effect of Oil in the Arctic Marine Environment. A report prepared for the National Energy Board of Canada Arctic Roundtable: State-of-Knowledge Review of Fate and Effects of Oil in Arctic Offshore, 1–257.

Lee, K., Boufadel, M., Chen, B., Foght, J., Hodson, P., Swansons, S., & Venosa, A. 2015. The Royal Society of Canada Expert Panel: The Behaviour and Environmental Impacts of Crude Oil Released into Aquatic Environments. 1–460.

Liu, B., Gao, L., Ding, L., Lv, L., & Yu, Y. 2023. Trophodynamics and bioaccumulation of polycyclic aromatic hydrocarbons (PAHs) in marine food web from Laizhou Bay, China. Marine Pollution Bulletin, 194 (Part B): 1–10.

Loose, B., Schlosser, P., Perovich, D., Ringelberg, D., Ho, D. T., Takahashi, T., Richter-Menge, J., Reynolds, C. M., McGillis, W. R., & Tison, J. L. 2011. Gas diffusion through columnar laboratory sea ice: implications for mixed-layer ventilation of CO_2 in the seasonal ice zone. Tellus, 63: 23–39.

Ma, Y., Xie, Z., Yang, H., Möller, A., Halsall, C., Cai, M., Sturm, R., & Ebinghaus, R. 2013. Deposition of polycyclic aromatic hydrocarbons in the North Pacific and the Arctic. Journal of Geophysical Research: Atmospheres, 118: 5822–5829.

Macdonald, R. W., Barrie, L. A., Bidleman, T. F., Diamond, M. L., Gregor, D. J., Semkin, R. G., Strachan, W. M. J., Li, Y. F., Wania, F., Alaee, M., Alexeeva, L. B., Backus, S. M., Bailey, R., Bewers, J. M., Gobeil, C., Halsall, C. J., Harner, T., Hoff, J. T., Jantunen, L. M. M., . . . Yunker, M. B. 2000. Contaminants in the Canadian Arctic: 5 years of progress in understanding sources, occurrence and pathways. Science of The Total Environment, 254: 93–234.

Mackay, D., & Wania, F. 1995. Transport of contaminants to the Arctic: partitioning, processes and models. Science of The Total Environment, 160: 25–38.

Meador, J. P., Casillas, E., Sloan, C. A., & Varanasi, U. 1995. Comparative bioaccumulation of polycyclic aromatic hydrocarbons from sediment by two infaunal invertebrates. Marine Ecology, 123: 107–124.

Meyer, T., Lei, Y. D., Muradi, I., & Wania, F. 2009a. Organic Contaminant Release from Melting Snow. 1. Influence of Chemical Partitioning. Environmental Science and Technology, 43: 657–662.

Meyer, T., Lei, Y. D., Muradi, I., & Wania, F. 2009b. Organic contaminant release from melting snow. 2. Influence of snow pack and melt characteristics. Environ Science and Technology, 43: 663–668.

Miller, C. J. 2025. Restricting Oil and Gas Leases through Withdrawals under OCSLA: Can a President Rescind? Env't L. Rep., 55: 10153.

Mishra, A. K., & Kumar, G. S. 2015. Weathering of Oil Spill: Modeling and Analysis. Aquatic Procedia, 4: 435–442.

NASA. 2025. Arctic Sea Ice Minimum Extent. https://climate.nasa.gov/vital-signs/arctic-sea-ice/?intent=121. Accessed June 12, 2025.

National Research Council. 2003. Oil in the Sea III: Inputs, Fates, and Effects. The National Academies Press. 1–29.

National Research Council. 2014. Responding to oil spills in the U.S. Arctic Marine environment (1st ed.). The National Academies Press. 1–195.

National Toxicology Program. 2011. National Toxicology Program: 12th report on carcinogens. Report on carcinogens: carcinogen profiles. 12: 1–499

Noh, J., Kim, H., Lee, C., Yoon, S. J., Chu, S., Kwon, B.-O., Ryu, J., Kim, J.-J., Lee, H., Yim, U. H., Giesy, J. P., & Khim, J. S. 2018. Bioaccumulation of Polycyclic Aromatic Hydrocarbons (PAHs) by the Marine Clam, Mactra veneriformis, Chronically Exposed to Oil-Suspended Particulate Matter Aggregates. Environmental Science and Technology, 52: 7910–7920.

Notz, D., & Stroeve, J. 2018. The Trajectory Towards a Seasonally Ice-Free Arctic Ocean. Current Climate Change Reports, 4: 407–416.

Oggier, M., Eicken, H., Wilkinson, J., Petrich, C., & O'Sadnick, M. 2020. Crude oil migration in sea-ice: Laboratory studies of constraints on oil mobilization and seasonal evolution. Cold Regions Science and Technology, 174: 1–16.

PAME. 2020. Heavy Fuel Oil (HFO) Use By Ships in the Arctic 2019. Arctic Shipping Status Report (ASSR) #2.

Pampanin, D., & Sydnes, M. O. 2013. Polycyclic Aromatic Hydrocarbons: A Constituent of Petroleum: Presence and Influence in the Aquatic Environment. In Hydrocarbon. 83–118.

Payne, J. R., Clayton, J. R., & Kirstein, B. E. 2003. Oil Suspended Particulate Material Interactions and Sedimentation. Spill Science and Technology Bulletin, 8: 201–221.

Payne, J. R., Hachmeister, L. E., McNabb, G. D., Sharpe, H. E., Smith, G. S., & Menen, C. A. 1991a. Brine-induced advection of dissolved aromatic hydrocarbons to Arctic bottom waters. Environmental Science and Technology, 25: 940–951.

Payne, J. R., McNabb Jr, G. D., & Clayton. Jr, J. R. 1991b. Oil-weathering behavior in Arctic environments. Polar Research, 10: 631–662.

Peng, L., Lin, Y., Meng, F., Wu, J., Zheng, Y., Sun, T., & Wang, G. 2021. Environmental fate and aquatic effects of propylbenzenes and trimethylbenzenes: A review. Chemosphere, 264 (Part 2): 1–10.

Petrich, C., Karlsson, J., & Eicken, H. 2013. Porosity of growing sea ice and potential for oil entrainment. Cold Regions Science and Technology, 87: 27–32.

Pizzolato, L., Howell, S. E. L., Dawson, J., Laliberté, F., & Copland, L. 2016. The influence of declining sea ice on shipping activity in the Canadian Arctic. Geophysical Research Letters, 43: 146–154.

Pizzolato, L., Howell, S. E. L., Derksen, C., Dawson, J., & Copland, L. 2014. Changing sea ice conditions and marine transportation activity in Canadian Arctic waters between 1990 and 2012. Climatic Change, 123: 161–173.

Polcwiartek, K., Stern, G. A., & Wang, F. 2025. Incorporation and Distribution of Polycyclic Aromatic Hydrocarbons in Experimental Sea-Ice. Environmental Science and Technology, 59: 7310–7319.

Pruell, R. J., Lake, J. L., Davis, W. R., & Quinn, J. G. 1986. Uptake and depuration of organic contaminants by blue mussels (Mytilus edulis) exposed to environmentally contaminated sediment. Marine Biology, 91: 497–507.

Pućko, M., Stern, G. A., Barber, D. G., Macdonald, R. W., & Rosenberg, B. 2010a. The international polar year (IPY) circumpolar flaw lead (CFL) system study: The importance of brine processes for α- and γ-hexachlorocyclohexane (HCH) accumulation or rejection in sea ice. Atmosphere-Ocean, 48: 244–262.

Pućko, M., Stern, G. A., Macdonald, R. W., & Barber, D. G. 2010b. α- and γ-hexachlorocyclohexane measurements in the brine fraction of sea ice in the Canadian High Arctic using a sump-hole technique. Environmental Science and Technology, 44: 9258–9264.

Pućko, M., Stern, G. A., Macdonald, R. W., Jantunen, L. M., Bidleman, T. F., Wong, F., Barber, D. G., & Rysgaard, S. 2015. The delivery of organic contaminants to the Arctic food web: why sea ice matters. Science of Total Environment, 506–507: 444–452.

Rantanen, M., Karpechko, A. Y., Lipponen, A., Nordling, K., Hyvärinen, O., Ruosteenoja, K., Vihma, T., & Laaksonen, A. 2022. The Arctic has warmed nearly four times faster than the globe since 1979. Communications Earth and Environment, 3: 1–10.

Riazi, M. R., & Edalat, M. 1996. Prediction of the rate of oil removal from seawater by evaporation and dissolution. Journal of Petroleum Science and Engineering, 16: 291–300.

Saltymakova, D., Desmond, D. S., Galley, R., Polcwiartek, K., Neusitzer, T. D., Firoozy, N., Barber, D. G., & Stern, G. A. 2024. The influence of sea-ice conditions on crude oil spill behaviour. Cold Regions Science and Technology, 221: 104160.

Schwarzenbach, R. P., Gschwend, P. M., & Imboden, D. M. 2016. Environmental Organic Chemistry, 3rd Edition, Wiley, 213–317.

Shapovalova, D., & Stephen, K. 2019. No race for the Arctic? Examination of interconnections between legal regimes for offshore petroleum licensing and level of industry activity. Energy Policy, 129: 907–917.

Stewart, E. J., & Dawson, J. 2011. A Matter of Good Fortune? The Grounding of the "Clipper Adventurer" in the Northwest Passage, Arctic Canada. Arctic, 64: 263–267.

Stewart, E. J., Dawson, J., Howell, S. E. L., Johnston, M. E., Pearce, T., & Lemelin, H. 2013. Local-level responses to sea ice change and cruise tourism in Arctic Canada's Northwest Passage. Polar Geography, 36: 142–162.

Stewart, E. J., Howell, S. E. L., Draper, D., Yackel, J., & Tivy, A. 2007. Sea Ice in Canada's Arctic: Implications for Cruise Tourism. Arctic, 60: 370–380.

Stroeve, J., Holland, M. M., Meier, W., Scambos, T., & Serreze, M. 2007. Arctic sea ice decline: Faster than forecast. Geophysical Research Letters, 34: 1–5.

Stroeve, J. C., Kattsov, V., Barrett, A., Serreze, M., Pavlova, T., Holland, M., & Meier, W. N. 2012. Trends in Arctic sea ice extent from CMIP5, CMIP3 and observations. Geophysical Research Letters, 39: 1–7.

Stroeve, J. C., Markus, T., Boisvert, L., Miller, J., & Barrett, A. 2014. Changes in Arctic melt season and implications for sea ice loss. Geophysical Research Letters, 41: 1216–1225.

Thomas, D. N. 2016. Sea Ice (Third edition). Wiley.

Tison, J.-L., Delille, B., & Papadimitriou, S. 2017. Gases in sea ice. In Sea Ice. 433–471.

Turcotte, D., Akhtar, P., Bowerman, M., Kiparissis, Y., Brown, R. S., & Hodson, P. V. 2011. Measuring the toxicity of alkyl-phenanthrenes to early life stages of medaka (Oryzias latipes) using partition-controlled delivery. Environmental Toxicology and Chemistry, 30: 487–495.

Tysiąc, P., Strelets, T., & Tuszyńska, W. 2022. The Application of Satellite Image Analysis in Oil Spill Detection. Applied Sciences, 12: 4016.

Ucan-Marin, F., & Dupuis, A. 2015. A literature review on the aquatic toxicology of petroleum oil: An overview of oil properties and effects to aquatic biota. Canadian Science Advisory Secretariat (CSAS), 007: 52.

U.S. Environmental Protection Agency. 1987. Priority Pollutant PAHs.

USGS. 2008. U.S. Geological Survey (USGS) Circum-Arctic Resource Appraisal: Estimates of Undiscovered Oil and Gas North of the Arctic Circle. U.S. Department of the Interior, U.S. Geological Survey. http://library.arcticportal.org/1554/. Accessed May 13, 2025.

Venkatesh, S., El-Tahan, H., Comfort, G., & Abdelnour, R. 1990. Modelling the behaviour of oil spills in ice-infested waters. Atmosphere-Ocean, 28: 303–329.

Vergeynst, L., Greer, C. W., Mosbech, A., Gustavson, K., Meire, L., Poulsen, K. G., & Christensen, J. H. 2019. Biodegradation, Photo-oxidation, and Dissolution of Petroleum Compounds in an Arctic Fjord during Summer. Environmental Science and Technology, 53: 12197–12206.

Wang, F., Pućko, M., & Stern, G. 2017. Transport and transformation of contaminants in sea ice. In Sea Ice, 472–491.

Wang, Z., & Stout, S. 2016. Chemical Fingerprinting Methods and Factors Affecting Petroleum Fingerprints in the Environment. In Standard Handbook Oil Spill Environmental Forensics, 61–117.

Wang, Z. D., Fingas, M., Landriault, M., Sigouin, L., & Xu, N. N. 1995. Identification of Alkylbenzenes and Direct Determination of BTEX and (BTEX + C3-Benzenes) in Oils by GC/MS. Analytical Chemistry, 67: 3491–3500.

Whitehouse, B. G. 1984. The effects of temperature and salinity on the aqueous solubility of polynuclear aromatic hydrocarbons. Marine Chemistry, 14: 319–332.

Wiaderna, D., Gralewicz, S., & Tomas, T. 2002. Assessment of long-term neurotoxic effects of exposure to mesitylene (1,3,5-trimethylbenzene) based on the analysis of selected behavioral responses. International Journal of Occupational Medicine and Environmental Health, 15: 385–391.

Wilkinson, J., Beegle-Krause, C. J., Evers, K.-U., Hughes, N., Lewis, A., Reed, M., & Wadhams, P. 2017. Oil spill response capabilities and technologies for ice-covered Arctic marine waters: A review of recent developments and established practices. Ambio, 46 (Suppl 3): S423–S441.

Williams, S. D., Ladd, D. E., & Farmer, J. J. 2006. Fate and Transport of Petroleum Hydrocarbons in Soil and Ground Water at Big South Fork National River and Recreation Area, Tennessee and Kentucky, 2002-2003: U.S. Geological Survey Scientific Investigations Report, 2005–5104.

Yan, J., Wang, L., Fu, P. P., & Yu, H. 2004. Photomutagenicity of 16 polycyclic aromatic hydrocarbons from the US EPA priority pollutant list. Mutation Research Genetic Toxicology and Environmental Mutagenesis, 557: 99–108.

Yunker, M. B., & Macdonald, R. W. 1995. Composition and Origins of Polycyclic Aromatic Hydrocarbons in the Mackenzie River and on the Beaufort Sea Shelf. Arctic, 48: 118–129.

Zhang, L., Ma, Y., Vojta, S., Morales-Mcdevitt, M., Hoppmann, M., Soltwedel, T., Kirk, J., De Silva, A., Muir, D., & Lohmann, R. 2023. Presence, Sources and Transport of Polycyclic Aromatic Hydrocarbons in the Arctic Ocean. Geophysical Research Letters, 50: 1–12.

Zhou, J., Delille, B., Eicken, H., Vancoppenolle, M., Brabant, F., Carnat, G., Geilfus, N. X., Papakyriakou, T., Heinesch, B., & Tison, J. L. 2013. Physical and biogeochemical properties in landfast sea ice (Barrow, Alaska): Insights on brine and gas dynamics across seasons. Journal of Geophysical Research: Oceans, 118: 3172–3189.

Chapter 2 Incorporation and Distribution of Polycyclic Aromatic Hydrocarbons in Experimental Sea Ice

This chapter examines the distribution behaviour and particle-liquid partitioning of four PAHs in experimental sea ice and seawater. The particle-liquid partitioning is a fundamental process controlling the distribution of contaminants in the natural environment, yet its mechanisms have not been studied experimentally in the sea ice environment. This chapter also introduces a unique microcosm approach for studying the fate of contaminants in the sea ice environment. The research paper has been published in *Environmental Science and Technology* (Polcwiartek et al., 2025).

Contributions of Authors

I designed the experiment, planned the sampling strategy and developed methods for sample processing under the supervision of Dr. Feiyue Wang (FW) and Dr. Gary Stern (GS). I performed the sampling collection with the help of Dr. Cathrin Veenaas (CV). I processed the samples, developed analytical methodology and performed the instrumental analysis. I worked with FW and GS on the data processing, visualization and interpretation. I prepared the manuscript with substantial contributions from FW and GS.

Abstract

Rapid melting of sea ice is making the Arctic more accessible for marine shipping and other industrial activities, increasing the risk of oil spills in the Arctic Ocean. PAHs are among the most toxic substances in petroleum oil, yet their behaviour in sea ice-covered waters remains poorly studied. Here we report an outdoor microcosm study to examine the partitioning behaviour of four PAHs (naphthalene, phenanthrene, pyrene and benzo(a)pyrene) across the seawater-sea ice-atmosphere interface in the presence of particulate humic acid as a surrogate for POC. We show that the higher the molecular weight of the PAH, the higher its concentration in sea ice and the POC fraction. The POC-aqueous phase (seawater or bulk sea ice) partition coefficients are reasonably well explained by temperature and salinity for all four PAHs in seawater and for phenanthrene and pyrene in sea ice. Relationships of K_d with temperature and salinity in sea ice and freezing seawater are complex and nonunidirectional, most likely due to the dynamic nature of sea ice and seawater under such temperatures. This suggests that conventional equilibrium-based approaches developed for open-water conditions need to be revisited when describing the behaviour of PAHs in ice-covered waters.

2.1 Introduction

PAHs are an emerging concern in the Arctic (AMAP, 2017, 2021) due to projected increases in marine shipping (Dawson et al., 2018) and fossil fuel extraction activities as climate change makes the Arctic more accessible. Other sources of PAHs to the Arctic include tundra or forest fires in and around the Arctic and long-range transport from lower latitudes. PAHs have been shown to cause adverse effects to both Arctic sea ice communities (Hatlen et al., 2009) and marine biota (Carls et al., 1999; Hannam et al., 2010). Yet, the role of sea ice in the fate and transport of PAHs in the Arctic remains poorly understood.

Distribution of PAHs across the seawater-ice-atmosphere interface is governed by both the physicochemical properties of PAHs and the dynamic processes in the marine cryosphere, especially the movement of brine and air bubbles in sea ice. Distribution of gaseous chemicals between sea ice and seawater has been shown to be driven by buoyant air bubble transfer or diffusion (Crabeck et al., 2014), whereas water-soluble compounds accommodated in the brine are distributed by the brine dynamics (Garnett et al., 2021; Pućko et al., 2010; Wang et al., 2017). Therefore, relationships between salinity and solutes in sea ice are used in experimental (Garnett et al., 2021) and modelling (Thomas et al., 2023) studies to assess and predict the way in which chemicals are incorporated and rejected from sea ice. However, more hydrophobic contaminants, such as PFAS, are not necessarily transported conservatively with respect to brine, likely due to their partitioning to solid ice interstitial surfaces (Garnett et al., 2021). This may play a significant role in the distribution, transformation and environmental impacts of PAHs, especially HMW PAHs, in sea ice containing POC (Eicken et al., 2005; Macdonald et al., 2000; Wang et al., 2017). Studies on the Antarctic sea ice (Duprat et al., 2019; Duprat et al., 2021; Lannuzel et al., 2011) have shown that particle-bound metal fractions were partially immobilized on brine channel surfaces due to particle sorption to ice crystal surfaces, which separated them from brine and subsequently led to their retention in sea ice. However, no studies have examined the partitioning of organic contaminants to sea ice POC and its impact on contaminant distribution, retention in sea ice and exposure pathways to the local biota.

Partitioning of PAHs between the aqueous phase and POC has implications for their toxicity, bioavailability, transport and overall fate in the environment. It is a solubility-driven process that is quantitatively described by the K_d, which is affected by both physicochemical properties of the PAH and environmental parameters such as temperature and salinity (Schwarzenbach et al., 2016). Studies have examined K_d values of PAHs in seawater at above water-freezing temperatures (Brunk et al., 1997; Means et al., 1980; Zhou et al., 1999), but data are scarce for conditions relevant to polar oceans (Finizio and Di Guardo, 2001), especially in seawater and sea ice brine at or below water-freezing temperatures. As such, it remains unknown whether the existing environmental models are sufficient to describe the transport, transformation, and effects of PAHs and other contaminants in cold environments (Wang et al., 2017).

To fill this critical knowledge gap, here we report the results of an outdoor sea ice microcosm experiment on the behaviour of four PAHs of differing physicochemical properties (naphthalene, (NAP), phenanthrene (PHE), pyrene (PYR), and benzo(a)pyrene (BaPYR)) in the presence of POC. We studied the distribution of the PAHs across the seawater-ice-atmosphere interface, examined their partitioning behaviour between the dissolved and particulate phases in both the ice matrix and the underlying water column, determined their K_d values in ice and seawater, and investigated the combined effect of freezing temperature and salinity on the K_d values.

2.2 Materials and Methods

2.2.1 Experimental setup

An outdoor sea ice microcosm experiment was conducted from February 24 to March 16, 2020, at the University of Manitoba's SERF in Winnipeg, Canada. Six funnel-shaped fibreglass containers (5 replicates and a control), each with a 260 L capacity (Figure A1 in Appendix A), were exposed to outdoor winter conditions. The experiment simulated the seasonal evolution of natural sea ice.

Each microcosm was filled with approximately 240 L of artificial seawater formulated from groundwater and salts, with a salinity and major ion composition resembling that of standard seawater at a salinity of 33, similar to surface Arctic seawater. A detailed description of the artificial seawater preparation can be found in the study by Gao et al. (2024). The water in five of the six microcosms was spiked with 0.7 g of particulate humic acid and stirred with a rod to distribute it as evenly as possible throughout each microcosm, reaching final concentrations of approximately 2.9 mg L^{-1}. Humic acid has previously been used as a surrogate for POC in studies involving snow (Meyer et al., 2009; Meyer et al., 2006) and marine particles (Tremblay et al., 2005). In the current study, the particulate humic acid was prepared by mixing about 15 g of humic acid (Sigma Aldrich) with 6 L of filtered artificial seawater from SERF, followed by filtering with 0.7 µm glass microfiber filters (GF/F, Whatman) to remove the water-soluble fraction. The particulate humic acid fraction retained on the filters was dried at 65 °C overnight and used to spike each of the five microcosms. The sixth microcosm was designated as a control and was not spiked with humic acid.

Four PAHs, including NAP, PHE, PYR and BaPYR, were used in this experiment. These compounds differ greatly in molecular weight, volatility, water solubility and other physicochemical properties (Table A1). A methanolic mixture solution containing 20 µg mL^{-1} of each of the four compounds was prepared from individual standards (Sigma Aldrich).

Sea ice formation in the microcosms began on February 24. Two days later (designated as day 0), after the ice in each of the microcosms had grown to a thickness of ~8 cm, a 5-mm diameter hole was made with a hand drill through the center of the ice surface in each microcosm except the control. Subsequently, 25 mL of the PAH mixture solution was injected ~20 cm beneath the ice-water interface using a plastic disposable pipette. This was followed by an injection of 20 mL of ambient seawater at the same depth and turning the submerged pipette tip in the underlying seawater several times to aid the dispersal of the added PAHs. The opening in the ice was resealed with ice shavings generated during the drilling. The control microcosm was not spiked with PAHs. The ice continued to grow until March 16, when the experiment was terminated. A schematic showing the experimental setup and the steps followed during the sample collection is provided in Figure A1.

During the experiment, the air temperature and wind speed were measured in situ at approximately 1.5 m above the ground using a Vaisala HMP45C probe and an UltraSonic anemometer (WindSonic), respectively.

2.2.2 Sampling procedure

The five microcosms that were injected with POC and PAHs were treated identically but were sampled at different points in time as the ice grew. The first microcosm was sampled on February 28 (two days post PAH injection; day 2) when the ice had grown to a thickness of 12 ± 1 cm. The other four microcosms were sampled 5-, 9-, 14- and 19-days post PAH injection, corresponding to March 2, 6, 11, and 16, respectively. The control microcosm was sampled only on March 16.

During each sampling event, four bulk ice cores were retrieved from the corresponding microcosm using a 9-cm diameter core barrel (Kovacs Enterprise Mark II coring system). Three ice cores were dedicated for the analysis of PAHs, and the fourth was used to determine the content of particles (e.g., POC) in the ice.

The four ice cores from each sampling event were measured for the temperature profile at a resolution of every 2 cm immediately after the ice core extraction. This was done by drilling a 5-mm diameter hole perpendicular to the core length at each depth and measuring the temperature with a digital temperature probe (Traceable). Next, all ice cores were horizontally sectioned at a vertical resolution of 3 cm using a hand saw (DeWalt) and stored in 1 L clear glass jars with aluminum foil-lined polypropylene closed-top lids in a refrigerator at 4 °C until they completely melted. The exact volumes of melted ice slices and water samples were assessed with graduated cylinders with an accuracy of 0.5 mL.

Immediately following the ice core extractions, five replicates of water samples (1 L each) were collected from the water column through the cored opening using silicone tubing and a peristaltic pump (Cole-Parmer) and stored in 1 L amber glass bottles with PTFE-lined caps in a refrigerator at 4 °C for no longer than 24 hours. Three of the replicate samples were dedicated for the analysis of PAHs, and the other two for the measurement of particles in the water.

2.2.3 Sample processing and analysis

Dissolved and particulate fractions of PAHs were separated by vacuum filtration using pre-baked (at 450 °C for 6 h) and pre-weighed 0.7 µm glass microfiber filters (Whatman). During filtration, the jars used for sample storage, as well as filtration funnels, were rinsed with ice-cold Milli-Q water (18 MΩ cm) to avoid re-partitioning of PAHs between dissolved and particulate fractions. For the same reason, seawater and melted ice samples were not spiked with any organic-solvent-based standards until after the filtration. To assess the filtration recoveries, independent trials of the loss of PAHs during filtration were performed in the laboratory before the experiment. The mean recoveries (n = 6) for the four PAHs were 73 ± 15%, 87 ± 8%, 84 ± 11%, and 91 ± 13%, respectively (Table A2).

Following the filtration, liquid and particulate fractions were spiked with the deuterated PAH surrogate standards (NAP-D_8, PHE-D_{10}, PYR-D_{10}, BaPYR-D_{12}) in methanolic solution (Sigma-Aldrich) and in iso-octane solution (Cambridge Isotope Laboratories), respectively. Solid-phase extraction (SPE) and ultrasonification were then performed to extract the PAHs from dissolved and particulate fractions, respectively, following established procedures (Chen et al., 2015; Delgado-Saborit et al., 2010) with slight modifications, as detailed in Text A1. Following the SPE procedure, 20 mL aliquots of effluent were collected into 50 mL vortex tubes for bulk ice salinity measurements using an Orion Star A212 conductivity meter (Thermo Scientific).

Ice cores and water samples for the particle concentration measurements were filtered through pre-baked and pre-weighed 0.7 µm glass microfiber filters. The particulate humic acid mass was determined by gravimetry, after drying the GF/F in an air-heated oven at 55 °C until constant weight and equilibration at room temperature in a desiccator.

The analysis of PAHs was performed on a gas chromatograph (GC; Agilent 7890B) coupled with a triple quadrupole mass spectrometer (MS/MS; Agilent 7010B) equipped with a PAL RSI

85 autosampler, a Rxi-PAH analytical column (60 m×250 μm×0.1 μm), and helium as the carrier gas. Information regarding the details of the instrumental analysis is presented in Text A2. Quantification of PAHs was achieved with a set of external standards (Restek) containing native and deuterated NAP, PHE, PYR and BaPYR with concentrations ranging from 0.488 to 1000 ng mL^{-1}. A detailed description of the targeted ions is provided in Table A3. The QC information concerning the blanks and instrumental analysis is provided in Text A3.

2.2.4 Data analysis

The V_B of the respective sea ice samples was calculated from the sea ice temperature and bulk ice salinity based on the formula of Cox and Weeks (1983). The ice growth rate was calculated by dividing the ice thickness growth (cm) between the two consecutive measurement dates by the period the growth occurred (day).

The K_ds (L kg^{-1}) for NAP, PHE, PYR, and BaPYR in both ice and water matrices were calculated as the ratio of their concentrations in the particulate humic acid phase (ng kg^{-1}) to those in the dissolved aqueous phase (liquid phase obtained after filtration) of seawater or melted bulk ice samples (ng L^{-1}).

The dependence of the PAH K_d values on temperature and salinity was examined by fitting the experimental data to the following general equation (Millero et al., 2006):

$$ln\,K_d = a_1 + \frac{a_2}{T} + a_3 lnT + \left(a_4 + \frac{a_5}{T}\right)S + (a_6 + \frac{a_7}{T})S^2 \qquad (1)$$

where T is temperature (K), S is salinity, and a_i are fitting parameters.

Statistical analysis was carried out using SigmaPlot 14.0 (Systat Software Inc.). Student's t-test was used to establish the statistical difference by comparing total mass of each PAH in the microcosms (or individual compartments such as the water, ice and potential atmospheric losses) on day 0 vs day 19; the relative fractions (%) of each PAH associated with diss-PAH phase (or part-PAH phase) in sea ice (or seawater) on day 2 *vs* day 19; log K_d values of each PAH in the ice (or seawater) on day 2 *vs* day 19, and at a specific point in time in sea ice *vs* seawater. One-way ANOVA was used to examine the statistical difference under various conditions by contrasting the total masses of the four PAH in a certain microcosm compartments (e.g., sea ice or seawater or potential atmospheric loss) at a certain point of time; the relative fractions (%) of the four PAH associated with a specific phase (e.g., diss-PAH or part-PAH phase) in sea ice (or seawater) at a certain point in time; the four PAH log K_d values compared among each other in the ice (or seawater) at a certain point in time. The significant level was set at 0.05 for each test. Regression analyses were used to determine relationships between PAH concentrations and bulk ice salinity.

2.3 Results

2.3.1 Sea ice and seawater properties

Throughout the study, the ambient air temperature fluctuated between –19 and +6 °C, mostly well below 0 °C; the daytime high reached above 0 °C only on four days (February 24, and March 1, 7 and 11). The wind speed varied between 0.2 to 5.1 m s^{-1} with an average of 1.1 m s^{-1} (Figure A2b).

Despite the ambient air temperature variability, the ice continued to grow throughout the experiment. The ice growth rate was 4.0 cm day^{-1} between February 24 and 26 and decreased to between 0.1 and 2.3 cm day^{-1} on subsequent days (Table A8). The ice thickness ranged from approximately 8.0 ± 0.4 to 19.3 ± 3.8 cm on day 0 and day 19, respectively. There were no major snowfall events during the experiment.

The ice was relatively warm throughout, with the average temperatures at the surface and bottom of the ice reaching –2.7 ± 1.5 and –2.5 ± 0.9 °C, respectively. The temperature of sea ice on day 2 (Figure A3a) increased steadily from the ice surface to the ice-water interface. The ice temperature for the subsequent dates showed an isothermal profile throughout the ice column, as the ambient air temperature rose (Figure A2).

While the ice temperature increased over time, the average bulk ice salinity decreased from 10.1 ± 1.2 on day 2 to 6.3 ± 0.3 on day 19. The underlying seawater salinity varied between 36.2 ± 3.0 and 45.1 ± 1.4 during the study (Figure A3b). The bulk ice salinity exhibited a C-shaped profile with slightly higher salinities at the top- and bottom-most parts of the ice in relation to the middle ice sections (Figure A3b), as commonly observed in young and growing natural sea ice (Petrich and Eicken, 2017).

The maximum particulate humic acid concentration reached 7.1 ± 1.6 mg L^{-1} at the ice surface; it gradually decreased with ice depth to 1.9 ± 0.9 mg L^{-1} in the bottom ice layers (Figure A3c). The mean particulate humic acid concentration in seawater was 2.9 ± 0.1 mg L^{-1}. Mass budget calculations show a total loss of up to 8–11% of the particulate humic acid in the microcosms, likely due to a combination of factors such as sorption onto the container walls and settling to the bottom.

The V_B in sea ice increased from the surface (11–31%) toward the ice-water boundary layer (19–37%), as the ice warmed up with depth (Figure A3d). As these values well exceeded the critical ice porosity threshold of 5% (Golden et al., 1998; Golden et al., 2007) in the entire thickness, movement of fluids was expected within the ice matrix throughout the experiment.

2.3.2 Distribution of PAHs between seawater, sea ice and atmosphere

The total amounts of each PAH in the microcosms were calculated as the sum of their quantities measured in the dissolved and particulate fractions of bulk sea ice and the water column (Table A6). Percentages of the PAHs in each of the microcosm compartments and potential losses (Figure 2.1) were calculated relative to the original amounts added (day 0), which ranged from 498 μg for PYR to 511 μg for NAP (Table A6). As can be seen from Figure 2.1 and Table A6, quantities of NAP, PHE, and PYR in the microcosms gradually and significantly ($p < 0.05$) decreased with time; by the end of the study, the mean atmospheric losses observed for NAP, PHE and PYR had reached 58, 17 and 5% of their initial masses, respectively. In contrast, there was no significant loss ($p > 0.05$) of BaPYR. The lost portions of each compound were assumed to be fractions volatilized in the air and were calculated as a difference between the compound’s initial mass on day 0 and the sum of the seawater and sea ice fractions. The concentrations of PAHs in the air just above the microcosms were not measured in this study.

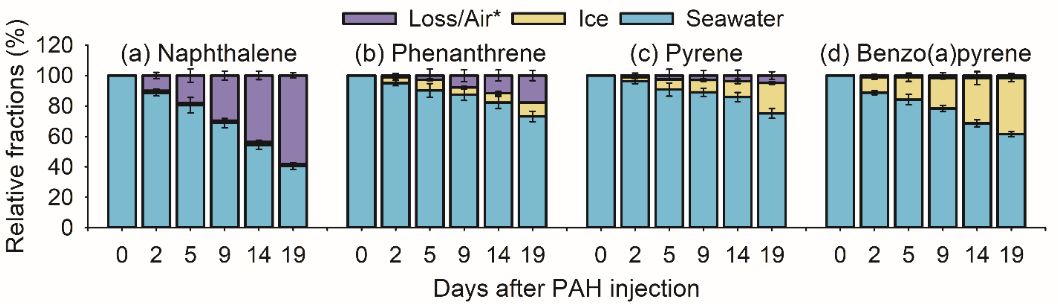

Figure 2.1. Distribution of the mean relative fractions (%) of the four PAHs between the water, sea ice and air compartments. The loss to the air was estimated from the difference between the initial mass on day 0 and the sum of the seawater and sea ice fractions on each sampling day. Error bars correspond to the respective standard deviations.

Examples of vertical distribution profiles of the four PAHs in the ice are shown in Figure 2.2; vertical profiles for all the sampling events can be found in Figure A4. Overall, the higher the molecular weight of the compound, the larger its quantity is encased in the ice. For instance, on day 2, up to 9.6, 22.1, 15.9, and 53.7 µg of NAP, PHE, PYR and BaPYR, respectively, were found in the ice, with the largest quantity of each compound found at the ice depth corresponding to the ice-water interface at the time of PAH injection (~8 cm) and below. Over time, the quantities of PHE, PYR and BaPYR in the ice significantly ($p < 0.05$) increased. No change in the content of NAP ($p > 0.05$) was observed (Figures 2.1 and 2.2). On day 19, predominant portions of NAP and PHE were present in the bottom-most ice sections (below 11 cm), whereas PYR, BaPYR were more dominant in the middle and top sections (above 11cm).

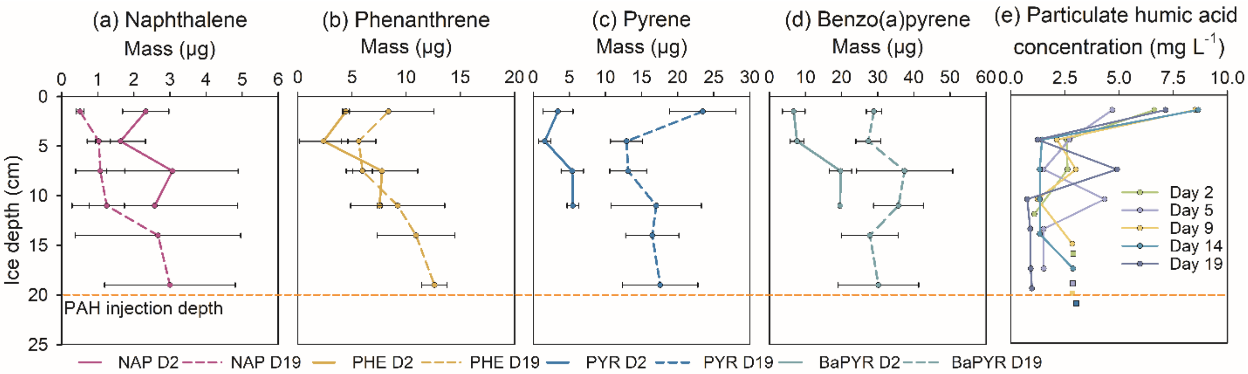

Figure 2.2. Vertical distribution profiles of (a–d) PAH mean masses in sea ice on day 2 (solid line) and day 19 (dashed line), and (e) concentrations of particulate humic acid throughout the experiment. The square symbols in (e) indicate particulate humic acid concentrations in the water column. Error bars correspond to the respective standard deviations.

2.3.3 Partitioning of PAHs between the liquid and particulate phases

Measurements of the PAH masses in the dissolved (diss-PAH) and particulate (part-PAH; i.e., PAHs bound to particulate humic acid) fractions allow for a better evaluation of their fate and exposure in the studied system (Figure 2.3). In the ice, up to 3, 4, 36, and 71% of NAP, PHE, PYR and BaPYR, respectively, were bound to humic acid on day 2. By day 19, the corresponding part-PAH fractions significantly ($p < 0.05$) increased to 4, 27, 82, and 92%.

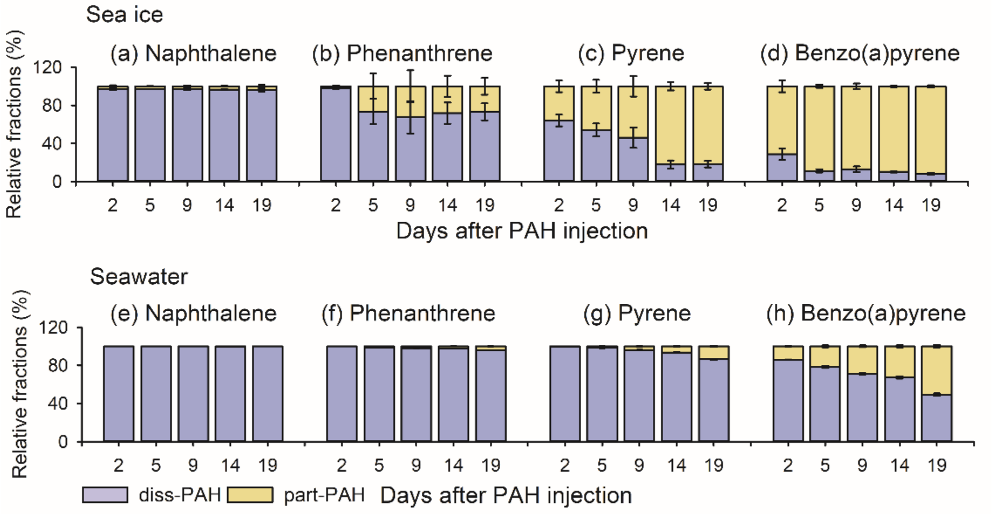

Figure 2.3. Mean relative fractions (%) of the four PAHs detected in the dissolved (diss-PAH) and particulate (part-PAH) phases in the ice (a–d) and the underlying water column (e–h). The standard deviations for the four PAHs in seawater are close to 0, and hence, the error bars are not visible.

In the underlying seawater, the four PAHs bound to particulate humic acid followed a similar pattern (Figure 2.3b), where the higher the compound's molecular weight, the larger its content in the part-PAH fraction. For example, the part-PAH fractions of the four PAHs in the water were 0, 0.1, 0.4, and 14% on day 2, and significantly ($p < 0.05$) increased to 0.1, 4, 14, and 51% on day 19, respectively.

The mean log K_d values for the studied PAHs calculated from the PAH concentrations in the dissolved and particulate fractions in sea ice on day 2 were 3.8, 3.7, 5.1, and 5.8 for NAP, PHE, PYR, and BaPYR, respectively, and by day 19, they significantly ($p < 0.05$) increased to 4.5, 5.7, 6.3, and 6.7, respectively (Table A7).

2.4 Discussion

2.4.1 Microcosm approach for studying PAH partitioning in the sea ice environment

Partitioning of PAHs in the sea ice environment can be studied at field and laboratory scales. While field studies reflect real-world situations, they are logistically challenging, and it is difficult to isolate a specific process that is being studied due to the dynamic nature of the real-world environment. On the contrary, the laboratory-based approach allows greater control over experimental conditions, which leads to more precise data, but may not be representative of real-world situations, which can limit the applicability of the findings.

In this study, we used a new microcosm approach that bridges between the field and laboratory approaches, allowing us to isolate and probe partitioning of PAHs among different phases (dissolved *vs* particulate) in different compartments (sea ice and seawater) under ambient winter conditions that resemble the Arctic. This approach is particularly useful due to a much simpler operational and less costly setup than the field-scale approach, the ability to control the composition of seawater (e.g., salinity, the type and concentration of POC, and the choice and concentration of the studied PAHs), and the ability to control the timing of PAH injection. One of the limitations of this approach, however, is a lack of mixing in the microcosms, which prevented efficient circulation of seawater and, consequently, homogenous distribution of POC and PAHs.

As shown in Figure A3, the properties of the ice from the microcosms resemble those of natural sea ice. Specifically, the observed temperature gradient from the surface to the bottom ice is characteristic of natural sea ice. The bulk ice salinity profiles of the ice grown during our study are representative of young and growing sea ice with the characteristic C-shape curve with higher salinities at both interfaces. This is due to the rejection of highly saline brine during the ice formation and growth processes that subsequently accumulates at the surface of the ice and the underlying water column (Notz and Worster, 2009; Petrich and Eicken, 2017). Due to the small volume of the microcosm, this resulted in a much higher salinity in the underlying seawater.

Mass balance calculations were conducted to assess the potential loss of PAHs in the microcosms and the potential experimental artifacts. The observation that the total amount of BaPYR, the least volatile among the studied PAHs, remained essentially unchanged ($p > 0.05$) throughout the study period (Figure 2.1 and Table A6) confirms negligible losses of the compound due to sorption to the sides of the microcosms. Moreover, control samples and field blanks contained very low levels of PAH (from not detectable to 1.5 ng L^{-1}; Table A4), confirming that atmospheric contamination of PAHs can be ruled out and the chemicals detected in the samples originated from the PAH spike solution. Biodegradation of PAHs by microbial organisms is known to occur in the natural snow and ice environment (Iriarte et al., 2023). Since SERF employs artificial seawater formulated at the beginning of the winter, the microbial activity in SERF seawater and sea ice has been shown to be very low during winter months (Gao et al., 2024; Rysgaard et al., 2014) and with negligible biodegradation potential for PAHs (Saltymakova et al., 2025).

2.4.2 Incorporation and early transport of PAHs across the seawater-sea ice-atmosphere interface

Chemicals introduced into the multiple-phased sea ice environment will partition to different phases (gaseous, dissolved, and particulate) based on their physicochemical properties. Once accommodated in a preferential compartment (ice crystals, brine or air bubbles, and organic matter), they are subsequently transported from within and out of the ice (i.e., atmosphere and/or seawater) *via* the ice internal processes (Notz and Worster, 2009; Petrich and Eicken, 2017; Wang et al., 2017) (see Text A4). For chemicals in ice-covered seawater to reach the ice surface, a pathway through a succession of connected pores (air and brine inclusions) must connect the seawater to the air-ice interface. As a result, the transport of chemicals occurs through buoyant air bubble transfer and/or concentration gradient-driven diffusion in brine channels (Crabeck et al., 2014; Kotovitch et al., 2016), brine movements (Pućko et al., 2010), as well as sorption to solid brine channel and ice interstitial surfaces (Garnett et al., 2021; Thomas et al., 2023).

Following the injection (day 0), all PAHs were present exclusively in the water column (Figure 2.1). Their presence in the ice on day 2 indicates their rapid incorporation within the growing sea ice through freeze rejection (dissolved fraction) and particle entrapment (*via* partitioning onto particulate humic acid; particulate fraction), as well as the formation of bubbles (gaseous fraction) (Wang et al., 2017).

Since the V_B exceeded 5% (Figure A3) throughout the ice, the bulk ice phase was expected to be permeable (Golden et al., 1998; Golden et al., 2007), and thus the water-air exchange of the

PAHs was possible. This is confirmed by the vertical profiles (Figure 2.2) showing that all four compounds were detected across the entire ice thickness. The differences in the quantities and vertical distribution profiles suggest that the four PAHs were subjected to different transport processes, which stems from their varying physicochemical properties.

Specifically, because of its relatively high vapour pressure and water-solubility (Table A1), NAP would have preferentially partitioned to air inclusions in the ice or dissolved in the brine. Subsequently, it migrated to the air-ice interface *via* buoyant air bubble transfer and/or concentration gradient-driven diffusion in brine channels, similar to the transport of other gases in sea ice (Crabeck et al., 2014; Kotovitch et al., 2016). NAP could also be expelled from the growing ice to the air-ice interface due to freeze rejection (Liyana-Arachchi et al., 2012). Vertical transport of NAP to the air-ice interface and its subsequent release to the atmosphere could explain the considerable loss of NAP (Desmond et al., 2019; Saltymakova et al., 2020) that occurred early in the experiment (Figure 2.1) due to its high vapour pressure.

The lower evaporative losses observed for the remaining PAHs (Figure 2.1) can be attributed to their relatively lower vapour pressures (Table A1). Therefore, bubble dynamics would be less important for their movement through the ice. Instead, their vertical transport would be partially controlled by brine migration depending on their solubility in the brine (Desmond et al., 2022; Loose et al., 2011; Pućko et al., 2010; Saltymakova et al., 2020), and partially by partitioning to the particulate humic acid depending on their affinity to particulate matter.

Brine convection, usually responsible for the transport of solutes in brine channels, appeared to regulate the distribution of the four PAHs to a limited extent only. Specifically, the mass distribution profiles of the four PAHs exhibit different patterns than the C-shaped profile expected for salinity and major sea salts (Figure 2.2); the concentrations of the four PAHs exhibited poor relationships with bulk ice salinity (Figure A5), expressed by coefficient of determination (R^2) ranging from 0.13 to 0.42. These results suggest that the behaviour of PAHs in the experimental ice deviates from that of major sea salts.

Given that particulate matter in sea ice is much less mobile (Gustafsson et al., 2005; Nürnberg et al., 1994), the particle-associated PAHs are not expected to be readily displaced out of the ice. Sorption onto the particulate humic acid is attributed to hydrophobic properties of a chemical, often expressed as the Kow (Schwarzenbach et al., 2016) (Table A1) that increases with increasing molecular weight of the PAHs. This is supported by the molecular-size-dependent distribution patterns in their K_d values (Table A7). We observe that the higher the molecular weight of the compound, the larger its portion in the ice (Figure 2.1) and the particulate humic acid fraction (Figure 2.3). This causes higher retention of HMW PAHs in the ice relative to LMW PAHs (Figure 2.1) and potentially their delayed release from melting ice, just like reported previously for snow (Meyer et al., 2009).

2.4.3 Effect of temperature and salinity on partitioning of PAHs between the liquid and particulate phases

Partitioning of PAHs between POC and water is dependent on both temperature and salinity. At above the water-freezing temperature, K_d values of PAHs are commonly affected by the combination of these two in a way that K_d increases with decreasing temperature and increasing salinity of the aqueous phase (Schwarzenbach et al., 2016). Reitsma et al. (2013) appears to be the only study that has examined the temperature and salinity dependence of PAH partitioning under water-freezing conditions. They reported that LMW PAHs attained thermodynamic equilibrium in a passive sampler-water system and showed that the respective K_d values increased as the temperature decreased from +20 to −15 °C and salinity increased from 0 to 245, which agrees with the patterns at above water-freezing temperatures. In contrast, K_d values of the HMW PAHs tended to decrease at temperatures colder than −4 °C and salinity higher than 100, which resulted from the HMW PAHs being unable to equilibrate in saline brines below 0 °C. Extremely slow equilibration of the HMW PAHs results from increased water viscosity at colder and more saline conditions (Reitsma et al., 2013).

Our study provides a unique opportunity to examine whether such a temperature and salinity dependence of K_d applies to seawater or sea ice at or below water-freezing temperatures; the results are shown in Figure 2.4 and Table 2.1. For PAHs partitioning between particulate humic acid and seawater, the four PAHs showed a moderate-to-strong relationship with temperature and salinity ($R^2 \geq 0.54$) over a very narrow freezing-temperature range of 270.4 to 271.6 K and the salinity range of 33.1 to 46.4 (Figure 2.4a−d). In bulk sea ice, K_d values for the two moderate-molecular-weight (MMW) PAHs, PHE and PYR, that are moderately water-soluble, are also reasonably well explained by the temperature and salinity dependence ($R^2 \geq 0.57$) over a temperature range of 268.2 to 272.5 K and a bulk ice salinity range of 4.2 to 12.8 (Figure 2.4f–g). However, the fitting for the lowest-molecular-weight PAH, NAP, was the poorest ($R^2 = 0.10$; Figure 2.4e) due to its very high volatility and thus large evaporative loss from the bulk sea ice (Figure 2.1a). The fitting for the highest-molecular-weight PAH, BaPYR, was also poor ($R^2 = 0.30$; Figure 2.4h), likely due to its very low water solubility and high hydrophobicity and propensity to solid ice surfaces.

Unlike in sea ice, the distribution of the four PAHs in seawater is not impacted as much by their partitioning to a gaseous phase (e.g., air inclusions) or sorption to solid surfaces different than particulate humic acid (e.g., ice crystal surfaces) that occur simultaneously with the POC-water partitioning process. This is due to the lower complexity and greater homogeneity of the seawater environment. We believe this is the reason why the K_d values in seawater exhibit stronger relationships with temperature and salinity than those in sea ice.

Overall, the dependence of K_d values on temperature and salinity in seawater and sea ice is more complex than that at above water-freezing temperatures. Different from the well-observed unidirectional influence of temperature or salinity on K_d values at above-freezing temperatures (Schwarzenbach et al., 2016), decreasing sea ice or seawater temperature and increasing salinity could result in enhancing or diminishing K_d values, depending on specific temperature-salinity conditions. This is evident in the surface plots that have more than one slope and multiple distinctive peaks (Figure 2.4).

One reason for the deviation from the expected temperature and salinity-dependence of K_d in sea ice could be due to the fact that a thermodynamic equilibrium between PAHs in particulate humic acid and in bulk sea ice could not be truly established in an extremely dynamic sea ice environment where the volume and boundaries of ice, brine, and air bubbles are always changing due to diurnal and seasonal changes of ambient air temperature (Figure A2), as suggested by Garnett et al. (2021). Similarly, the dynamically changing salinity of the underlying seawater due to the ongoing brine drainage could hinder the equilibration of PAHs in seawater, despite small temperature changes. Moreover, thermodynamic equilibrium could have been further delayed by enhanced viscosity of the ice fluids and seawater under colder and saltier conditions, which, in turn, impeded diffusion of the PAHs, similar to that reported for the passive sampler-water systems (Reitsma et al., 2013). Another study shows that even after 12 weeks, HMW PAHs were not able to reach equilibrium in a passive sampler-water system at near-freezing temperature and salinity of seawater (Jonker et al., 2015).

These results stress the challenges of determining the POC-water equilibrium K_d of PAHs under dynamically changing cold temperatures, high salinity, and ambient conditions. Hence, thermodynamic equilibrium-based parameters, such as K_d, may be of limited use when describing or modeling PAH behaviour in the dynamic sea ice environment or seawater at below-water-freezing temperatures, where common theoretical principles established for temperatures above 0 °C may not apply.

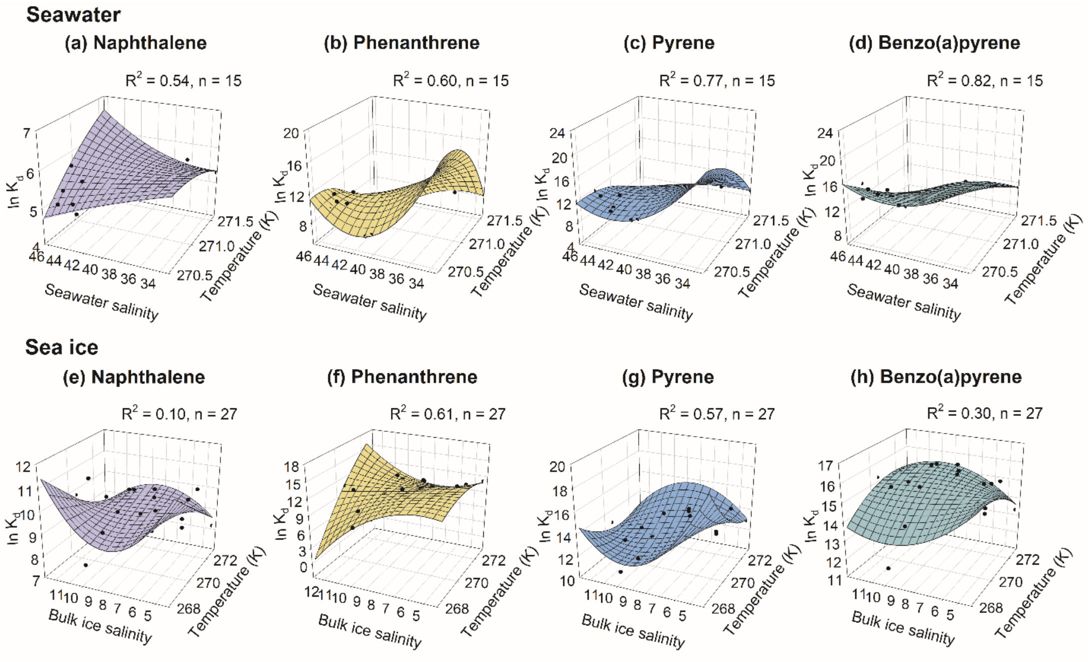

Figure 2.4. Best-fit plots of the dependence of PAH partition coefficients (K_d) on temperature and salinity in seawater (top panels) and sea ice (bottom panels).

Table 2.1. Dependence on temperature (T) and salinity (S) of the partition coefficient (K_d) of PAHs between particulate humic acid and seawater or sea ice, as fitted with the following equation:

$$ln\ K_d = a_1 + \frac{a_2}{T} + a_3 lnT + \left(a_4 + \frac{a_5}{T}\right)S + (a_6 + \frac{a_7}{T})S^2 \qquad (2)$$

Matrix	PAH	a_1	a_2	a_3	a_4	a_5	a_6	a_7
Seawater (Temperature: 270.4–271.6K, Salinity: 33.1–46.4)	NAP	5.967×10^5	-2.493×10^7	-9.008×10^4	-1.403×10^2	3.797×10^4	2.358	-6.383×10^2
	PHE	1.035×10^7	-4.054×10^8	-1.580×10^6	4.228×10^3	-1.147×10^6	-5.331×10^1	1.446×10^4
	PYR	5.832×10^6	-2.254×10^8	-8.925×10^5	2.919×10^3	-7.921×10^5	-3.552×10^1	9.638×10^3
	BaPYR	-3.618×10^3	1.042×10^7	-6.210×10^3	2.235×10^3	-6.060×10^5	-2.859×10^1	7.752×10^3
Sea ice (Temperature: 268.2–272.5, Salinity: 4.2–12.8)	PHE	3.006×10^4	-1.251×10^7	-4.541×10^4	-3.260×10^2	8.803×10^4	2.602×10^1	-7.037×10^3
	PYR	-2.422×10^5	1.035×10^7	3.642×10^4	4.704×10^2	-1.274×10^5	-2.614×10^1	7.077×10^3

2.4.4 Evolution of the PAH behaviour across the seawater-sea ice-atmosphere interface

Based on the above results, a general evolution scheme of PAHs across the seawater-sea ice-atmosphere interface is depicted in Figure 2.5. As the ambient air temperature increases with time (Figure A2), the ice warms up and becomes more porous (Figure A3) due to expanding brine and air inclusions (Golden et al., 2007). As a result, the evaporative loss of the LMW PAHs increases ($p < 0.05$) with time, while brine-associated PAHs are more efficiently flushed to the underlying seawater with circulating brine.

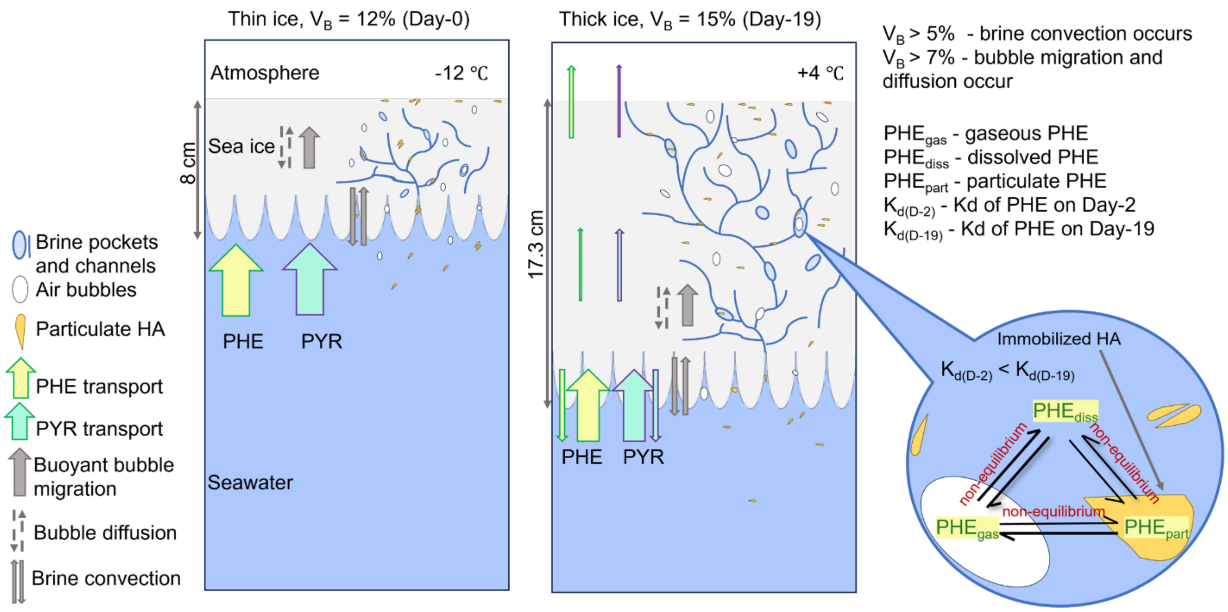

Figure 2.5. Schematic summary of the physical and chemical processes driving the distribution of PAHs in the microcosms using phenanthrene (PHE) and pyrene (PYR) as examples. V_B: brine volume fraction; HA: humic acid; K_d: partition coefficient between the particulate and dissolved phases.

PAHs present in the ice are not limited to brine channels but rather are distributed throughout the bulk ice through chemical-specific processes, such as partitioning to the dissolved phase (e.g., ice brine) (Pućko et al., 2010), partitioning to solid phases (e.g., ice interstitial surfaces or particulate humic acid) (Duprat et al., 2019; Duprat et al., 2021; Garnett et al., 2021; Lannuzel et al., 2011), or partitioning toward the gaseous phase (e.g., air bubbles). As the ice grows, its volume, phase content, and properties (e.g., temperature and salinity) change rapidly and dynamically.

Therefore, PAHs that partition between these phases are unlikely to reach true thermodynamic equilibrium. With time, the ice becomes warmer and less saline, which promotes an overall increase ($p < 0.05$) in partitioning of the MMW and HMW PAHs to the particulate humic acid (Figure 2.3, Table A7). While the partitioning behaviour of PAHs of intermediate water solubility, such as PHE and PYR, appears to be relatively well explained by evolving temperature and salinity of the ice, PAHs of more extreme properties, such as NAP and BaPYR, behave in a way that is poorly explained by temperature and salinity.

The enhanced partitioning of PAHs to the particulate humic acid leads to an increasing fraction of MMW and HMW PAHs in the ice and their subsequent retention. The retention of the HMW PAHs in the ice may potentially increase exposure to any ice-dwelling biota (Garnett et al., 2021; Pućko et al., 2010). This is particularly important when sediment-laden ice becomes more common in the Arctic (Eicken et al., 2005) and seasonal ice becomes enriched with organic matter from algal blooms, both of which have the potential to scavenge and interact with organic contaminants (Krembs et al., 2011; Wang et al., 2017). Furthermore, while particulate humic acid was used as a surrogate for POC in this study, it should be noted that the presence of other particulate matter, for instance, soot, may further enhance the retention of PAHs in sea ice. This is because of much higher affinities of PAHs to soot (Bucheli and Gustafsson, 2000; Jonker and Koelmans, 2002). As shipping activities, and tundra and forest fires could readily deposit soot onto snow and sea ice, the interactions of soot with PAHs, as well as with other contaminants in the sea ice environment, need to be considered in future studies.

Acknowledgements

We thank the Natural Sciences and Engineering Research Council (NSERC) of Canada, the Canada Research Chairs (CRC) Program, Genome Canada, and Genome Prairie for funding. This work is also a contribution to the GENICE II project. Our special thanks go to David Binne at the Sea-ice Environmental Research Facility who helped tremendously with the microcosm setup, and to Dr. Cathrin Veenaas for help and support in sample collection and processing.

Supporting Information

The Supporting Information for this chapter is available in Appendix A.

References

AMAP. 2017. Assessment 2016: Chemicals of Emerging Arctic Concern. Arctic Monitoring and Assessment Programme (AMAP): Oslo, Norway. i–353.

AMAP. 2021. Arctic Climate Change Update 2021: Key Trends and Impacts. Arctic Monitoring and Assessment Programme (AMAP): Tromsø, Norway. i–145.

Brunk, B. K., Jirka, G. H., & Lion, L. W. 1997. Effects of Salinity Changes and the Formation of Dissolved Organic Matter Coatings on the Sorption of Phenanthrene: Implications for Pollutant Trapping in Estuaries. Environmental Science and Technology, 31: 119–125.

Bucheli, T. D., & Gustafsson, Ö. 2000. Quantification of the Soot-Water Distribution Coefficient of PAHs Provides Mechanistic Basis for Enhanced Sorption Observations. Environmental Science and Technology, 34: 5144–5151.

Carls, M. G., Rice, S. D., & Hose, J. E. 1999. Sensitivity of fish embryos to weathered crude oil: Part I. Low-level exposure during incubation causes malformations, genetic damage, and mortality in larval Pacific herring (Clupea pallasi). Environmental Toxicology and Chemistry, 18: 481–493.

Chen, Y., Jia, R., & Yang, S. 2015. Distribution and source of polycyclic aromatic hydrocarbons (PAHs) in water dissolved phase, suspended particulate matter and sediment from Weihe River in Northwest China. International Journal of Environmental Research and Public Health, 12: 14148–14163.

Cox, G. F. N., & Weeks, W. F. 1983. Equations for Determining the Gas and Brine Volumes in Sea-Ice Samples. Journal of Glaciology, 29: 306–316.

Crabeck, O., Delille, B., Rysgaard, S., Thomas, D. N., Geilfus, N. X., Else, B., & Tison, J. L. 2014. First "in situ" determination of gas transport coefficients (D_{O2}, D_{Ar}, and D_{N2}) from bulk gas concentration measurements (O_2, N_2, Ar) in natural sea ice. Journal of Geophysical Research: Oceans, 119: 6655–6668.

Dawson, J., Pizzolato, L., Howell, S. E. L., Copland, L., & Johnston, M. E. 2018. Temporal and Spatial Patterns of Ship Traffic in the Canadian Arctic from 1990 to 2015. Arctic, 71: 15–26.

Delgado-Saborit, J. M., Aquilina, N., Baker, S., Harrad, S., Meddings, C., & Harrison, R. M. 2010. Determination of atmospheric particulate-phase polycyclic aromatic hydrocarbons from low volume air samples. Analytical Methods, 2: 231–242.

Desmond, D. S., Saltymakova, D., Crabeck, O., Schreckenbach, G., Xidos, J. D., Barber, D. G., Isleifson, D., & Stern, G. A. 2022. Methods for Interpreting the Partitioning and Fate of Petroleum Hydrocarbons in a Sea Ice Environment. Journal Physical Chemistry A, 126: 772–786.

Desmond, D. S., Saltymakova, D., Neusitzer, T. D., Firoozy, N., Isleifson, D., Barber, D. G., & Stern, G. A. 2019. Oil behavior in sea ice: Changes in chemical composition and resultant effect on sea ice dielectrics. Marine Pollution Bulletin, 142: 216–233.

Duprat, L., Kanna, N., Janssens, J., Roukaerts, A., Deman, F., Townsend, A. T., Meiners, K. M., Van Der Merwe, P., & Lannuzel, D. 2019. Enhanced Iron Flux to Antarctic Sea Ice via Dust Deposition From Ice-Free Coastal Areas. Journal of Geophysical Research: Oceans, 124: 8538–8557.

Duprat, L., Townsend, A. T., van der Merwe, P., Meiners, K. M., & Lannuzel, D. 2021. Spatial and seasonal distribution of dissolved and particulate bioactive metals in Antarctic sea ice. Elementa, 9: 1–24.

Eicken, H., Gradinger, R., Gaylord, A., Mahoney, A., Rigor, I., & Melling, H. 2005. Sediment transport by sea ice in the Chukchi and Beaufort Seas: Increasing importance due to changing ice conditions? Deep Sea Research Part II: Topical Studies in Oceanography, 52: 3281–3302.

Finizio, A., & Di Guardo, A. 2001. Estimating temperature dependence of solubility and octanol–water partition coefficient for organic compounds using RP-HPLC. Chemosphere, 45: 1063–1070.

Gao, Z., Munson, K., & Wang, F. 2024. Temporal Evolution of Gaseous Mercury Across the Sea Ice-Seawater Interface: A Mesocosm Study. Journal of Geophysical Research: Oceans, 129: 1–13.

Garnett, J., Halsall, C., Thomas, M., Crabeck, O., France, J., Joerss, H., Ebinghaus, R., Kaiser, J., Leeson, A., & Wynn, P. M. 2021. Investigating the Uptake and Fate of Poly- and Perfluoroalkylated Substances (PFAS) in Sea Ice Using an Experimental Sea Ice Chamber. Environ Science and Technology, 55: 9601–9608.

Golden, K. M., Ackley, S. F., & Lytle, V. I. 1998. The Percolation Phase Transition in Sea Ice. Science, 282: 2238–2241.

Golden, K. M., Eicken, H., Heaton, A. L., Miner, J., Pringle, D. J., & Zhu, J. 2007. Thermal evolution of permeability and microstructure in sea ice. Geophysical Research Letters, 34: 1–6.

Gustafsson, Ö., Andersson, P., Axelman, J., Bucheli, T. D., Kömp, P., McLachlan, M. S., Sobek, A., & Thörngren, J. O. 2005. Observations of the PCB distribution within and in-between ice, snow, ice-rafted debris, ice-interstitial water, and seawater in the Barents Sea marginal ice zone and the North Pole area. Science of The Total Environment, 342: 261–279.

Hannam, M. L., Bamber, S. D., John Moody, A., Galloway, T. S., & Jones, M. B. 2010. Immunotoxicity and oxidative stress in the Arctic scallop Chlamys islandica: Effects of acute oil exposure. Ecotoxicology and Environmental Safety, 73: 1440–1448.

Hatlen, K., Camus, L., Berge, J., Olsen, G. H., & Baussant, T. 2009. Biological effects of water soluble fraction of crude oil on the Arctic sea ice amphipod Gammarus wilkitzkii. Chemistry and Ecology, 25: 151–162.

Iriarte, J., Dachs, J., Casas, G., Martínez-Varela, A., Berrojalbiz, N., & Vila-Costa, M. 2023. Snow-Dependent Biogeochemical Cycling of Polycyclic Aromatic Hydrocarbons at Coastal Antarctica. Environmental Science and Technology, 57: 1625–1636.

Jonker, M. T. O., & Koelmans, A. A. 2002. Sorption of Polycyclic Aromatic Hydrocarbons and Polychlorinated Biphenyls to Soot and Soot-like Materials in the Aqueous Environment: Mechanistic Considerations. Environmental Science and Technology, 36: 3725–3734.

Jonker, M. T. O., Van Der Heijden, S. A., Kotte, M., & Smedes, F. 2015. Quantifying the Effects of Temperature and Salinity on Partitioning of Hydrophobic Organic Chemicals to Silicone Rubber Passive Samplers. Environmental Science and Technology, 49: 6791–6799.

Kotovitch, M., Moreau, S., Zhou, J., Vancoppenolle, M., Dieckmann, G. S., Evers, K.-U., Van der Linden, F., Thomas, D. N., Tison, J.-L., & Delille, B. 2016. Air-ice carbon pathways inferred from a sea ice tank experiment. Elementa (Washington, D.C.), 4: 1–15.

Krembs, C., Eicken, H., & Deming, J. W. 2011. Exopolymer alteration of physical properties of sea ice and implications for ice habitability and biogeochemistry in a warmer Arctic. Proceedings of the National Academy of Sciences, 108: 3653–3658.

Lannuzel, D., Bowie, A. R., van der Merwe, P. C., Townsend, A. T., & Schoemann, V. 2011. Distribution of dissolved and particulate metals in Antarctic sea ice. Marine Chemistry, 124: 134–146.

Liyana-Arachchi, T. P., Valsaraj, K. T., & Hung, F. R. 2012. Ice Growth from Supercooled Aqueous Solutions of Benzene, Naphthalene, and Phenanthrene. The Journal of Physical Chemistry A, 116: 8539–8546.

Loose, B., Schlosser, P., Perovich, D., Ringelberg, D., Ho, D. T., Takahashi, T., Richter-Menge, J., Reynolds, C. M., McGillis, W. R., & Tison, J. L. 2011. Gas diffusion through columnar laboratory sea ice: implications for mixed-layer ventilation of CO_2 in the seasonal ice zone. Tellus B: Chemical and Physical Meteorology, 63: 23.

Macdonald, R. W., Barrie, L. A., Bidleman, T. F., Diamond, M. L., Gregor, D. J., Semkin, R. G., Strachan, W. M. J., Li, Y. F., Wania, F., Alaee, M., Alexeeva, L. B., Backus, S. M., Bailey, R., Bewers, J. M., Gobeil, C., Halsall, C. J., Harner, T., Hoff, J. T., Jantunen, L. M. M., Yunker, M. B. 2000. Contaminants in the Canadian Arctic: 5 years of progress in understanding sources, occurrence and pathways. Science of The Total Environment, 254: 93–234.

Means, J. C., Wood, S. G., Hassett, J. J., & Banwart, W. L. 1980. Sorption of polynuclear aromatic hydrocarbons by sediments and soils. Environmental Science and Technology, 14: 1524–1528.

Meyer, T., Lei, Y. D., Muradi, I., & Wania, F. 2009. Organic Contaminant Release from Melting Snow. 1. Influence of Chemical Partitioning. Environmental Science and Technology, 43: 657–662.

Meyer, T., Lei, Y. D., & Wania, F. 2006. Measuring the Release of Organic Contaminants from Melting Snow under Controlled Conditions. Environmental Science and Technology, 40: 3320–3326.

Millero, F. J., Graham, T. B., Huang, F., Bustos-Serrano, H., & Pierrot, D. 2006. Dissociation constants of carbonic acid in seawater as a function of salinity and temperature. Marine Chemistry, 100: 80–94.

Notz, D., & Worster, M. G. 2009. Desalination processes of sea ice revisited. Journal of Geophysical Research, 114: 1–10.

Nürnberg, D., Wollenburg, I., Dethleff, D., Eicken, H., Kassens, H., Letzig, T., Reimnitz, E., & Thiede, J. 1994. Sediments in Arctic sea ice: Implications for entrainment, transport and release. Marine Geology, 119: 185–214.

Petrich, C., & Eicken, H. 2017. Overview of sea ice growth and properties. In Sea Ice, 1–41.

Pućko, M., Stern, G. A., Macdonald, R. W., & Barber, D. G. 2010. α- and γ-hexachlorocyclohexane measurements in the brine fraction of sea ice in the Canadian High Arctic using a sump-hole technique. Environmental Science and Technology, 44: 9258–9264.

Reitsma, P. J., Adelman, D., & Lohmann, R. 2013. Challenges of Using Polyethylene Passive Samplers to Determine Dissolved Concentrations of Parent and Alkylated PAHs under Cold and Saline Conditions. Environmental Science and Technology, 47: 10429–10437.

Rysgaard, S., Wang, F., Galley, R. J., Grimm, R., Notz, D., Lemes, M., Geilfus, N. X., Chaulk, A., Hare, A. A., Crabeck, O., Else, B. G. T., Campbell, K., Sørensen, L. L., Sievers, J., & Papakyriakou, T. 2014. Temporal dynamics of ikaite in experimental sea ice. The Cryosphere, 8: 1469–1478.

Saltymakova, D., Desmond, D. S., Isleifson, D., Firoozy, N., Neusitzer, T. D., Xu, Z., Lemes, M., Barber, D. G., & Stern, G. A. 2020. Effect of dissolution, evaporation, and photooxidation on crude oil chemical composition, dielectric properties and its radar signature in the Arctic environment. Marine Pollution Bulletin, 151: 110629.

Saltymakova, D., Desmond, D. S., Smith, A. F., Bautista, M. A., Collins, E., Polcwiartek, K., Snyder, N., Wolfe, T., Hubert, C., Isleifson, D., & Stern, G. 2025. Enhanced crude oil degradation observed in sea ice following bioaugmentation with arctic bacteria. Marine Environmental Research, 204: 106942.

Schwarzenback, R. P., Gschwend, P. M., & Imboden, D. M. 2016. Environmental Organic Chemistry, 3rd Edition Wiley, 349–514.

Thomas, M., Cate, B., Garnett, J., Smith, I. J., Vancoppenolle, M., & Halsall, C. 2023. The effect of partial dissolution on sea-ice chemical transport: a combined model–observational study using poly- and perfluoroalkylated substances (PFASs). The Cryosphere, 17: 3193–3201.

Tremblay, L., Kohl, S. D., Rice, J. A., & Gagné, J.-P. 2005. Effects of temperature, salinity, and dissolved humic substances on the sorption of polycyclic aromatic hydrocarbons to estuarine particles. Marine Chemistry, 96: 21–34.

Wang, F., Pućko, M., & Stern, G. 2017. Transport and transformation of contaminants in sea ice. In Sea Ice, 472–491).

Zhou, J. L., Fileman, T. W., Evans, S., Donkin, P., Readman, J. W., Mantoura, R. F. C., & Rowland, S. 1999. The partition of fluoranthene and pyrene between suspended particles and dissolved phase in the Humber Estuary: a study of the controlling factors. Science of The Total Environment, 243–244: 305–321.

Chapter 3 Distribution of Diesel and Aromatic Hydrocarbons in Diesel-in-Ice Spill Scenario: A Microcosm Study

Building on Chapter 2, this chapter investigates the dynamics and distribution behaviour of a complex mixture of diesel and its AHs in a diesel-in-ice spill scenario using a microcosm approach over a 15-day ice growth period. This chapter reports empirical equations for predicting the distribution of 46 AHs in the water, ice and air compartments from their respective K_{OW} and K_H values. The data on the spilled diesel fuel dynamics and its AHs in icy waters are required for toxicity assessment and regional spill weathering models, yet these datasets are extremely limited. The chapter is currently under preparation for journal submission.

Contributions of Authors

I designed the experiment, planned the sampling strategy, and developed methods for sample processing and sample analysis under the supervision of Dr. Feiyue Wang (FW) and Dr. Gary Stern (GS). I performed the sampling collection with the assistance of group members: Kedong Zhang (KZ), Skye Kushner (SK) and Zhiyuan Gao (ZG). I processed the samples and performed the instrumental analysis. I worked with FW and GS on the data processing, visualization and interpretation, as well as manuscript preparation.

Abstract

Climate change-driven sea ice retreat in the Arctic makes this region more susceptible to accidental petroleum spills due to enhanced marine shipping. Since diesel is abundantly transported and used as a fuel in the Arctic, it is vital to better comprehend the fate and behaviour of its toxic fractions, specifically aromatic hydrocarbons, in ice-covered Arctic waters should a diesel spill occur. By performing a 15-day outdoor diesel-in-ice microcosm experiment, here we report early distribution behaviour of diesel fuel and its 46 aromatic hydrocarbons of varying characteristics within growing sea ice and across the seawater-ice-atmosphere interface. We demonstrate that the vertical migration of encapsulated diesel and its aromatic hydrocarbons across the ice occurred as early as 3 days following the diesel injection and continued throughout the experiment. We show that the 46 studied compounds exhibited distinct distribution behaviours in the microcosmic compartments. The relative fractions of the aromatic hydrocarbons in seawater, sea ice and potential atmospheric losses are moderately-to-well predicted from their octanol-water partition coefficients and Henry's Law Constants throughout the study. Our findings provide new quantitative insight into the dynamics of bulk diesel and aromatic hydrocarbons entrapped in sea ice cover, which will help improve models predicting their migration in icy waters to aid the detection and monitoring, response planning, and damage assessments of diesel spills in the Arctic.

3.1. Introduction

There is a clear scientific consensus that climate change is resulting in fast sea ice loss in the Arctic. A sea ice regime transition from a thick multi-year ice (MYI) to a thinner first-year ice (FYI) cover (Kwok and Cunningham, 2008) is making Arctic waters more accessible to marine shipping, which has increased by 37% between 2013 and 2024 (PAME, 2025). These changes, in turn, bring heightened probability of accidental oil spills on, in and under the Arctic sea ice. Light distillate fuels, such as diesel fuel, MDO, and MGO, are abundantly used in the Arctic as fuel for ships operating in the region and as cargo transported to Northern communities who rely on them as a primary source of energy. Moreover, with the HFO ban in the Arctic taking effect in July 2024 (Comer et al., 2020), a transition in the Arctic marine shipping towards the use of light fuels is expected. Yet, the fate and behaviour of light distillate fuels in sea ice-laden Arctic waters are poorly understood.

In general, following an under-ice oil spill, the released oil will form small droplets (< 1 cm in diameter), which will rise to the surface, and upon contact with the ice bottom will form oil lenses in under-ice depressions. If an oil spill occurs under actively growing sea ice, it will become completely encapsulated by the ice within hours to days (Fingas and Hollebone, 2003). If sea ice porosity permits (e.g., when the brine volume fraction exceeds the critical value of 5%), oil will tend to move to the surface of the ice (Karlsson et al., 2011; Oggier et al., 2020; Petrich et al., 2013). Otherwise, the oil will remain largely immobile within the ice in its original form (Fingas and Hollebone, 2003).

While oil is encased within sea ice, its aromatic components, which are among the most toxic constituents of petrogenic oils (Pampanin and Sydnes, 2013), may partition within the ice, and subsequently may be transported across the ice, to the air and the underlying seawater (Desmond et al., 2019; Faksness and Brandvik, 2008a, 2008b; Saltymakova et al., 2020). Fractionation and distribution of oil components is possible due to the highly heterogeneous structure of sea ice, where many environmental compartments co-exist in a restricted space (e.g., air bubbles, brine, solid ice lattice, and particulate matter) (Petrich and Eicken, 2017), and due to the highly dynamic nature of sea ice. Because of their varying physicochemical properties (e.g., V_P, S_{aq}, K_H, and K_{OW}), different AHs will preferentially partition to different ice compartments. Specifically, water-soluble AHs (e.g., naphthalene and its alkylated homologues) will dissolve in sea ice brine and subsequently will be expelled to the underlying seawater (Desmond et al., 2019; Saltymakova et al., 2020), reaching concentrations in the ice of up to 4 μg L^{-1}, which could potentially cause acute toxicity to ice-dwelling communities (Faksness and Brandvik, 2008a, 2008b). Volatile AHs (e.g., alkylbenzenes), which are expected to rapidly evaporate to the atmosphere in open water conditions, have instead been shown to partition into the water column along with the brine generated and rejected during new ice formation (Payne et al., 1991a). Ultimately, these compounds may persist in the deep ocean in dissolved and bioavailable forms for up to several months (Payne et al., 1991a). On the other hand, particle-reactive HMW PAHs are expected to attach to solid ice crystal surfaces (Garnett et al., 2019) and/or POM entrapped in the ice (Meyer et al., 2009a, 2009b; Polcwiartek et al., 2025).

While these general patterns in which aromatic constituents are distributed in an oil-in-ice spill scenario are described to some degree, there is a fundamental gap in the quantitative description of the dynamics of how bulk diesel and its aromatic components behave across the seawater-ice-atmosphere interface. This hinders our ability to develop diesel weathering models in icy Arctic waters, aiding diesel spill detection and monitoring, toxicity assessment, and spill response planning.

To address this knowledge gap, here we report the results of a 15-day outdoor microcosm experiment simulating a diesel-in-ice spill scenario involving experimental young sea ice. We examined and quantified the spatial and temporal distribution of diesel fuel and its 46 individual AHs across the seawater-ice-atmosphere interface, estimated fluxes of total aromatic hydrocarbons (TAHs) to the atmosphere and the underlying seawater throughout the study, investigated differences in the distribution patterns among the studied AHs, and developed empirical equations predicting their relative distribution fractions in sea ice, seawater, and losses to the atmosphere from their respective K_{OW} and K_H values.

3.2 Materials and Methods

3.2.1 Experimental set-up

The outdoor diesel-in-ice microcosm experiment was carried out between February 19 and March 11, 2019, at SERF. The experimental sea ice is grown here from artificial seawater exposed to ambient winter conditions as cold as –30 °C and is characterized by geophysical properties that are similar to Arctic FYI (Gao et al., 2022; Gao et al., 2024; Rysgaard et al., 2014). The artificial seawater at SERF was prepared in the fall by mixing groundwater and salts, with a salinity and major salt composition reflecting that of Arctic seawater (Crabeck et al., 2016). A detailed description of the artificial seawater formulation can be found elsewhere (Gao et al., 2022).

In this study, we utilized six 260 L funnel-shaped fibreglass containers (five experimental microcosms and a control) that were of the same design as in our earlier study (Polcwiartek et al., 2025). The microcosms were filled with artificial seawater to a volume of approximately 240 L on February 19 and exposed to ambient winter conditions so that the ice could form and grow. After five days (designated as day 0), approximately 100 mL of a truck diesel fuel (also known as

Premium Diesel or Number 1 Diesel; Consumers' Co-operative Refineries Limited) was introduced into each experimental microcosm. This was accomplished by drilling a 5-mm diameter hole with a hand drill through the center of the ~15-cm thick ice cover in the five experimental microcosms and injecting a diesel fuel mixture at ~50 cm below the air-ice interface using a plastic disposable syringe with silicone tubing attached to its tip. This injection depth allowed diesel droplets to spread throughout the water column and coalesce under a larger ice-water interface area. Approximately 20 mL of ambient seawater was subsequently injected at the same depth to remove any remaining diesel fuel from the tubing. The silicone tubing was then partially withdrawn from the water column with a section still remaining in the ice. The tubing was cut ~2 cm above the air-ice interface, and a new plastic syringe filled with ambient seawater was attached to its end above the ice. A portion of seawater was flushed through the tubing filling it with seawater so that the diesel fuel was unable to collect in it. The tubing with the attached syringe was left inserted in the ice for the duration of the experiment. This prevented diesel fuel from immediate migration to the ice surface through the opening in the ice. The control microcosm was not injected with diesel fuel. The control and the experimental microcosms were exposed to the same ambient winter conditions until March 11 when the experiment was terminated. At that time, the ice reached its maximal thickness of ~48 cm. An illustration and a photograph showing the experimental design are shown in Figure 3.1.

Throughout the experiment, wind speed was measured on-site at 1.5 m above the ground using an UltraSonic anemometer (WindSonic). SERF was equipped with a Vaisala HMP45C probe for ambient air temperature measurements; however, it was out of order at the time of the experiment. Therefore, the air temperatures for this study were retrieved from the Meteorological Station at the Winnipeg International Airport.

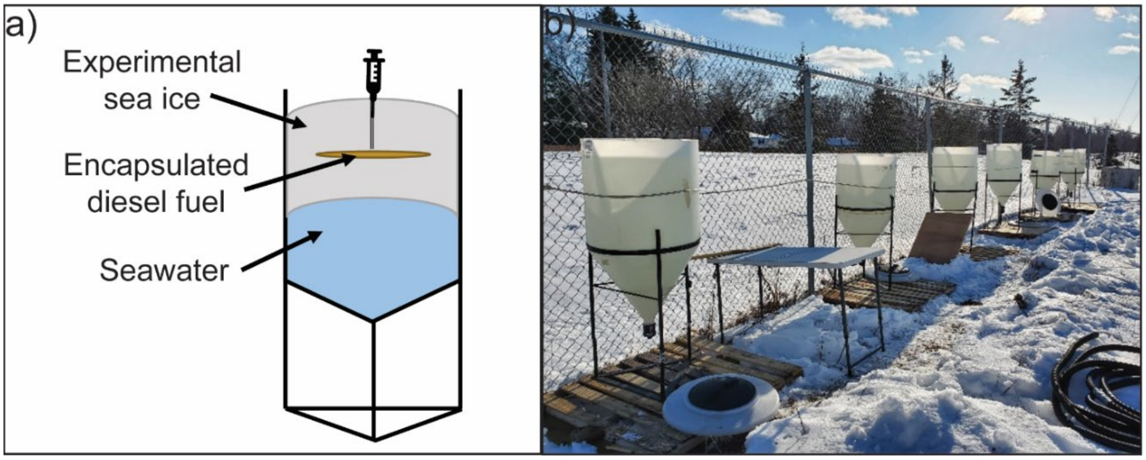

Figure 3.1. A schematic showing the experimental design (a), and a photograph of the diesel-in-ice microcosm set-up (b).

3.2.2 Sampling protocol

An illustration showing the steps followed during the sample collection is shown in Figure B1 in Appendix B. In essence, the microcosms were sampled at different points in time and independently of each other as the ice grew thicker. The first two microcosms were sampled three days following the diesel injection (February 27; days 3a and 3b), when the ice thickness reached approximately 30 cm, ensuring diesel fuel had become encapsulated within the growing ice. The sampling from the two experimental microcosms on the same day was performed to validate the replicability of the microcosm design. The remaining three experimental microcosms were sampled 5-, 8- and 15-days post diesel introduction, corresponding to March 1, 4, and 11, respectively. The diesel-free control microcosm was sampled at the end of the study on day 15.

On each sampling occasion, four ice cores were collected from a corresponding microcosm with a 9-cm diameter core barrel (Kovacs Enterprise Mark II coring system). Immediately after the ice core extraction, each ice core was measured for length and for the temperature profile. The temperature measurements were performed by drilling a 5-mm diameter hole perpendicular to the core length at a resolution of every 3 cm and recording the temperature with a digital temperature probe (Traceable). Subsequently, each ice core was horizontally sectioned with a hand saw (DeWalt) into three segments: the top section representing the uppermost 20% of the total core length (6–10 cm in length), the middle section (40% of the total ice length), and the bottom section (the remaining 40% of the ice length). The ice core sections were stored in 2 L clear glass jars with aluminum foil-lined polypropylene closed-top lids in a freezer at –20 °C until the sample processing. To prevent cross-contamination of the ice cores during each sampling event, the ice core barrel and the hand saw were thoroughly rinsed with hexane (Fisher Chemical, Optima Grade) and subsequently with methanol (Fisher Chemical, Optima Grade) between consecutive ice cores.

Following the ice core extractions, three replicate seawater samples (2.7 L each) were taken from the water column using silicone tubing and a peristaltic pump (Cole-Parmer), and were stored in 2.7 L amber glass jars with PTFE-lined caps in a refrigerator at 4 °C until sample processing.

3.2.3 Sample processing and analysis

Prior to the sample processing, the ice core samples were placed in a refrigerator at 4 °C until they completely melted. The exact volumes of melted ice core and water samples were assessed with graduated cylinders with an accuracy of 0.5 mL.

SPE and liquid-liquid extraction (LLE) were carried out to extract diesel fuel from seawater and melted ice samples, respectively. Both procedures were performed according to the protocols reported by Chen et al. (2015), and Lau and Stenstrom (1997) with adjustments, as detailed in Text B1. Before the sample processing, deuterated PAH surrogate standards (Naphthalene-D_8 (NAP-D_8), Acenaphthylene-D_8 (ACY-D_8), Acenaphthene-D_{10} (ACE-D_{10}), Fluorene-D_{10} (FLE-D_{10}), Phenanthrene-D_{10} (PHE-D_{10}), and Pyrene-D_{10} (PYR-D_{10})) in a methanolic solution (mixture prepared from individual standards; Sigma Aldrich) and in an iso-octane solution (Cambridge Isotope Laboratories) were added to the seawater and melted ice samples, respectively. The recoveries obtained for NAP-D_8, ACY-D_8, ACE-D_{10}, FLE-D_{10}, PHE-D_{10}, and PYR-D_{10} reached 48, 64, 68, 75, 79, and 101%, respectively, for the SPE procedure, and 35, 44, 49, 52, 74, and 88%, respectively, for the LLE procedure (Table B1). Since the recovery values for the respective deuterated PAHs were consistent within the population of samples, the recoveries are assessed as reliable. Low recoveries observed for NAP-D_8, ACY-D_8, and ACE-D_{10} could be attributed to their high volatility. Following the SPE and LLE procedures, 25 mL aliquots of effluent were placed into 50 mL vortex tubes and were measured for bulk salinity with an Orion Star A212 conductivity meter (Thermo Scientific).

The collected samples were analyzed for aromatic hydrocarbons using a GC (Agilent 7890B) coupled with an MS/MS (Agilent 7010B) equipped with a PAL RSI 85 autosampler, a Rxi-PAH analytical column (60 m×250 μm×0.1 μm) and helium as the carrier gas. The GC-MS/MS was operated in the selected ion monitoring (SIM) mode. The electron ionization energy was 70 eV. A sample volume of 1 μL was injected in splitless mode. The oven was operated at 40 °C with a 1 min hold, then the temperature increased to 140 °C at the rate of 30 °C/min and again to 190 °C at a rate of 10 °C/min, and finally to 320 °C at a rate of 10 °C/min with a 10 min hold.

In total, 46 AHs were identified in the diesel fuel using the following standards: mixture of 46 alkylated benzenes and PAHs (Chiron), SV Calibration Mix #5 (Restek), and Custom Alkylated PAH Standard (Restek) (Table 3.1). Quantitative analysis of the identified compounds and the deuterated surrogate compounds was accomplished using an external standard calibration approach with a single internal standard (2-fluorobiphenyl; Restek). The linear working range of the calibration curves ranged from 0.488 to 1000 μg L^{-1} and exhibited R^2 values greater than 0.98. Detailed information pertaining to the ions targeted during the analysis is provided in Table B2. Due to their very close retention times, 1-ethylnaphthalene and 2-ethylnaphthalene were quantified as a sum of two isomers (1/2-EN). The method detection limits (MDLs), calculated based on U.S.EPA (2016), ranged from 0.5 to 8.3 ng L^{-1} (Table B2).

Table 3.1. List of the 46 aromatic hydrocarbons identified in the diesel fuel and standard solutions used for their identification.

Compound	Acronym	Standard solution
1,3-diethylbenzene	1,3-DEB	Mixture of 46 alkylated benzenes and PAHs, Chiron
1,2-diethylbenzene	1,2-DEB	
1,2,4,5-tetramethylbenzene	1,2,4,5-TeMB	
1,2,3,5-tetramethylbenzene	1,2,3,5-TeMB	
Naphthalene	NAP	SV Calibration Mix #5, Restek
Acenaphthylene	ACY	
Acenaphthene	ACE	
Fluorene	FLE	
Phenanthrene	PHE	
Pyrene	PYR	
2-methylnaphthalene	2-MN	Mixture of 46 alkylated benzenes and PAHs, Chiron
1-methylnaphthalene	1-MN	
2-ethylnaphthalene	2-EN	
1-ethylnaphthalene	1-EN	
2,6-dimethylnaphthalene	2,6-DMN	
2,7-dimethylnaphthalene	2,7-DMN	
1,3-dimethylnaphthalene	1,3-DMN	
1,7-dimethylnaphthalene	1,7-DMN	
1,6-dimethylnaphthalene	1,6-DMN	
1,4-dimethylnaphthalene	1,4-DMN	
2,3-dimethylnaphthalene	2,3-DMN	
1,5-dimethylnaphthalene	1,5-DMN	
1,2-dimethylnaphthalene	1,2-DMN	
1,8-dimethylnaphthalene	1,8-DMN	
1,3,7-trimethylnaphthalene	1,3,7-TMN	
1,3,6-trimethylnaphthalene	1,3,6-TMN	
1,4,6-trimethylnaphthalene	1,4,6-TMN	
2,3,6-trimethylnaphthalene	2,3,6-TMN	
2,3,5-trimethylnaphthalene	2,3,5-TMN	
1,2,6-trimethylnaphthalene	1,2,6-TMN	
1,2,4-trimethylnaphthalene	1,2,4-TMN	
1,2,5-trimethylnaphthalene	1,2,5-TMN	
2,4,5-trimethylnaphthalene	2,4,5-TMN	
1,2,3-trimethylnaphthalene	1,2,3-TMN	
1,4,5-trimethylnaphthalene	1,4,5-TMN	
1,4,6,7-tetramethylnaphthalene	1,4,6,7-TeMN	
1,2,5,6-tetramethylnaphthalene	1,2,5,6-TeMN	
2-methylphenanthrene	2-MPHE	
2-methylanthracene	2-MANT	
1-methylanthracene	1-MANT	
1-methylphenanthrene	1-MPHE	
3-methylphenanthrene	3-MPHE	Custom Alkylated PAH Standard, Restek
9-methylphenanthrene	9-MPHE	
2-methylpyrene	2-MPYR	
4-methylpyrene	4-MPYR	
1-methylpyrene	1-MPYR	

3.2.4 Quality control

To establish background concentrations of analytes in the microcosms, seawater (1 L; n = 2) was retrieved from each experimental microcosm on February 19 before sea ice started to form. Seawater and ice cores were also collected from the control microcosm on day 15 (March 11; n = 3 each for water and ice) to determine background concentrations of aromatics in the experimental sea ice. The analytes were not detected in either the seawater of the experimental microcosms or the seawater and sea ice of the control container (Table B3).

During each sampling event, field blanks including Milli-Q water (1 L, n = 4), artificial SERF seawater (1 L; n = 4), and n-hexane (Fisher Chemical, Optima Grade; 500 mL; n = 4) were exposed to the surrounding environment for approximately 5 hours, to monitor for potential atmospheric-sourced contamination. The concentrations of the studied compounds in the field blanks varied from 0.5 to 1.4 ng L^{-1}, depending on the compound (Table B3). The concentrations of the analytes in the laboratory blanks (1 L of Milli-Q water; n = 16) collected on the sample processing days ranged from 1.4 to 3.3 ng L^{-1}. Blank samples were processed following the same SPE protocol used for seawater samples.

To meet the quality assurance criteria, the analytical instrumentation was tuned before and after each sequence of samples and standards. Moreover, quality control standard duplicates and iso-octane blanks were run every five samples to ensure that the repeatability of the instrumentation was maintained. The variability in the response of the quality control standard duplicates was within 12%.

3.2.5 Data analysis

The V_B of the respective ice samples was calculated from the ice temperature and bulk ice salinity following the formula of Cox and Weeks (1983). The ice growth rate was calculated by dividing the ice thickness (cm) between the two consecutive sampling dates and the time duration (day).

The mass of TAHs (m_{TAHs}) present in either the injected volume of diesel, the entire ice cover, or the entire volume of seawater compartment in the microcosm on a specific sampling day was calculated as the cumulative mass of all the identified aromatic hydrocarbons. The mass of each compound was calculated from its concentration in either sea ice or seawater samples and the volumes of the corresponding compartments.

The flux of the TAHs mass (F_{TAHs}; mg day^{-1} m^{-2}) that occurred between the two consecutive sampling dates was calculated using the following general equation:

$$F_{TAHs} = \frac{\Delta m_{TAHs}}{t * A} \qquad (3)$$

where Δm_{TAHs} represents the change in the total aromatic hydrocarbons mass (m_{TAHs}; mg) that occurred between the two sampling dates, t corresponds to time (day), and A is the surface area of sea ice in the respective microcosms (m^2).

Compound relative fractions (%) in the seawater ($f_{Seawater}$), bottom (f_{Bottom}), middle (f_{Middle}) and top (f_{Top}) ice core sections and the potential atmospheric losses (f_{Loss}) were calculated based on the following equation:

$$f_X = \frac{m_X}{m_0} \qquad (4)$$

where X represents a specific microcosm compartment (seawater, or bottom, middle, top ice core sections or potential loss), m_X corresponds to a mass (μg) of a compound in the respective compartment on a specific sampling day, and m_0 is the initial mass (μg) of a compound introduced into the respective microcosm on day 0.

Free and open-source modelling software, Quantitative Structure–Activity Relationship (QSAR), was used to estimate values of the following physicochemical properties of the studied aromatic hydrocarbons at 25 °C and salinity of freshwater: vapour pressure, aqueous solubility, Henry's Law Constant, octanol-water partition coefficient, and octanol-air partition coefficient. The values of are shown in Table B4.

Statistical analysis was performed using SigmaPlot 14.0 (Systat Software Inc.). Student's t-test was used to assess the statistical difference for the following comparisons: total volume of diesel (or total mass of TAHs) in the microcosm (a sum of amounts form seawater and sea ice compartments) on day 0 *vs* day 15; total volume of diesel (or total mass of TAHs) in a specific microcosm compartment (e.g., seawater, three sea ice sections or estimated atmospheric loss) on day 0 *vs* day 15; volume of diesel (or total mass of TAHs) in a specific microcosm compartment on day 3a *vs* 3b; the relative fraction (f_X; %) of each compound in a specific microcosm compartment on day 0 *vs* day 15; mass flux of TAHs to the atmosphere (or seawater) compared between two consecutive sampling dates. One-way ANOVA was carried out to examine the statistical difference under various conditions by contrasting the relative fractions (f_X; %) of selected individual AHs in a specific microcosm compartment at a certain point in time. The significant level was set at 0.05 on all occasions. Multiple linear regression analysis was performed to establish empirical equations linking the analyte's fraction values in a specific microcosm compartment with its respective K_{OW} and K_H based on the following general equation:

$$y = b_0 + b_1x_1 + b_2x_2 + \cdots + b_ix_i \quad (5)$$

where y corresponds to the analyte's relative fraction (f_X; %) value, b_0 is the intercept, b_1, b_2 and b_i are regression coefficients, and x_1, x_2, and x_i are independent variables (e.g., K_{OW}, K_H). Since experimentally derived values for the selected physicochemical properties (e.g., V_P, S_{aq}, K_{OW}, K_H, K_{OA}) are not available for most of the 46 aromatic hydrocarbons, the multiple linear regression analyses were conducted using exclusively the QSAR-predicted property values.

3.3 Results

3.3.1 Meteorological conditions, and sea ice and seawater characteristics

Throughout the experiment, the ambient air temperature ranged between –32 and –3 °C, mostly well below 0 °C (Figure B2). Sea ice began to form on day 0 and continued to grow until day 15, when the average thickness of the ice reached 47.8 ± 2.0 cm (Table B5), with a growth rate ranging between 0.5 and 5.1 cm day^{-1}.

The ice temperature increased from the air-ice interface toward the ice-water boundary layer (Figure 3.2a), as commonly observed for natural sea ice (Petrich and Eicken, 2017). For example, on day 3a, the average surface ice temperature was –8.9 ± 1.5 °C, and gradually increased to –3.3 ± 0.1 °C at the bottom of the ice. By day 15, the average surface and bottom ice temperatures increased to –5.4 ± 0.8 °C and –3.1 ± 0.5 °C, respectively. Seawater temperatures varied between

–3.1 and –2.0 °C, depending on the date. Seawater temperatures below the freezing point, –1.8 °C, could result from the small size of the microcosms and the collection of cold brine at the seawater-ice boundary layer.

Between days 0 and 15, the average bulk ice salinity varied from 4.3 ± 1.2 to 6.2 ± 1.9 in the top ice sections and from 8.4 ± 0.2 to 8.9 ± 1.2 in the bottom ice sections (Figure 3.2b). A C-shaped vertical profile of the bulk ice salinity, characteristic of young and growing natural sea ice with elevated salinities in the top and bottom ice layers (Notz and Worster, 2009), was observed only on day 15 (Figure 3.2b) and in the control microcosm (Figure B3). A reversed shape of the bulk ice salinity profile observed for the remainder of the dates can most likely be attributed to the displacement of brine from the upper ice by migrating diesel fuel. Salinity of the adjacent seawater ranged from 37.9 ± 0.1 to 48.5 ± 1.1. The elevated salinity values obtained in our study, relative to those of natural seawater (~33), can be explained by brine rejection from growing sea ice to a relatively small volume of seawater in the microcosms.

The V_B values increased downward from the ice surface (3.2–5.8%) to the bottom ice (7.9–11.3%) (Figure 3.2c). For sea ice to be porous enough so that the movement of fluids and air bubble transfer is guaranteed, a brine volume fraction of at least 5% (Golden et al., 1998; Golden et al., 2007), and an air bubble fraction of at least 7% (Crabeck et al., 2014; Loose et al., 2011), respectively, are generally required. The V_B values obtained here for diesel-contaminated ice may not reflect the actual porosity of sea ice.

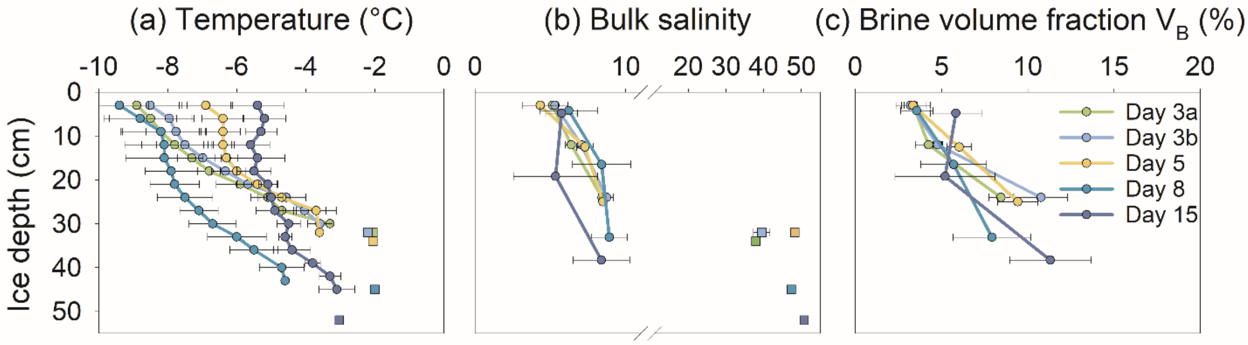

Figure 3.2. Vertical profiles of the average temperature (a), average bulk salinity (b), and average brine volume fraction (c) throughout the sea ice column (circle symbols) and in the underlying seawater (square symbols) in the microcosms on various sampling occasions. An ice depth of zero corresponds to the air-ice interface. Error bars represent the respective standard deviations.

3.3.2 Distribution of diesel fuel and aromatic hydrocarbons among seawater, sea ice and atmosphere

The total volume of diesel fuel and total mass of TAHs (m_{TAHs}) in the microcosms were calculated as the sum of diesel volumes, and the sum of the studied aromatic hydrocarbon masses, respectively, that were detected in the ice and the water column (Table B6). Relative fractions (f_X) of diesel (vol%) and TAHs (mass%) in the water column, sea ice and potential losses (Figure 3.3) were calculated relative to the respective initial amounts injected into the microcosms on day 0 (Table B6). The losses of diesel and TAHs were assumed to occur via evaporation to the atmosphere, although the concentrations of the AHs above the microcosms were not measured. Based on Figure 3.3 and Table B6, we observed that the amounts of diesel and TAHs in the microcosms decreased progressively and significantly ($p < 0.05$) over time. Specifically, by day 15, approximately 29 and 51% of the original amounts of diesel and TAHs, respectively, were lost to the air. The fractions of diesel and TAHs in the microcosmic compartments obtained for the two replicate containers sampled on day 3, displayed as days 3a and 3b, respectively, showed no significant differences ($p > 0.05$).

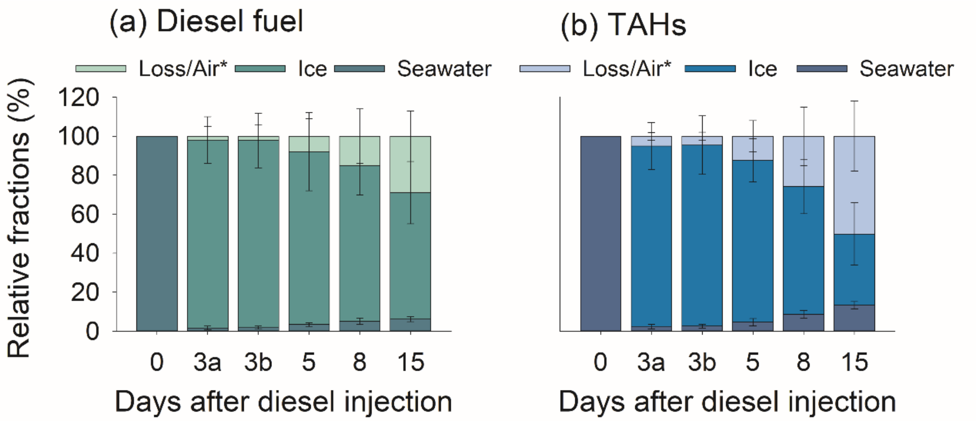

Figure 3.3. Distribution of the average relative fractions (vol.%) of diesel fuel (a) and average relative fractions (mass%) of the total aromatic hydrocarbons (TAHs) (b) among the seawater, sea ice and potential losses to the atmosphere throughout the experiment. The loss to the atmosphere was assessed from the difference between the original amounts of diesel fuel/TAHs in the microcosms on day 0 and the sum of the seawater and sea ice fractions on each sampling occasion. Error bars represent the respective standard deviations.

Vertical distribution profiles of diesel fuel and TAHs in the ice are presented in Figure 3.4; examples of vertical profiles of four representative compounds of varying physicochemical properties are provided in Figure B4. On day 3, up to 11, 82 and 4% of the initial volume of diesel were found in the top, middle and bottom ice core sections, respectively, whereas up to 17, 69 and 6% of the initial mass of TAHs were detected in the respective ice core sections. By day 15, the percentages of diesel and TAHs in the middle ice sections significantly ($p < 0.05$) decreased. The diesel and TAHs fractions in the top and bottom ice sections did not change significantly ($p > 0.05$) over time, except for the contents in the top sections on day 15 ($p < 0.05$). The percentages of diesel and TAHs across the ice sections on days 3a and 3b showed no significant differences ($p > 0.05$).

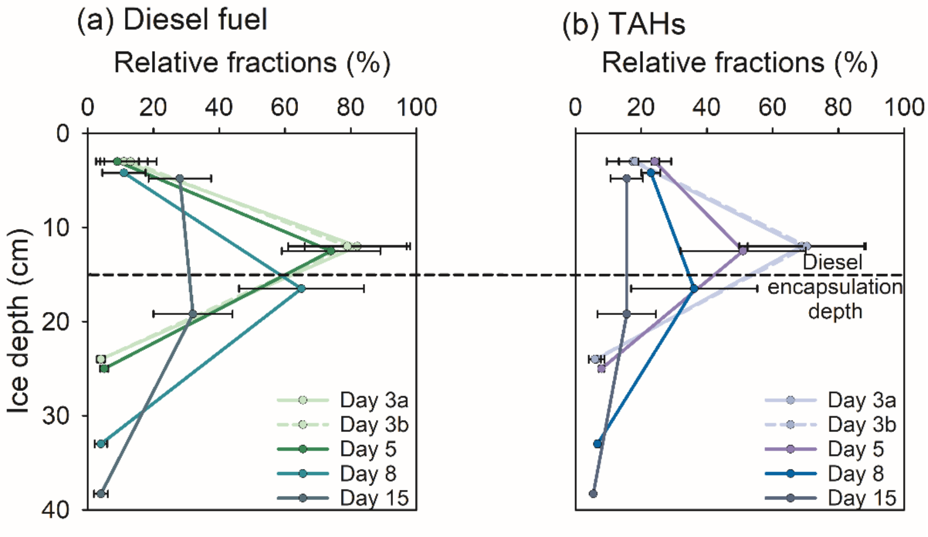

Figure 3.4. Vertical distribution of the average relative fractions (vol.%) of diesel fuel (a) and average relative fractions (mass%) of the TAHs (b) across the ice during the experiment. The relative fractions of diesel and TAHs were calculated relative to their initial amounts injected into the microcosms on day 0. Error bars represent the respective standard deviations.

Spatial and temporal variations in the vertical distribution patterns of the studied aromatic hydrocarbons are displayed in Figure 3.5. Overall, the higher the molecular weight of the compound, the larger its fraction encased in the middle ice sections and the smaller its loss. For instance, on day 3, the fraction of the compound with the lowest-molecular-weight among the studied AHs, 1,3-diethylbenzene, in the middle ice section was 59%, whereas for the highest-molecular-weight compound, that is 1-methylpyrene, the corresponding fraction reached 95%. Simultaneously, up to 10% loss was observed for 1,3-diethylbenzene, whereas no loss was recorded for 1-methylpyrene. By day 15, the fraction of 1,3-diethylbenzene in the middle ice sections and the loss significantly ($p < 0.05$) changed and reached 8 and 76%, respectively. On the contrary, the fractions for 1-methylpyrene in the corresponding compartments changed significantly ($p < 0.05$) to 60 and 8%, respectively.

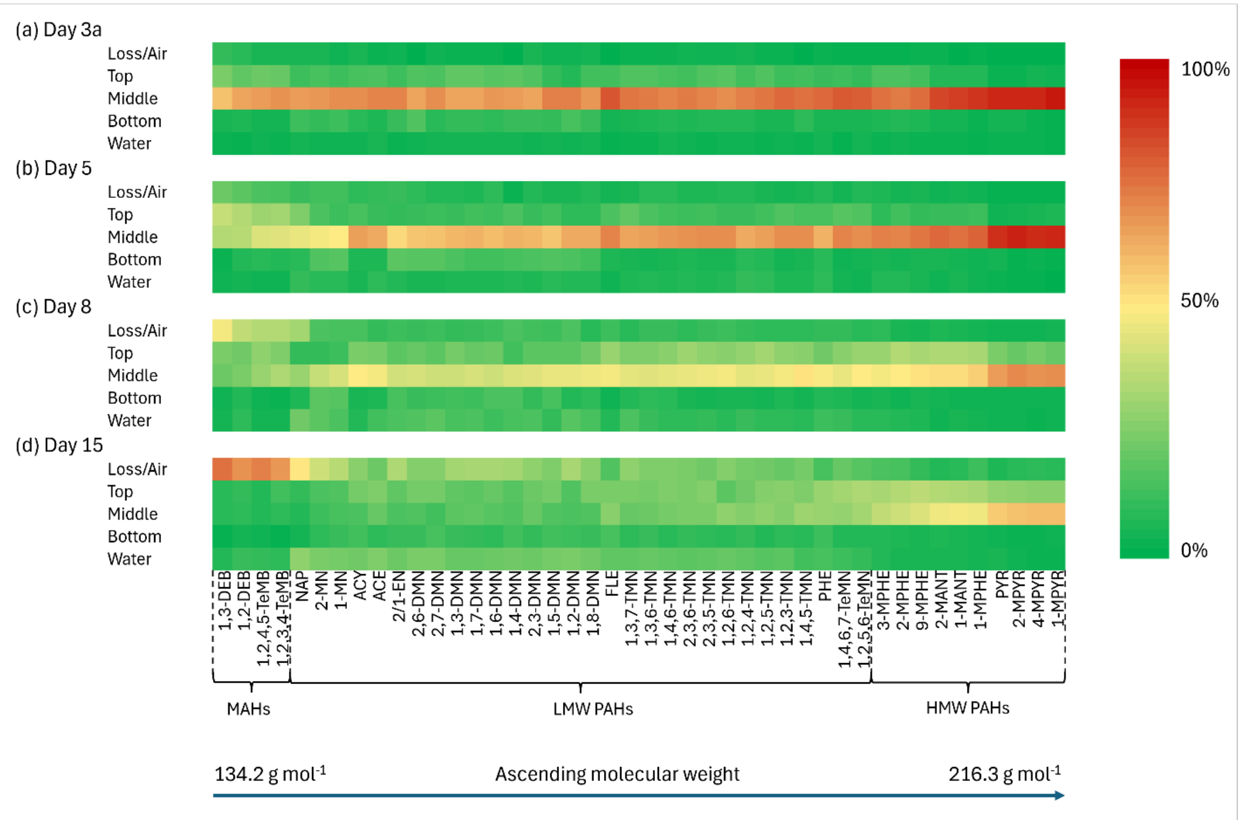

Figure 3.5. Heatmaps showing variations in the vertical distribution of the 46 aromatic hydrocarbon relative fractions (f_X; %) among the seawater, top, middle and bottom ice core sections, and potential losses to the atmosphere throughout the study. The atmospheric loss fractions were estimated from the difference between the original amount of each analyte in the diesel fuel on day 0 and its respective amount detected in the microcosms on each sampling occasion. (Yellow: f = 50%; dark green: f = 0%; dark red: f = 100%).

3.3.3 Mass flux of TAHs to the atmosphere and seawater

The masses of TAHs that were potentially lost to the atmosphere and accumulated in the water column throughout the study, along with the estimated fluxes of TAHs that occurred between the two consecutive sampling events for the corresponding compartments, are shown in Figure 3.6. Out of 963.6 mg of TAHs injected into the microcosms on day 0 (Table B6), by day 3, m_{TAHs}

lost to the air reached 47.3 mg, whereas in the seawater, the m_{TAHs} reached 23.6 mg. This gave rise to 55.8 and 27.8 mg day^{-1} m^{-2} of TAHs to the air and seawater, respectively, between days 0 and 3. The cumulative m_{TAHs} released to the air and to the water column gradually and significantly ($p < 0.05$) increased over time and reached 483.4 and 128.4 mg, respectively, by the end of the study. The fluxes of TAHs to the air and seawater continued to significantly ($p < 0.05$) rise until day 8; however, between days 8 and 15, the fluxes of TAHs significantly ($p < 0.05$) decreased.

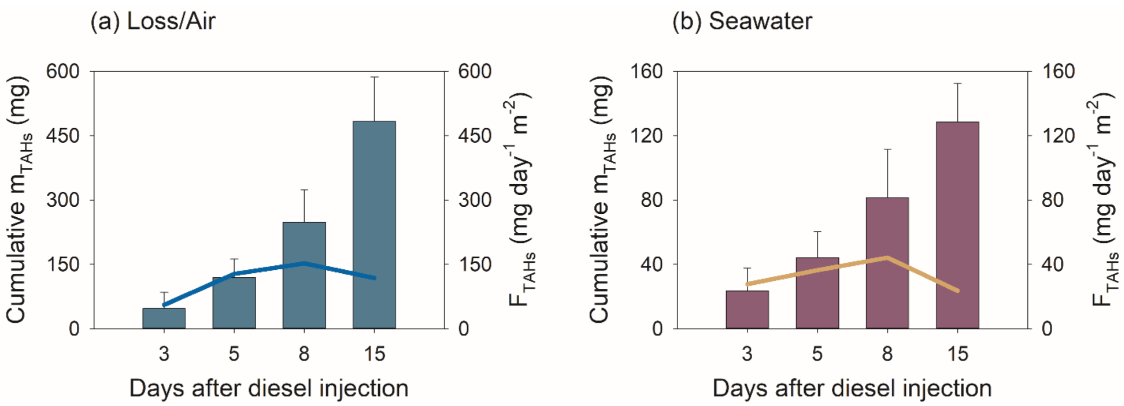

Figure 3.6. Estimated average cumulative mass of TAHs (m_{TAHs}; displayed as bars) and mass flux of TAHs (F_{TAHs}; displayed as curves) that occurred between the two consecutive sampling events to the atmosphere (a) and to the water column (b). Error bars represent the respective standard deviations.

3.4 Discussion

3.4.1 Encapsulation and early transport of diesel and aromatic hydrocarbons across the seawater-ice-atmosphere interface

The injection of diesel under the experimental sea ice (day 0) was followed by coalescence of diesel droplets in under-ice depressions approximately 15 cm below the air-ice interface. Since the ice was rapidly growing at the early stages of the experiment (Table B5), the diesel plume became surrounded by the growing ice crystals and subsequently encapsulated within the ice matrix, most likely within the first hours after the diesel injection (Fingas et al., 2015).

Despite earlier claims that movement of petroleum in sea ice during the growth season is constrained and largely ceased (Fingas and Hollebone, 2003), we observe that as early as 3 days post-diesel injection, bulk diesel and its AHs were distributed between the water column, cold sea ice, and potentially lost to the atmosphere (Figures 3.3, 3.4 and 3.6). At the time, however, the largest fractions of diesel and TAHs (Figure 3.4) and individual AHs (Figure B4) were present in the middle ice core sections corresponding to the depth of diesel encapsulation. Similarity in the vertical distribution profiles of bulk diesel (Figure 3.4a) and TAHs (Figure 3.4b) early in the experiment suggests that the migration of AHs in the microcosms was coupled with that of diesel fuel.

The presence of bulk diesel and its components in the seawater compartment can be explained by the dissolution of water-soluble AHs, such as naphthalene and its alkylated homologues (Figure 3.5) in sea ice brine, subsequent brine-driven transport from the diesel lens to the bottom ice and eventually to the adjacent water column, agreeing with a previous study (Faksness and Brandvik, 2008b). On the other hand, the presence of bulk diesel and AHs in the upper ice and potential losses (Figures 3.4 and 3.5) could be explained by the upward migration of diesel from the injection depth towards the air-ice interface through brine channels (Oggier et al., 2020). Since diesel fuel is primarily composed of volatile hydrocarbons, such as MAHs and LMW PAHs (Kuppusamy et al., 2019) (Figure B5), once released at the ice surface and exposed to the atmosphere, its volatile fractions tend to evaporate quickly, contributing to the observed loss of diesel and TAHs (Brandvik and Faksness, 2009) (Figure 3.3).

The V_B values (Figure 3.2c) early in the experiment are below the ice porosity threshold value of 5% (Golden et al., 1998; Golden et al., 2007), suggesting impermeability of our experimental ice; therefore, migration of diesel and its components was not expected to occur. However, since the V_B was calculated based on the equations that had been developed for natural, oil-free ice (Cox and Weeks, 1983), the V_B values may not be applicable in predicting ice porosity in the presence of diesel fuel.

3.4.2 Role of physicochemical properties in the distribution of aromatic hydrocarbons in diesel-in-ice microcosms

We observe varying relative fractions of AHs in the respective microcosm compartments (seawater, three sea ice depths and potential losses) (Figure 3.5), as well as differing vertical distribution profiles of several representative AHs across the ice (Figure B4). In general, the greater the molecular weight of a compound, the larger its relative fraction in the middle ice core sections containing a diesel lens, and the smaller its relative portion in the water column and potential loss (Figure 3.5). Because the identified AHs exhibit differing physicochemical properties (Table B4), they show distinct affinities to the sea ice phases (gaseous, liquid, solid surfaces, organic phase) and therefore, they are transferred between the microcosm compartments through different transport pathways; these include air bubble and brine dynamics (Polcwiartek et al., 2025).

Investigation into the influence of the physicochemical properties on the distribution patterns of the studied compounds in the microcosms revealed that the fractions of AHs, on most of the occasions, showed moderate-to-strong relationships ($0.40 \leq R^2 \leq 0.92$) with the combination of their respective log K_{OW} and log K_H values throughout the experiment, depending on the microcosm compartment (Table 3.2). Varying directions of the relationships indicate that the upward and downward distribution patterns of AHs are affected by log K_{OW} and log K_H in differing manners.

In essence, the loss and the top ice fractions are negatively linked with log K_{OW} and positively with log K_H throughout the experiment (Table 3.2). This indicates that AHs characterized by lower log K_{OW} and greater log K_H values, thus of lower affinity to the organic diesel phase and greater potential for evaporation, respectively, tend to be distributed into the upper ice and potentially released to the air in a greater portion than less volatile counterparts (Payne et al., 1991b). This is confirmed by Figure 3.5 showing that the largest losses were observed for alkylbenzenes, the most volatile among the studied compounds. The change in the relationship direction in the upper ice on day 15 (Table 3.2) can be explained by substantial removal of alkylbenzenes, and LMW alkylnaphthalenes from the upper ice (due to gradual transport to the air), and simultaneous preservation of 3- and 4-ring PAHs (e.g., phenanthrene, anthracene, pyrene) and their alkylated homologues characterized by greater log K_{OW} and lower log K_H values (Figure 3.5d). Similar observations have been reported in Chapter 4, where the distribution of AHs in the upper ice of a crude-oil-in-ice mesocosm was correlated positively with log K_{OW} and negatively with log K_H in a 77-day study.

Moreover, AHs characterized by greater log K_{OW} and lower log K_H values are also present in greater proportions in the middle ice core sections containing the diesel lens (Table 3.2). Preservation of AHs in the bulk diesel can be attributed to their hydrophobic properties, leading to a low propensity of AHs to partition within sea ice and ultimately their hindered displacement out of the ice.

Conversely, the AH fractions in the bottom ice and seawater compartments are negatively associated with the combination of K_{OW} and K_H (Table 3.2), just as reported in Chapter 4. AHs characterized by lower log K_{OW} and lower log K_H values, thus, exhibiting greater propensity to aqueous phases and larger potential for dissolution (e.g., naphthalene and alkylnaphthalenes) are more potently distributed to the bottom ice and the underlying seawater in comparison to more hydrophobic counterparts. Overall, the AH fractions in the bottom ice and seawater showed weaker relationships with both variables relative to those associated with the loss, top and middle ice sections. This observation is highly likely a result of a more profound role of the ice dynamics in the downward transport of AHs, as opposed to their upward migration driven primarily by AH physicochemical properties.

Varying R^2 values across the microcosm compartments throughout the study could be attributed to the intricate structure and highly dynamic nature of growing sea ice. The presence of several phases in sea ice (gaseous, liquid, solid surfaces, and organic phase) facilitates multiple partitioning pathways for AHs in a small, confined space. Moreover, evolving temperature, salinity, volume and phase content in the ice further impact the partitioning (Polcwiartek et al., 2025), transport processes, and the ultimate distribution of diesel components in the microcosms. Therefore, we believe that the equations derived here (Table 3.2) are considered satisfactory and applicable for predicting the distribution of AHs across the seawater-ice-atmosphere interface in a diesel-in-growing-ice spill scenario.

Table 3.2. Dependence of the relative fractions (f_X; %) of the 46 aromatic hydrocarbons on their respective octanol-water partition coefficient and Henry's Law Constant values as fitted with the following equation (X represents the atmospheric loss, top, middle, bottom ice sections or seawater):

$$f_X = b_0 + b_1 log\ K_{OW} + b_2 log\ K_H \qquad (6)$$

where insignificant regressions ($p > 0.05$) are displayed in bold, R^2 represents the coefficient of determination, and SEE corresponds to the standard error of estimate. The 95% confidence intervals for the modelled regression equation coefficients are provided in Table B7.

Microcosm compartment	Date	b_0	b_1	b_2	p-Value	R^2	SEE of estimate
f_{Loss}	Day 3	0.133	–0.015	0.011	$p < 0.001$	0.50	0.016
	Day 5	0.321	–0.036	0.024	$p < 0.001$	0.63	0.027
	Day 8	0.639	–0.070	0.054	$p < 0.001$	0.57	0.066
	Day 15	1.223	–0.117	0.117	$p < 0.001$	0.73	0.092
f_{Top}	Day 3	0.346	–0.018	0.036	$p < 0.001$	0.62	0.031
(Temperature:	Day 5	0.426	–0.022	0.050	$p < 0.001$	0.51	0.054
264.0–267.9 K,	Day 8	–0.090	–0.078	0.007	$p < 0.001$	0.45	0.053
Salinity: 4.3–6.2)	Day 15	–0.230	0.074	–0.035	$p < 0.001$	0.66	0.045
f_{Middle}	Day 3	0.206	0.076	–0.053	$p < 0.001$	0.80	0.039
(Temperature:	Day 5	–0.273	0.136	–0.085	$p < 0.001$	0.91	0.041
265.2–267.7 K,	Day 8	–0.177	0.082	–0.075	$p < 0.001$	0.88	0.036
Salinity: 5.3–8.4)	Day 15	–0.788	0.155	–0.096	$p < 0.001$	0.92	0.043
f_{Bottom}	Day 3	0.249	–0.035	–0.005	$p < 0.001$	0.39	0.027
(Temperature:	Day 5	0.370	–0.058	–0.007	$p < 0.001$	0.42	0.040
267.2–269.4 K,	Day 8	0.268	–0.039	–0.006	$p = 0.002$	0.27	0.038
Salinity: 8.4–8.9)	**Day 15**	**0.195**	**–0.026**	**–0.001**	$\mathbf{p = 0.054}$	**0.18**	**0.035**
$f_{Seawater}$	Day 3	0.066	–0.008	–0.001	$p = 0.018$	0.28	0.010
(Temperature:	Day 5	0.157	–0.020	–0.003	$p = 0.004$	0.33	0.022
270.2–271.1 K,	Day 8	0.364	–0.052	–0.008	$p < 0.001$	0.40	0.039
Salinity: 37.9–50.8)	Day 15	0.605	–0.086	–0.016	$p < 0.001$	0.48	0.057

3.4.3 Evolution of the aromatic hydrocarbons' distribution behaviour across the seawater-ice-atmosphere interface

A general illustration showing the temporal and spatial evolution of the distribution behaviour of diesel fuel and the studied AHs in the microcosms is displayed in Figure 3.7.

With increasing ambient air temperature (Figure B2a), the ice becomes warmer and potentially more permeable (Figure 3.2), facilitating the ongoing upward migration of bulk diesel to the upper ice (Figure 3.4a) and subsequently to the air-ice interface. As a result, by day 15, the atmospheric loss of bulk diesel fuel and TAHs significantly increases over time ($p < 0.05$), contributing to up to 29% (vol.%) and 51% (mass%) removal of diesel fuel and TAHs, respectively (Figure 3.3). For comparison, the evaporative loss of crude oil spilled onto the surface of seawater, characterized by a 90% ice coverage, reached 20% of the initial crude oil volume within the first 72 hours following the spill (Brandvik and Faksness, 2009). Therefore, continuous sea ice cover substantially hinders the evaporation of oil components, ensuring an extended window of opportunity for oil spill response. The fractions of diesel (Figure 3.3) and TAHs (Figure 3.5) expelled into the adjacent water also significantly ($p < 0.05$) increase with time, reaching 6 and 13% of the initial amounts, respectively. The fluxes of TAHs to the air and seawater increase between the two consecutive events until day 8, when they peak and decrease afterwards (Figure 3.6). A reason for this observation is the rapid and substantial loss of alkylbenzenes, the most abundant compounds among the studied AHs in the diesel fuel, early in the experiment (Figure B5). Overall, by day 15, the concentration of TAHs in the seawater compartment reached nearly 1209 $\mu g\ L^{-1}$. This result is particularly alarming, since concentrations of total PAHs as low as 0.4 $\mu g\ L^{-1}$ were found to cause detrimental effects to subarctic fish (Carls et al., 1999).

Since the AHs vary in their physicochemical properties, they exhibit distinct distributions in the microcosms (Figure 3.5). Throughout the experiment, the relative fractions of AHs in the water column, sea ice and atmosphere (Figure 3.5) are mostly moderately-to-well explained by their respective log K_{OW} and log K_H (Table 3.2). While alkylbenzenes are nearly completely lost to the atmosphere by day 15, alkylnaphthalenes are partially released into the air and partially expelled to the water column. On the other hand, 3- and 4-ring PAHs, such as phenanthrene and pyrene, as well as their alkylated homologues, preferentially remain in the diesel lens with a potential for a prolonged retention (Meyer et al., 2009a, 2009b) in sea ice due to interactions with solid ice surfaces (Garnett et al., 2021) and POM (Polcwiartek et al., 2025). Preservation of hydrophobic AHs in sea ice may contribute to long-term exposure for the ice-dwelling organisms.

Since the biological activity (Rysgaard et al., 2014) and biodegradation of AHs (Saltymakova et al., 2025) in the SERF sea ice have been assessed as negligible, the observations reported here are a result of primarily abiotic processes.

3.5 Conclusions

The results from this outdoor microcosm study deliver new insights on the dynamics of diesel fuel and AHs across the seawater-ice-atmosphere over a15-day ice growth period. The determined here diesel fuel and AHs migration patterns, distribution fractions between the microcosm compartments and TAH fluxes throughout the study have vital implications for diesel spill identification, detection and monitoring (Hicks et al., 2024), as well as diesel spill weathering models (Brandvik and Faksness, 2009). The derived equations predicting the relative fractions of AHs in different environmental compartments in a diesel-in-ice spill scenario are vital for the improvement of existing or development of new algorithms in toxicity assessment models.

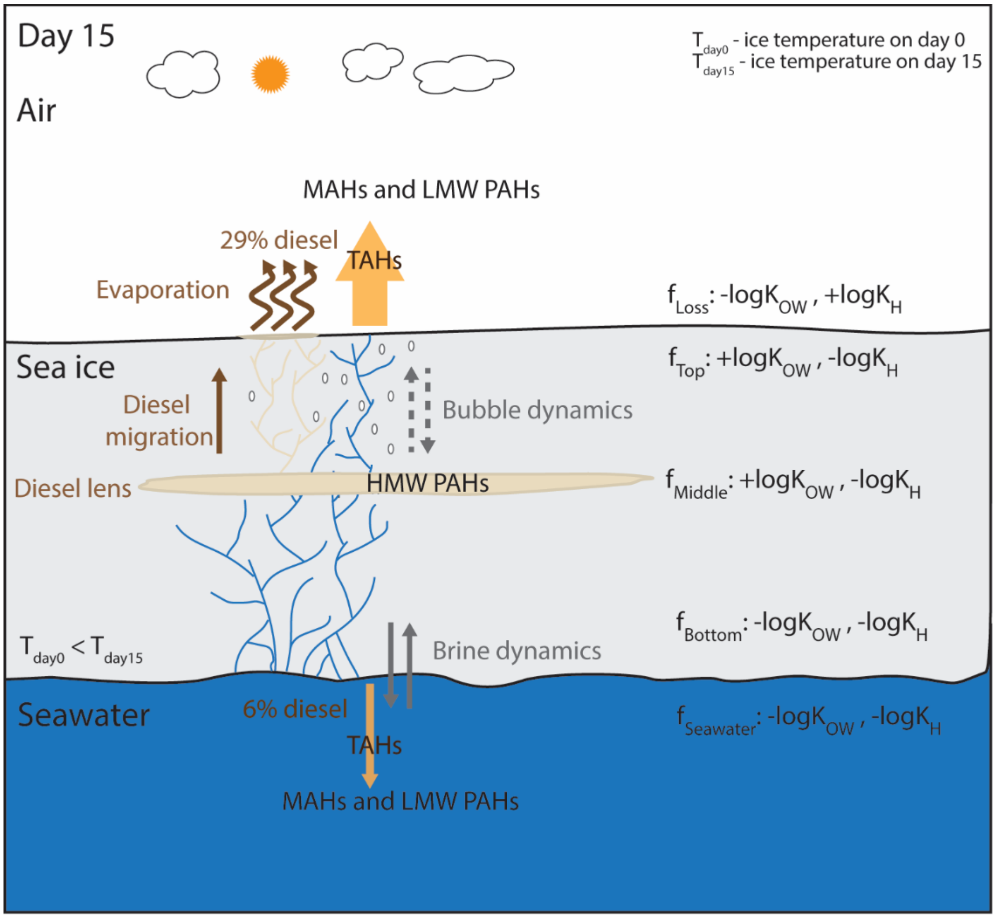

Figure 3.7. A schematic summary of the temporal and spatial distribution of diesel and its aromatic hydrocarbons across the seawater-ice-atmosphere interface in a diesel-in-ice microcosm under cold winter conditions. TAHs: total aromatic hydrocarbons; MAHs: monocyclic aromatic hydrocarbons; LMW PAHs: low-molecular-weight polycyclic aromatic hydrocarbons; HMW PAHs: high-molecular-weight polycyclic aromatic hydrocarbons; f: relative fraction; K_{OW}: octanol-water partition coefficient; K_H: Henry's Law Constant.

Supporting Information

The Supporting Information for this chapter is available in Appendix B.

References

Brandvik, P. J., & Faksness, L.G. 2009. Weathering processes in Arctic oil spills; meso-scale experiments with different ice conditions. Cold Regions Science and Technology, 55: 160–166.

Carls, M. G., Rice, S. D., & Hose, J. E. 1999. Sensitivity of fish embryos to weathered crude oil: Part I. Low-level exposure during incubation causes malformations, genetic damage, and mortality in larval Pacific herring (Clupea pallasi). Environmental Toxicology and Chemistry, 18: 481–493.

Chen, Y., Jia, R., & Yang, S. 2015. Distribution and source of polycyclic aromatic hydrocarbons (PAHs) in water dissolved phase, suspended particulate matter and sediment from weihe river in Northwest China. International Journal of Environmental Research and Public Health, 12: 14148–14163.

Comer, B., Osipova, L., Georgeff, E., & Mao, X. 2020. The international maritime organization's proposed arctic heavy fuel oil ban: Likely impacts and opportunities for improvement. The International Council on Clean Transportation, Washington, DC. Accessed September 12, 2020.

Cox, G. F. N., & Weeks, W. F. 1983. Equations for Determining the Gas and Brine Volumes in Sea-Ice Samples. Journal of Glaciology, 29: 306–316.

Crabeck, O., Delille, B., Rysgaard, S., Thomas, D. N., Geilfus, N. X., Else, B., & Tison, J. L. 2014. First "in situ" determination of gas transport coefficients (D_{O2}, D_{Ar}, and D_{N2}) from bulk gas concentration measurements (O_2, N_2, Ar) in natural sea ice. Journal of Geophysical Research: Oceans, 119: 6655–6668.

Crabeck, O., Galley, R., Delille, B., Else, B., Geilfus, N.-X., Lemes, M., Des Roches, M., Francus, P., Tison, J.-L., & Rysgaard, S. 2016. Imaging air volume fraction in sea ice using non-destructive X-ray tomography. The Cryosphere, 10: 1125–1145.

Desmond, D. S., Saltymakova, D., Neusitzer, T. D., Firoozy, N., Isleifson, D., Barber, D. G., & Stern, G. A. 2019. Oil behavior in sea ice: Changes in chemical composition and resultant effect on sea ice dielectrics. Marine Pollution Bulletin, 142: 216–233.

Faksness, L.-G., & Brandvik, P. J. 2008a. Distribution of water soluble components from Arctic marine oil spills — A combined laboratory and field study. Cold Regions Science and Technology, 54: 97–105.

Faksness, L.-G., & Brandvik, P. J. 2008b. Distribution of water soluble components from oil encapsulated in Arctic sea ice: Summary of three field seasons. Cold Regions Science and Technology, 54: 106–114.

Fingas, M., & Hollebone, B. P. 2015. Oil Behavior in Ice-Infested Waters. In Oil Spill Science and Technology. John Wiley & Sons. 271–284.

Fingas, M. F., & Hollebone, B. P. 2003. Review of behaviour of oil in freezing environments. Marine Pollution Bulletin, 47: 333–340.

Gao, Z., Geilfus, N.-X., Saiz-Lopez, A., & Wang, F. 2022. Reproducing Arctic springtime tropospheric ozone and mercury depletion events in an outdoor mesocosm sea ice facility. Atmospheric Chemistry and Physics, 22: 1811–1824.

Gao, Z., Munson, K., & Wang, F. 2024. Temporal Evolution of Gaseous Mercury Across the Sea Ice-Seawater Interface: A Mesocosm Study. Journal of Geophysical Research: Oceans, 129: 1–13.

Garnett, J., Halsall, C., Thomas, M., Crabeck, O., France, J., Joerss, H., Ebinghaus, R., Kaiser, J., Leeson, A., & Wynn, P. M. 2021. Investigating the Uptake and Fate of Poly- and Perfluoroalkylated Substances (PFAS) in Sea Ice Using an Experimental Sea Ice Chamber. Environmental Science and Technology, 55: 9601–9608.

Garnett, J., Halsall, C., Thomas, M., France, J., Kaiser, J., Graf, C., Leeson, A., & Wynn, P. 2019. Mechanistic Insight into the Uptake and Fate of Persistent Organic Pollutants in Sea Ice. Environmental Science and Technology, 53: 6757–6764.

Golden, K. M., Ackley, S. F., & Lytle, V. I. 1998. The Percolation Phase Transition in Sea Ice. Science, 282: 2238–2241.

Golden, K. M., Eicken, H., Heaton, A. L., Miner, J., Pringle, D. J., & Zhu, J. 2007. Thermal evolution of permeability and microstructure in sea ice. Geophysical Research Letters, 34: 1–6.

Hicks, L., Zabihi Mayvan, M., Asihene, E., Desmond, D. S., Polcwiartek, K., Stern, G. A., & Isleifson, D. 2024. Assessment of C-Band Polarimetric Radar for the Detection of Diesel Fuel in Newly Formed Sea Ice. Remote Sensing, 16: 1–18.

Karlsson, J., Petrich, C., & Eicken, H. 2011. Oil entrainment and migration in laboratory-grown saltwater ice. Proceedings of the International Conference on Port and Ocean Engineering under Arctic Conditions (POAC), 1: 88–97.

Kuppusamy, S., Maddela, N. R., Megharaj, M., & Venkateswarlu, K. 2019. Total Petroleum Hydrocarbons: Environmental Fate, Toxicity, and Remediation, Springer International Publishing. 1–55.

Kwok, R., & Cunningham, G. F. 2008. ICESat over Arctic sea ice: Estimation of snow depth and ice thickness. Journal of Geophysical Research. C. Oceans, 113: 1–17.

Lau, S.-L., & Stenstrom, M. K. 1997. Solid-Phase Extraction for Oil and Grease Analysis. Water Environment Research, 69: 368–374.

Loose, B., Schlosser, P., Perovich, D., Ringelberg, D., Ho, D. T., Takahashi, T., Richter-Menge, J., Reynolds, C. M., McGillis, W. R., & Tison, J. L. 2011. Gas diffusion through columnar laboratory sea ice: implications for mixed-layer ventilation of CO_2 in the seasonal ice zone. Tellus B: Chemical and Physical Meteorology, 63: 23–39.

Meyer, T., Lei, Y. D., Muradi, I., & Wania, F. 2009a. Organic Contaminant Release from Melting Snow. 1. Influence of Chemical Partitioning. Environmental Science and Technology, 43: 657–662.

Meyer, T., Lei, Y. D., Muradi, I., & Wania, F. 2009b. Organic contaminant release from melting snow. 2. Influence of snow pack and melt characteristics. Environmental Science and Technology, 43: 663–668.

Notz, D., & Worster, M. G. 2009. Desalination processes of sea ice revisited. Journal of Geophysical Research, 114: 1–10.

Oggier, M., Eicken, H., Wilkinson, J., Petrich, C., & O'Sadnick, M. 2020. Crude oil migration in sea-ice: Laboratory studies of constraints on oil mobilization and seasonal evolution. Cold Regions Science and Technology, 174: 1–16.

PAME. 2025. Arctic Shipping Status Report #1. The increase in Arctic Shipping: 2013-2024. https://hdl.handle.net/11374/2733.3. Accessed June 10, 2025.

Pampanin, D., & Sydnes, M. O. 2013. Polycyclic Aromatic Hydrocarbons: A Constituent of Petroleum: Presence and Influence in the Aquatic Environment. In Hydrocarbon. 83–118.

Payne, J. R., Hachmeister, L. E., McNabb, G. D., Sharpe, H. E., Smith, G. S., & Menen, C. A. 1991a. Brine-induced advection of dissolved aromatic hydrocarbons to Arctic bottom waters. Environmental Science and Technology, 25: 940–951.

Payne, J. R., McNabb Jr, G. D., & Clayton. Jr, J. R. 1991b. Oil-weathering behavior in Arctic environments. Polar Research, 10: 631–662.

Petrich, C., & Eicken, H. 2017. Overview of sea ice growth and properties. In Sea Ice, 1–41.

Petrich, C., Karlsson, J., & Eicken, H. 2013. Porosity of growing sea ice and potential for oil entrainment. Cold Regions Science and Technology, 87: 27–32.

Polcwiartek, K., Stern, G. A., & Wang, F. 2025. Incorporation and Distribution of Polycyclic Aromatic Hydrocarbons in Experimental Sea-Ice. Environmental Science and Technology, 59: 7310–7319.

Rysgaard, S., Wang, F., Galley, R. J., Grimm, R., Notz, D., Lemes, M., Geilfus, N. X., Chaulk, A., Hare, A. A., Crabeck, O., Else, B. G. T., Campbell, K., Sørensen, L. L., Sievers, J., & Papakyriakou, T. 2014. Temporal dynamics of ikaite in experimental sea ice. The Cryosphere, 8: 1469–1478.

Saltymakova, D., Desmond, D. S., Isleifson, D., Firoozy, N., Neusitzer, T. D., Xu, Z., Lemes, M., Barber, D. G., & Stern, G. A. 2020. Effect of dissolution, evaporation, and photooxidation on crude oil chemical composition, dielectric properties and its radar signature in the Arctic environment. Marine Pollution Bulletin, 151: 110629.

Saltymakova, D., Desmond, D. S., Smith, A. F., Bautista, M. A., Collins, E., Polcwiartek, K., Snyder, N., Wolfe, T., Hubert, C., Isleifson, D., & Stern, G. 2025. Enhanced crude oil degradation observed in sea ice following bioaugmentation with arctic bacteria. Marine Environmental Research, 204: 106942.

Chapter 4 Distribution of Aromatic Hydrocarbons of a Crude Oil in Experimental Sea Ice: A Mesocosm Study

Building on the sea ice microcosm studies of a simple mixture of four PAHs (Chapter 2) and of a complex diesel fuel (Chapter 3), this chapter examines the behaviour of a more complex crude oil in sea ice at a larger mesocosm scale. It investigates air bubble- and brine-mediated transport pathways and the distribution behaviour of low-molecular-weight volatile and water-soluble aromatic hydrocarbons of the crude oil in sea ice. This chapter also provides empirical equations linking concentrations of aromatic hydrocarbons throughout the ice with their respective K_{OW} and K_H. The manuscript is currently under preparation for journal submission.

Contributions of Authors

I participated in the experiment's conceptualization, which was a part of a GENICE study led by Dr. Gary Stern (GS) and assisted with Dr. Diana Saltymakova (DS) and Dr. Alastair Smith (AS). I developed and carried out the sample collection strategy with the participation of DS, Nolan Snyder (NS) and Durell Desmond (DD). I performed the analytical method development, sample analysis, data processing, visualization and interpretation under the supervision of Dr. Feiyue Wang (FW) and GS. I worked with FW and GS on the writing of the manuscript.

Abstract

Climate change-induced sea ice decline in the Arctic is perceived as an opportunity for increased anthropogenic activities, contributing to an elevated risk of oil spills in the Arctic Ocean. While volatile and water-soluble aromatic hydrocarbons are among the most toxic components in crude oils, their fate and behaviour in ice-covered marine waters are poorly studied. Here, we present a 77-day outdoor crude oil-in-ice mesocosm study to investigate the distribution behaviour of alkylbenzenes and alkylnaphthalenes of the crude oil in experimental first-year sea ice. We demonstrate that the more volatile alkylbenzenes are rapidly lost to the atmosphere through evaporation, whereas the more water-soluble alkylnaphthalenes tend to be retained in the upper ice and transported downwards to the bottom ice and eventually to the underlying water column. The concentration ratios of the studied aromatic hydrocarbons in the top or bottom ice core sections relative to the middle ice core sections (where the crude oil was originally injected), R_{TM} and $R_{BM,}$ respectively, are well predicted from their octanol-water partition coefficients and Henry's Law Constant throughout the experimental sea ice growth period. Insight into the distribution patterns of the most water-soluble crude oil components and the role their properties play in the process will warrant more precise predictions of low-molecular-weight aromatic hydrocarbons should a crude oil spill occur in the sea ice environment.

4.1 Introduction

Increasing temperatures in the Arctic region induced by climate change led to rapid melting of sea ice, resulting in shrinking and thinning of the Arctic ice cover (Kwok and Cunningham, 2008; Simmonds, 2015). Consequently, the Arctic is becoming more open to steadily increasing marine transit and destination shipping traffic (Dawson et al., 2018), fossil fuel exploration and extraction activities, and other industrial affairs. Thus, the increasing likelihood of crude oil spills and oil-related contamination in the Arctic marine environment is plausible. The toxicity of oils is often associated with the presence of low-molecular-weight AHs (e.g., BTEX compounds and naphthalene and its alkylated homologues), which are known to cause adverse effects to aquatic organisms (Johnson et al., 2018; Ucan-Marin and Dupuis, 2015). However, the fate and transport of those LMW AHs in the Arctic cryosphere in the aftermath of a crude oil spill are not fully understood.

Following a crude oil release in open water or partially ice-covered water, LMW AHs tend to rapidly evaporate into the atmosphere owing to their high vapour pressures (Incardona et al., 2013; Wang et al., 1995). Despite their good solubility in water, their dissolution becomes a secondary process (Spaulding, 1988) as the evaporation rate is much greater than that of dissolution (Riazi and Edalat, 1996). The fate of volatile and water-soluble AHs becomes more complex if crude oil is entrapped within a layer of growing young sea ice. The transport pathways for oil constituents will be strictly limited to openings and connections in sea ice, such as air and brine inclusions (Wang et al., 2017).

Crude oil-in-ice scenario studies have demonstrated that LMW aliphatic compounds are transported from an entrapped oil lens to the air-ice interface *via* evaporation (Desmond et al., 2019; Payne et al., 1991b; Saltymakova et al., 2020). Conversely, LMW alkylbenzenes (Payne et al., 1991a), LMW PAHs (Faksness and Brandvik, 2008a, 2008b) and HMW heterocyclic oil compounds (Desmond et al., 2019) dissolve in sea ice brine and are subsequently transported downward to the underlying seawater *via* brine drainage. Under quiescent ocean current conditions, brine-associated dissolved compounds can potentially be transported to the deep ocean and benthic layer by brine-mediated sinking (Payne et al., 1991a). Since evaporation of spilled crude oil is reduced by a sea ice cover (Brandvik and Faksness, 2009), dissolution of oil constituents will likely increase, potentially increasing their Toxic Equivalency (TEQ) in Arctic waters. It has been demonstrated that downward transport of water-soluble oil constituents from an oil lens entrapped in sea ice can persist for several months (Faksness and Brandvik 2008a), thus posing prolonged and chronic exposure to the sea-ice communities and biota relying on the under-sea ice boundary layer.

Distribution of petrogenic AHs within sea ice and across the seawater-sea-ice-atmosphere interface is driven by physicochemical properties of AHs, and sea ice dynamics, in particular, migration of brine and air bubbles in sea ice. Physicochemical properties, such as vapour pressure, aqueous solubility, Henry's Law Constant, octanol-water partition coefficient, and octanol-air partition coefficient, control partitioning of AHs between different compartments (e.g., air bubbles, liquid brine, solid ice crystal surfaces, POM in sea ice), whereas sea ice dynamics distribute chemicals within and out of the ice. However, the interplay between the physicochemical properties of the chemicals and sea ice dynamics in driving the spatial and temporal distribution of crude oil AHs remains poorly studied.

Building on the results presented in Chapters 2 and 3, this chapter examines a more complex oil (crude) at a mesocosm scale, instead of a microcosm scale. Here we report the results of a 77-day outdoor crude oil-in-sea-ice experiment investigating the distribution patterns of 39 alkylbenzenes and alkylnaphthalenes. We studied their spatial and temporal distributions across the experimental young sea ice, examined the role of brine and air bubble dynamics in their transport within the ice, determined the relationships between the vertical distribution patterns of the studied compounds and their respective physicochemical properties, and derived empirical equations predicting their distribution in the upper and bottom ice from their respective log K_{OW} and log K_H.

4.2 Materials and Methods

4.2.1 Experiment overview

This study was a part of an outdoor crude oil-in-sea-ice-mesocosm experiment (Desmond et al., 2021b; Saltymakova et al., 2024; Saltymakova et al., 2025) performed from January 8 to April 27, 2018, at the University of Manitoba's Sea-ice Environmental Research Facility in Winnipeg, Canada. A 3 m diameter by 1 m deep fibreglass tub (built by Structural Composite Technologies Ltd., Winnipeg) was filled with formulated seawater prepared from groundwater and salts, with a salinity and major ion composition resembling that of Standard Seawater at a salinity of 33, similar to surface Arctic seawater (Crabeck et al., 2016; Gao et al., 2022). A detailed description of the artificial seawater preparation can be found in Gao et al. (2022). Next, the mesocosm was exposed to outdoor winter conditions. Sea ice formation in the mesocosm began on January 8. On January 23 (designated as day 0), 6.6 L of light and sour crude oil (Tundra Oil & Gas Partnership Ltd.) was injected into a water column under a ~25 cm ice cover through a ~ 3-cm in diameter PVC pipe fixed to the bottom of the tub. The ice kept growing, reaching a maximum thickness of ~51 cm on day 52 (March 16). The experiment was terminated on day 94 (April 27), when the ice completely melted due to the warming ambient air temperature. Samples for this study were collected until day 77 (April 10), when sea ice was still present but was rapidly deteriorating. Figure 4.1 shows a schematic and a photograph of the mesocosm tub.

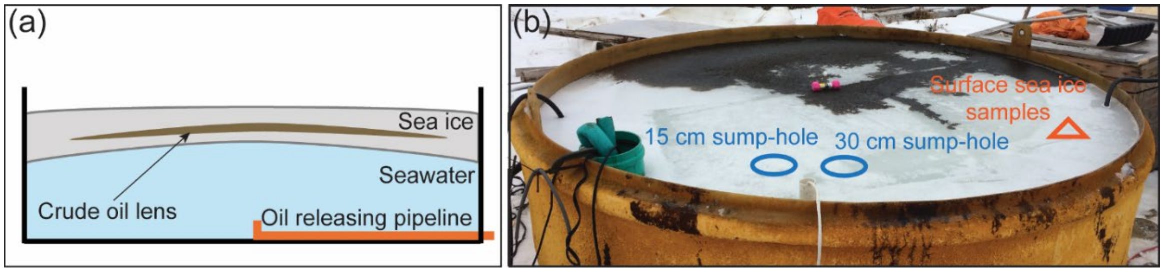

Figure 4.1. A schematic (a) and a photograph (b) of the experimental fibreglass tub used to carry out the crude oil-in-sea-ice mesocosm study at the Sea-ice Environmental Research Facility, Winnipeg, Canada. Also shown are the locations of collected brine (blue circles) and surface sea ice (orange triangle) samples.

4.2.2 Sampling procedure

Three types of samples, including surface sea ice, brine and sea ice core samples, were collected throughout the experiment. A schematic showing the steps followed during the sample collection is provided in Figure C1 in Appendix C.

4.2.2.1 Surface sea ice

Surface sea ice samples were collected on days 1, 2, 3, 6, and 10, following the crude oil injection. During each sampling event, a 2 mm thick layer of ice surface was scraped with a stainless-steel spoon from a location with no visible crude oil (Figure 4.1b). Approximately 10 mL (n = 2) of surface ice scrapes were placed in 20 mL airtight clear glass Agilent headspace vials during each sampling event. The surface sea ice samples were collected from the same area during consecutive sampling events.

4.2.2.2 Sea ice cores

Sea ice cores were collected on four occasions at different stages of sea ice evolution corresponding to 15-, 34-, 52- and 77-days post-crude oil injection. During each sampling event, three ice cores were extracted using a 9-cm diameter core barrel (Kovacs Enterprise Mark II coring system), except on day 77, when only two ice cores were collected. Next, the ice cores were horizontally sliced into three vertical segments (top, middle, bottom) using a sterilized hand saw (DeWalt). The top section related to 20% of the ice core length from the ice surface, and the remaining segment was sliced at its mid-depth, giving the middle and bottom sections, respectively. More details pertaining to the reasoning of the ice core slicing protocol can be found in Desmond et al. (2021b) and Saltymakova et al. (2024). Prior to the horizontal sectioning of the ice cores, the temperature of the ice was measured at the center of each ice section. This was conducted by drilling a 5-mm diameter hole perpendicular to the core length at each depth and measuring the temperature with a digital temperature probe (Traceable).

Following the ice core sectioning, approximately 10 mL of ice was sampled from each ice core section using a small ceramic blade knife (Starfrit, Amazon). The ice samples were placed in the same 20 mL airtight headspace vials as described above. The top and bottom ice sections were subsampled at mid-depth of each slice, whereas the middle sections were subsampled at the crude oil lens encapsulation depth. The remaining bulk sea ice core sections were dedicated to a parallel study investigating crude oil biodegradation potential as detailed in Saltymakova et al. (2025).

4.2.2.3 Brine

Brine samples were obtained by drilling sump-holes in the ice at depths of 15 cm and 30 cm using a 9-cm diameter core barrel (Figure C2). Two adjacent sump-holes (Figure 4.1b) were drilled on day 20 (February 12) at 11:00 AM local time. Immediately after drilling, the holes were tightly closed with styrofoam caps. Approximately 5 hours later, the brine accumulated in each sump-hole was collected using a glass turkey baster (DK Hardware) and was transferred into 50 mL amber glass jars with PTFE-lined caps. Next, 10 mL of the brine (n = 3) was subsampled from each jar into the same type of 20 mL airtight glass headspace vials. The brine samples were collected from the same sump-holes again on day 24 (February 16). The brine content in the holes froze on the following night, so no sampling was carried out after that. The temperature of the brine was measured during each sampling event using a digital temperature probe (Traceable) shortly before its extraction from the sump-holes.

4.2.3 Sample preparation and analysis

Immediately after collection, all the surface sea ice, brine and sea ice core samples were spiked on site with 50 µL of 1000 µg L^{-1} of deuterated benzene (Benzene-D_6) (prepared from Sigma Aldrich, Certified Reference Material, 2000 mg L^{-1} in methanol) as an internal standard. Then, the vials were tightly closed and stored in the freezer at –20 °C until the analysis. Before the analysis, the samples were melted at 4 °C.

The analysis of the collected samples was performed on a GC (Agilent 7890B) coupled with an MS/MS (Agilent 7010B) and combined with a static headspace (SHS) injection mode. The SHS-GC-MS/MS system was equipped with PAL RSI 85 autosampler, a Rxi-PAH analytical column (60 m×250 µm×0.1 µm) and helium as the carrier gas at a constant flow of 1.0 mL min^{-1}. The electron ionization energy was 70 eV. The oven regime was set as follows: 40 °C (5 min hold), 20 °C min^{-1} to 120 °C, 3 °C min^{-1} to 200 °C, with a 5 min hold giving a total run time of 40.7 min. The sample equilibration was performed in a thermostat at 80 °C for 20 min. The syringe temperature was 85 °C.

Since the samples varied considerably in the content of crude oil (from oil being nonvisible to highly oily samples) due to heterogeneity of lateral and vertical oil migration, the acquisition method parameters, such as injection volume and split injection ratio, were adjusted based on the crude oil content in the samples. Table C1 presents detailed information on the analytical method with acquisition parameters depending on the type of samples.

The identification of alkylbenzenes and alkylnaphthalenes in the crude oil mixture was carried out by analyzing a reference sample of fresh crude oil in full scan mode to obtain mass spectral data. The obtained compound's mass spectra and retention times were compared with those of the standard compounds, as well as with the mass spectrum National Institute of Standards and Technology (NIST) library information (version 2.0f, October 2008). In total, 39 compounds were identified in the studied crude oil; the complete list of the identified AHs and the used standard solutions is shown in Table 4.1.

Table 4.1. List of the identified aromatic hydrocarbons along with their respective acronyms and standard solutions used for their identification.

Compound	Acronym	Standard solution
Ethylbenzene	EB	502.2 Calibration Mix #5, Restek
p-xylene	p-X	
o-xylene	o-X	
1,2,4-trimethylbenzene	1,2,4-TMB	
sec-butylbenzene	sec-BB	
n-butylbenzene	n-BB	
m-xylene	m-X	502.2 Calibration Mix #4, Restek
Isopropylbenzene	iso-PB	
n-propylbenzene	n-PB	
1,3,5-trimethylbenzene	1,3,5-TMB	
1,2,3-trimethylbenzene	1,2,3-TMB	
3-ethyltoluene	3-ET	Mixture of 46 alkylated benzenes and PAHs, Chiron
4-ethyltoluene	4-ET	
2-ethyltoluene	2-ET	
1,3-diethylbenzene	1,3-DEB	
1,4-diethylbenzene	1,4-DEB	
1,2-diethylbenzene	1,2-DEB	
1,2,4,5-tetramethylbenzene	1,2,4,5-TeMB	
1,2,3,5-tetramethylbenzene	1,2,3,5-TeMB	
2-methylnaphthalene	2-MN	
1-methylnaphthalene	1-MN	
2-ethylnaphthalene	2-EN	
1-ethylnaphthalene	1-EN	
2,6-dimethylnaphthalene	2,6-DMN	
2,7-dimethylnaphthalene	2,7-DMN	
1,8-dimethylnaphthalene	1,8-DMN	
1,3-dimethylnaphthalene	1,3-DMN	
1,7-dimethylnaphthalene	1,7-DMN	
1,6-dimethylnaphthalene	1,6-DMN	
2,3-dimethylnaphthalene	2,3-DMN	
1,4-dimethylnaphthalene	1,4-DMN	
1,5-dimethylnaphthalene	1,5-DMN	
1,3,7-trimethylnaphthalene	1,3,7-TMN	
2,3,6-trimethylnaphthalene	2,3,6-TMN	
1,4,6-trimethylnaphthalene	1,4,6-TMN	
1,4,5-trimethylnaphthalene	1,4,5-TMN	
2,4,5-trimethylnaphthalene	2,4,5-TMN	
2,3,5-trimethylnaphthalene	2,3,5-TMN	
1,2,6-trimethylnaphthalene	1,2,6-TMN	
1,2,4-trimethylnaphthalene	1,2,4-TMN	
1,4,6,7-tetramethylnaphthalene	1,4,6,7-TeMN	
1,2,5,6-tetramethylnaphthalene	1,2,5,6-TeMN	

Quantitative analysis of the identified analytes was achieved using an external standard calibration approach with a single internal standard. A single internal standard quantification approach had been applied in previous studies using a static headspace injection technique combined with a GC-MS/MS system (Oliver-Pozo et al., 2015; Orazbayeva et al., 2017). All standard solutions and field samples were analyzed using the SIM mode. A detailed description of the targeted ions is provided in Table C2. A linear working concentration range for all analytes for calibration curves was established for each acquisition method (Table C1) separately, with a coefficient of determination greater than 0.95. Due to very close retention times, compound pairs including m-xylene and p-xylene (m/p-X), 3-ethyltoluene and 4-ethyltoluene (3/4-ET), as well as 1-ethylnaphthalene and 2-ethylnaphthalene were quantified as a sum of two isomers (1/2-EN) were quantified as a sum of two isomers.

Following the sample analysis, the salinity of the brine samples and melted sea ice core samples was measured using an Orion Star A212 conductivity meter (Thermo Scientific).

4.2.4 Quality control

On each sampling date, a seawater blank (500 mL) and a hexane blank (500 mL) were exposed to the surrounding environment for about 7 hours. The collected field blanks were then subsampled into headspace vials (10 mL; n = 3) and were analyzed following the same protocol as the regular samples. The studied analytes were not detected in the field blanks.

The SHS-GC-MS/MS system was tuned and validated before and after a sequence of standard and sample runs. Experimental seawater and Milli-Q water blanks, as well as quality control standard duplicates, were run every five samples to ensure the instrument repeatability was sustained. The quality control standard duplicate variability was within 10%.

Since the sea ice core samples were collected from different ice depths, their salinity varied, and it was not practical to match the matrix of the calibration standards to that of sea ice. Therefore, the external standard solutions were prepared in Milli-Q water instead. To determine how salt content impacted the analyte partitioning from the aqueous sample fraction to the headspace fraction during the sample equilibration in the thermostat (prior to sample analysis), additional analyses were run for the salinity range (0–20) of the sea ice core samples. The relative standard deviation of the detector signal for the targeted analytes varied from 6.9 to 11.4%, depending on the compound. The final concentrations of the studied analytes were corrected by using relative response factors (RRF) calculated for the salt-containing standard solution matrices.

The limit of quantification (LOQ) was established based on a signal-to-noise ratio of 10:1. The LOQ values ranged from 4.1 to 6.8 ng L^{-1} for oily samples and varied between 0.8 and 1.7 ng L^{-1} for samples that contained nonvisible oil, depending on the compound (Table C1).

4.2.5 Data analysis

The V_B values of the respective sea ice core samples were calculated from the sea ice temperature and bulk ice salinity based on the formula of Cox and Weeks (1983). The ice growth rate was calculated by dividing the ice thickness growth (cm) between the two consecutive measurement dates by the period the growth occurred (day).

Compound concentration ratios in the top (R_{TM}) or bottom (R_{BM}) ice core section to those in the middle ice core section were calculated by the following equation:

$$R_{TM} = \frac{C_T}{C_M} \qquad (7)$$

$$R_{BM} = \frac{C_B}{C_M} \qquad (8)$$

where C_T, C_B and C_M correspond to a compound concentration in the top, bottom and middle sea ice core sections, respectively.

The values of the physicochemical properties of the studied alkylbenzenes and alkylnaphthalenes (e.g., vapour pressure, aqueous solubility, Henry's Law Constant, octanol-water partition coefficient, and octanol-air partition coefficient) at 25 °C and salinity of fresh water were estimated using an open-source modelling software QSAR. The values of the computed properties of the studied compounds are provided in Table C3.

Statistical analysis was carried out using SigmaPlot 14.0 (Systat Software Inc.). Student's t-test and one-way ANOVA were used to examine the statistical difference under various conditions (e.g., to compare: abundance ratios of a compound in surface samples over time; R_{TM} or R_{BM} ratio values of the respective compounds over time; R_{TM} and R_{BM} ratio values of the respective compounds at a certain point in time; R_{TM} or R_{BM} ratio values of alkylbenzenes *vs* alkylnaphthalenes), and the significant level was set at 0.05 for each test. Regression analyses were used to determine the relationships between analyte concentrations and bulk ice salinity. Spearman Rank Order Correlation analysis was used to establish the strength and direction of the monotonic relationships between the R_{TM} or R_{BM} ratio values of the identified AHs and their respective physicochemical properties. Multiple linear regression analysis was used to derive empirical equations linking the analyte's R_{TM} and R_{BM} ratios in the ice with its respective K_{OW} and K_H values based on the following general equation:

$$y = b_0 + b_1x_1 + b_2x_2 + \cdots + b_ix_i \qquad (9)$$

where y corresponds to the analyte's R_{TM} or R_{BM} ratio value, b_0 is the intercept, b_1, b_2 and b_i are regression coefficients, and x_1, x_2, x_i are independent variables (e.g., K_{OW}, K_H). Since experimentally derived values for the selected physicochemical properties (e.g., V_P, S_{aq}, K_{OW}, K_H, K_{OA}) are not available for most of the 39 aromatic hydrocarbons, both Spearman Rank Order Correlation and multiple linear regression analyses were conducted using exclusively the QSAR-predicted property values.

4.3 Results

4.3.1 Meteorological, sea ice and brine properties

Throughout the experiment, the ambient air temperature fluctuated between –30 and 5 °C (Figure C3). The ice continued to grow from day 1 and reached the maximal thickness of 51.0 ± 0.1 cm (Table C4) on day 52, with a growth rate varying between 0.1 and 1.7 cm day^{-1}. Melting started after day 52, and the ice thickness decreased to 22.5 ± 9.2 cm by day 77 with an average ice decay rate of 1.1 cm day^{-1}.

The ice temperature varied during the experiment (Figure 4.2a). For instance, on day 15, the ice was relatively cold throughout, with the average temperature at mid-depth of the top and bottom ice sections reaching –9.6 ± 2.4 and –4.5 ± 0.5 °C, respectively. As the ambient air temperature increased, the top and bottom ice temperatures gradually increased to –0.3 ± 0.4 °C and –0.5 ± 0.3 °C, respectively, on day 77. From days 20 and 24, the average brine temperature increased from –13.3 ± 0.1 °C to –9.7 ± 0.1 °C in the 15-cm sump-hole, and from –9.2 ± 0.2 to –2.9 ± 0.1 °C in the 30-cm sump-hole (Figure 4.2a).

While the ice temperature increased over time, the average bulk ice salinity decreased from 11.1 ± 2.7 on day 15 to 1.2 ± 0.3 on day 77 (Figure 4.2b). A C-shaped profile of the bulk ice commonly observed in young and growing natural sea ice (Notz and Worster, 2009) was observed only on day 15 (Figure 4.2b). For the subsequent dates, the bulk ice salinity profiles showed a reversed shape. The salinity of the underlying seawater varied between 33.9 and 51.9 during the study due to the relatively small size of the mesocosm tub.

Between days 20 and 24, the average brine salinity in the 15- and 30-cm sump-holes decreased from 157.2 ± 0.8 to 148.7 ± 0.8 and from 109.2 ± 0.2 to 51.7 ± 0.1, respectively.

The V_B values increased from the top ice core sections (5.2–8.3%) towards the bottom ice core sections (11.3–18.3%), as the ice warmed up with depth (Figure 4.2c).

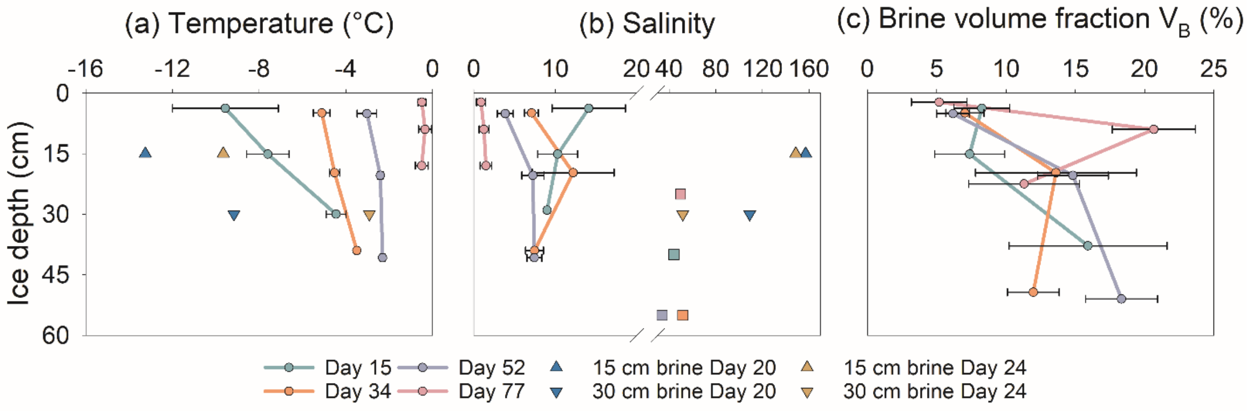

Figure 4.2. Vertical profiles of the average temperature (a), salinity (b), and brine volume fraction (c) across the sea ice column (circle symbols), in the brine (triangle symbols) and the water column (square symbols) in the mesocosm on various sampling days. The uppermost point on the y-axis corresponds to the air-ice interface. Error bars correspond to the respective standard deviations.

4.3.2 Chemical composition of surface sea ice

An example chromatogram (m/z = 105.1–156.1) of a surface sea ice sample is shown in Figure C4a. The concentrations of individual AHs in surface sea ice samples were not obtained due to a lack of a proper method developed for quantitative analysis at that time. Instead, Figure 4.3 shows abundance ratios of the identified alkylbenzenes and alkylnaphthalenes in the surface sea ice samples based on their respective peak areas on days 2 and 6 to those on day 3.

On day 2, only alkylbenzenes were detected in the surface sea ice samples. However, by day 6, all compounds except the lowest-molecular-weight alkylbenzenes (ethylbenzene, xylenes, propylbenzenes) were detected in the surface ice. The average day 2/day 3 ratios of LMW alkylbenzenes ranged from 8.7 ± 0.2 to 14.9 ± 0.7, whereas the average ratio values for the moderate-molecular-weight alkylbenzenes (the remainder of alkylbenzenes) were below 0.6. The average day 6/day 3 ratios of the MMW alkylbenzenes ranged from 0.1 ± 0.0 to 1.4 ± 0.1, whereas for alkylnaphthalenes, the ratio values varied between 1.9 ± 0.3 and 10.9 ± 0.6.

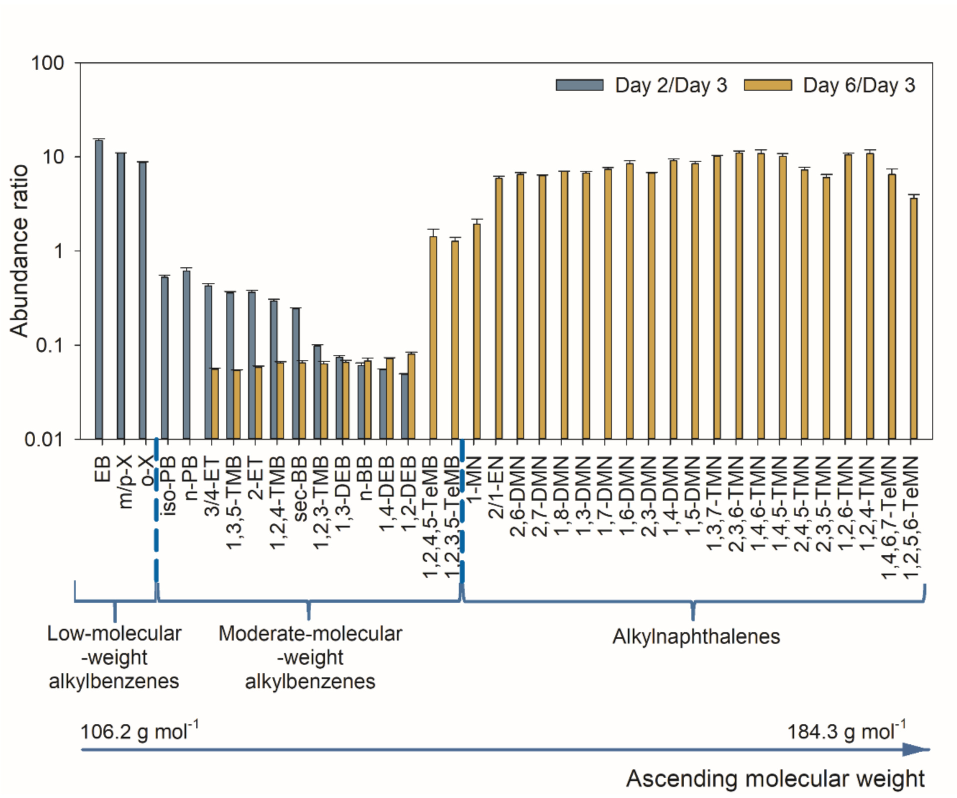

Figure 4.3. Mean ratios of analyte abundances in the surface sea ice samples on day 2 to those on day 3 (blue bars), and on day 6 to those on day 3 (yellow bars). Error bars represent the respective standard deviations.

4.3.3 Distribution of alkylbenzenes and alkylnaphthalenes in sea ice

Figure 4.4 shows concentrations of the monitored aromatic hydrocarbons in the fresh crude oil mixture (Figure 4.4a) and the three vertical sections of the sea ice core collected on day 15. Figure C5 shows vertical distribution concentration profiles of four example alkylbenzenes (ethylbenzene and 1,2,3,5-tetramethylbenzene) and alkylnaphthalenes (1-methylnaphthalene and 1,4,6,7-tetramethylnaphthalene) in the experimental sea ice.

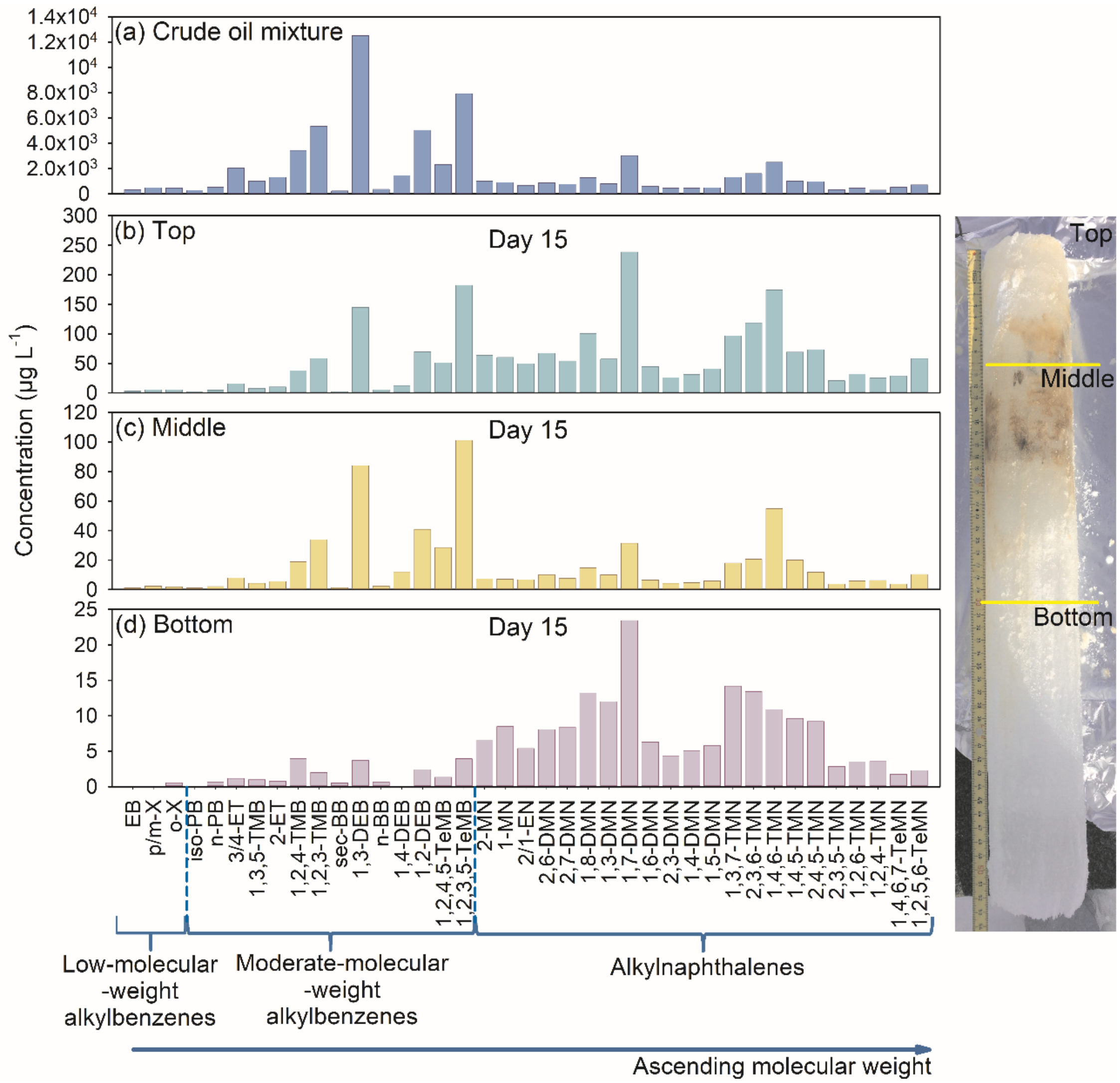

Figure 4.4. Chemical composition profiles of the studied aromatic hydrocarbons in the fresh crude oil mixture (a) and in the sea ice core section samples collected from different ice depths on day 15 (b–d).

The analyte concentrations in the top, middle and bottom ice core sections ranged from 2.4 to 239 µg L^{-1}, 1.1 to 101 µg L^{-1}, and 0.0 to 23.5 µg L^{-1}, respectively, depending on the compound. This gave rise to the total concentration of alkylbenzenes in the top, middle and bottom ice core sections as high as 618, 349 and 22.5 µg L^{-1}, respectively. The total concentration of alkylnaphthalenes in the respective samples reached 1530, 272, and 178 µg L^{-1}, respectively.

The chemical composition profiles of the fresh crude oil mixture and the middle sea ice core sample (Figures 4.4a, 4.4c) were dominated by MMW alkylbenzenes listed between 1,2,4-trimethylbenzene and 1,2,3,5-tetramethylbenzene and several alkylnaphthalenes displayed between 1,3,7-trimethylnaphthalene and 2,4,5-trimethylnaphthalene. The remainder of the compounds were less abundant. Conversely, the top and bottom ice core sections (Figures 4.4b, 4.4d) were dominated by compounds listed between 2-methylnaphthalene and 1,2,5,6-tetramethylnaphthalene.

Calculation of ratios between analyte concentration in the top (T) or bottom (B) sections to those in the middle (M) section (R_{TM} and R_{BM}, respectively) allows for better characterization of differences in the monitored AHs' distribution across sea ice relative to the oil encapsulation depth. Figure 4.5 shows spatial and temporal variations in the R_{TM} and R_{BM} ratios of the studied compounds. The heatmap cells corresponding to the middle ice core sections equal 1.0 and are presented in grey for all the sampling events.

On day 15, concentrations of alkylbenzenes and alkylnaphthalenes in the top ice core sections were greater than those in the middle ice core sections, giving rise to R_{TM} ratio values ranging from 1.1 to 8.6, depending on the compound (Figure 4.5a). Conversely, concentrations of the respective compounds in the bottom ice core sections were lower than those of the middle ice core sections for most of the compounds, resulting in R_{BM} ratio values varying between 0.04 and 1.2. The R_{TM} ratio values for the respective compounds significantly ($p < 0.05$) decreased by day 77 (Figure 4.5d), whereas the R_{BM} ratio values for alkylnaphthalenes significantly ($p < 0.05$) increased with time, reaching values between 12.2 and 35.0 (Figure 4.5c). On the contrary, R_{BM} ratio values for alkylbenzenes remained close to 0 throughout the study; eventually, alkylbenzenes were not detected in the ice on the last sampling event (Figure 4.5d). Overall, R_{TM} and R_{BM} ratio values for alkylnaphthalenes were significantly ($p < 0.05$) greater than those of alkylbenzenes throughout the study.

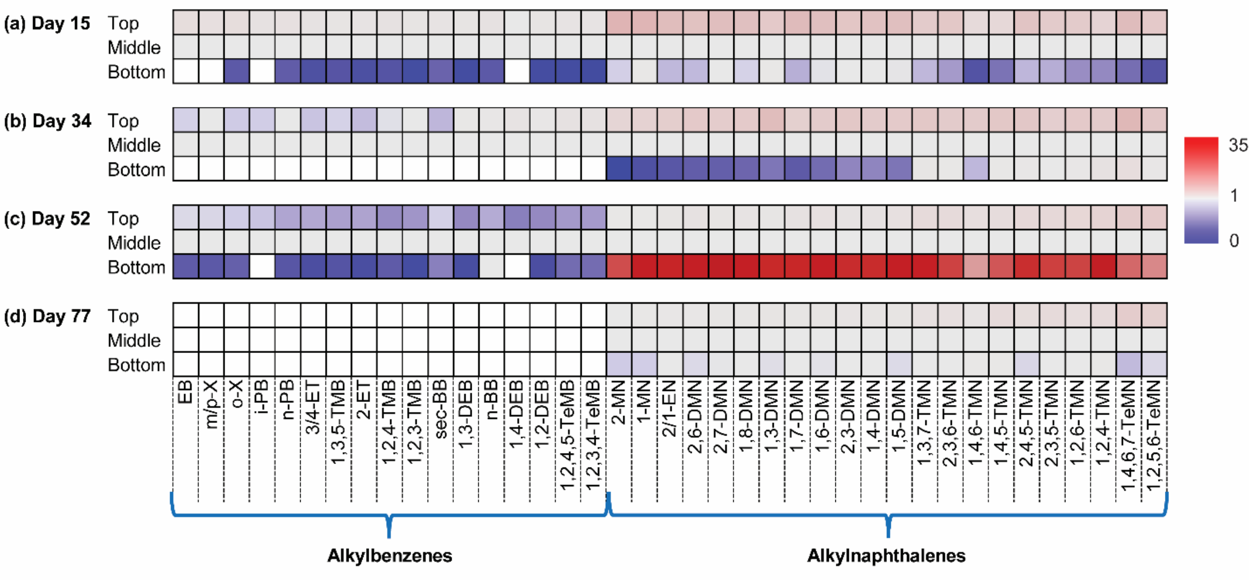

Figure 4.5. Heatmaps illustrating variations in the R_{TM} (ratio of analyte concentrations in the top to that in the middle ice core sections) and R_{BM} (ratio of analyte concentrations in the bottom to that in the middle ice core sections) ratio values of the 39 aromatic hydrocarbons during the four sampling events. The cells displayed in the middle ice core sections correspond to values of 1 and are depicted in grey. Note that cells corresponding to undetected compounds are displayed in white. (Blue: $R < 1$; red: $R > 1$).

4.3.4 Chemical composition of brine samples

Concentrations of the studied AHs in the brine samples collected from the 15-cm and 30-cm sump-holes on day 20 are provided in Figure C6, whereas ratios of analyte concentrations in the brine samples collected on day 20 to those on day 24 collected from the respective sump-holes are shown in Figure 4.6. Specifically, the concentration ratios for the studied compounds varied between 0.1 and 1.4 in the 15-cm sump-hole, depending on the compound. On the other hand, the ratios of the respective compounds in the 30-cm sump-hole ranged between 0.2 and 7.1.

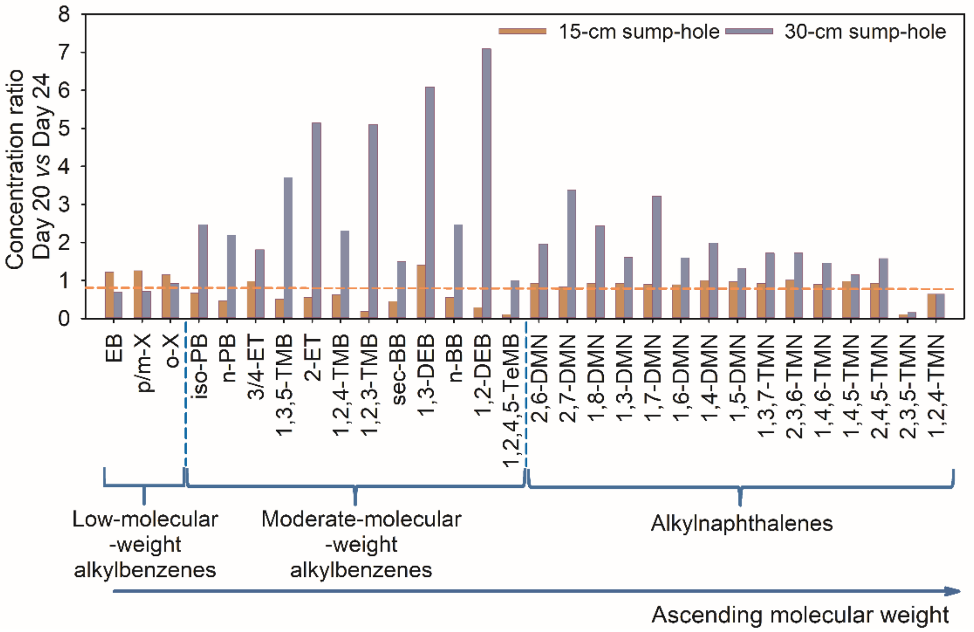

Figure 4.6. Ratios of analyte concentrations in the brine samples collected on day 20 to those on day 24. The brine samples extracted from the 15-cm sump-hole are shown in orange, and those in the 30-cm sump-hole are displayed in blue.

4.4 Discussion

The majority of what we know about oil spills in the natural environment typically comes from two types of events: accidental oil discharges on the one hand, and controlled oil spill initiatives on the other. The latter, however, present a series of challenges considerably limiting their feasibility, such as environmental and ethical considerations, and government or legal restrictions. To address these concerns, we have opted for a mesocosm approach and performed an outdoor crude oil-in-sea-ice experiment to examine the evolution of the distribution behaviour of alkylbenzenes and alkylnaphthalenes throughout the ice. Previous experiments at SERF had demonstrated simulation of the formation and growth of seasonal sea ice characterized by dynamics and geophysical properties of natural young sea ice using mesocosm- and microcosm-based outdoor studies (Gao et al., 2024; Polcwiartek et al., 2025).

4.4.1 Fractionation of alkylbenzenes and alkylnaphthalenes in sea ice

Following the injection under a continuous layer of actively growing sea ice (Figure C1), crude oil became encapsulated within two days, approximately 25 cm below the air-ice interface (Fingas and Hollebone, 2003). A portion of this oil then migrated *via* brine channels from the injection location to the ice surface (Figure 4.1b), likely facilitated by increasing ice temperature (Oggier et al., 2020; Petrich et al., 2013) and the V_B values exceeding the porosity threshold of 5% (Golden et al., 1998; Golden et al., 2007).

The presence of alkylbenzenes and alkylnaphthalenes above and below the oil encapsulation depth in the ice on day 15 (Figures 4.4, C5) indicates their fractionation throughout the ice (Desmond et al., 2019). Since the chemical composition profiles and concentrations of the studied AHs vary throughout the ice (Figure 4.4), this suggests that various oil constituents are transported within sea ice by means of different pathways, owing to compounds' varying physicochemical properties. This is also confirmed by the vertical distribution profiles of the four representative AHs exhibiting varying shapes (Figure C5), which agrees with the results presented in Chapters 2 and 3.

Specifically, the composition profile of the AHs in the upper ice (Figure 4.4b) is dominated by alkylnaphthalenes, whereas in the fresh oil mixture (Figure 4.4a), MMW alkylbenzenes comprise the largest fraction of the studied AHs. Because of their high vapour pressures (Table C3), LMW and MMW alkylbenzenes have likely separated from the encapsulated bulk oil and partitioned into the air inclusions in the ice. Subsequently, they were transported to the ice surface (Figures 4.3, C4a) through buoyant air bubble transfer and/or concentration gradient-driven diffusion in brine channels (Crabeck et al., 2014; Polcwiartek et al., 2025). This is confirmed by Figure 4.3, showing that two days after the oil injection, LMW and MMW alkylbenzenes were detected in the surface ice samples free of oil. On the other hand, the absence of the LMW alkylbenzenes in the surface sea ice samples on day 6 indicates their release to the atmosphere. The concentrations of the monitored compounds in the air just above the mesocosm were not measured.

The presence of alkylbenzenes in the brine collected from the 15-cm sump-hole (Figures 4.6, C6), suggests that alkylbenzenes were partially transported to the air-ice interface through freeze rejection (Liyana-Arachchi et al., 2012), which stems from their good aqueous solubility (Table

C3). However, due to their greater potential for evaporation than dissolution (expressed as greater Henry's Law Constant values; Table C3), brine-mediated transport of alkylbenzenes was likely less important than bubble dynamics.

Conversely, the preservation of alkylnaphthalenes in the upper ice (Figure 4.4b) and their significantly ($p < 0.05$) greater R_{TM} ratios compared to alkylbenzenes (Figure 4.5a) can be attributed to their lower vapour pressures (Table C3) and smaller potential for evaporative loss. Moreover, higher-substituted alkylnaphthalenes, especially tri- and tetramethylnaphthalenes, exhibit relatively high hydrophobicity and affinity to organic and solid phases (expressed as K_{OW}; Table C3), similar to that of 4-ring parent PAHs, such as pyrene ($\log K_{OW} = 4.93$; QSAR predicted value) and chrysene ($\log K_{OW} = 5.52$; QSAR predicted value). Therefore, they have likely partitioned toward ice crystal surfaces (Garnett et al., 2021), POM in the ice (Polcwiartek et al., 2025), or remained in the bulk oil phase that had migrated to the top ice core sections (Desmond et al., 2019). As a result, the oil-, ice surface- or particle-associated alkylnaphthalenes would remain immobilized and preserved in the upper sea ice (Figures 4.4b, 4.5) until upward movement of crude oil or melting of the sea ice matrix.

The observed prevalence of alkylnaphthalenes in the bottom ice (Figure 4.4d) and their high R_{BM} ratio values (Figure 4.5c) result from their active transport to the underlying seawater *via* brine drainage. Since alkylnaphthalenes exhibit reduced vapour pressures and greater potential for dissolution in aqueous phases (Table C3) relative to alkylbenzenes, they have a greater tendency to partition to sea ice brine and thus for enhanced downward transport. Downward migration of alkylnaphthalenes is confirmed by their presence in the 30-cm sump-hole brine (Figures 4.6, C6) and by the results of the study performed in parallel to this work (Saltymakova et al., 2024), demonstrating that alkylnaphthalenes were found in the adjacent seawater. Nonetheless, brine movement, usually responsible for the transport of dissolved chemicals, was found to regulate the distribution of the AHs to a limited extent only. In essence, the concentrations of the three representative compounds exhibited poor relationships ($R^2 = 0.11-0.24$) with bulk ice salinity (Figure C7). These results suggest that the behaviour of AHs in the crude oil-in-ice mesocosm deviates from that of major sea salts. This could be explained by the complexity of the experimental setup, the highly dynamic sea ice environment, interactions between crude oil and ice, as well as interactions between the oil constituents and multiple microcompartments present in the experimental sea ice. Similar observations were noted in Chapters 2 and 3.

Alkylbenzenes were found to represent a substantially smaller fraction in the bottom ice relative to alkylnaphthalenes (Figure 4.4d), and exhibit significantly ($p < 0.05$) lower R_{BM} ratio values than those of alkylnaphthalenes (Figure 4.5). Since the 30-cm sump-hole brine samples contained mostly alkylnaphthalenes (Figure C6), and taking into account that alkylbenzenes tend to have greater potential for evaporation (Table C3), we postulate that they preferentially migrated upward to the air-ice interface rather than to the water column. Alternatively, limited preservation of alkylbenzenes in the bottom ice core sections (Figure 4.5) could be presumably explained by their loss to the adjacent water column through brine drainage (Payne et al., 1991a).

A study conducted in parallel to our work (Saltymakova et al., 2025) reported that biological and microbial activities did not contribute to the changes in the composition of the aromatic hydrocarbons in the crude oil mixture encapsulated within the young experimental sea ice. Therefore, the observed distribution behaviour of AHs throughout the ice in this work is likely primarily a result of physical transport processes.

4.4.2 Role of physicochemical properties in the distribution of aromatic hydrocarbons in sea ice

To illustrate how the physicochemical properties of the 42 alkylbenzenes and alkylnaphthalenes influence their content in the upper and bottom ice, the results of Spearman's rank correlation analysis are provided in Table 4.2. The results indicate moderate-to-strong significant ($p < 0.05$) correlations between the R_{TM} or R_{BM} ratios and V_P, S_{aq}, K_H, K_{OW}, and K_{OA} of the studied AHs (Table 4.2) throughout the experiment. This agrees with Desmond et al. (2019), who demonstrated that the vertical distribution of various crude oil constituents (e.g., PAHs, heterocyclic aromatics, acyclic alkanes, cycloalkanes, alkylbenzenes) across young sea ice showed moderate linear relationships with their molecular mass and volume, vapour pressure and octanol-water partition coefficient. The poor correlations between the R_{BM} ratios and the compounds' properties on day 77 (Table 4.2) are likely a result of warm and melting sea ice and agree with previous observations (Desmond et al., 2019).

Table 4.2. Spearman's rank correlation coefficients of relationships between the R_{TM} and R_{BM} ratios of the 39 aromatic hydrocarbons with their respective physicochemical properties throughout the study. Insignificant correlations ($p > 0.05$) are displayed in bold. The following acronyms V_P, S_{aq}, K_H, K_{OW} and K_{OA} correspond to a compound's vapour pressure, aqueous solubility, Henry's Law Constant, octanol-water partition coefficient, and octanol-air partition coefficient, respectively.

Ratio	Date	V_P (mmHg)	S_{aq} (mg L^{-1})	log K_H (atm m^3 mol^{-1})	log K_{OW}	log K_{OA}
R_{TM}	Day 15	–0.62	–0.33	–0.86	0.48	0.57
	Day 34	–0.88	–0.74	–0.66	0.88	0.87
	Day 52	–0.79	–0.72	–0.63	0.81	0.84
	Day 77	–0.62	–0.94	–0.77	0.93	0.88
R_{BM}	Day 15	–0.47	–0.21	–0.86	0.32	0.41
	Day 34	–0.49	–0.85	–0.69	0.91	0.84
	Day 52	–0.66	–0.47	–0.82	0.59	0.62
	Day 77	**–0.09**	**–0.30**	**0.25**	**0.21**	**0.22**

To further investigate whether the spatial distribution of the AHs within growing sea ice can be predicted from their respective properties, empirical equations were derived using multiple linear regression analysis; the regression results are presented in Tables 4.3 and C5. In essence, linear relationships with R^2 values greater than 0.76 were established for a combination of log K_{OW} and log K_H, which suggests that these parameters are good predictors of the monitored alkylbenzene and alkylnaphthalene R_{TM} and R_{BM} ratio values.

Specifically, the R_{TM} ratios are positively correlated with log K_{OW} and negatively correlated with log K_H on each sampling day, similarly to the regression results reported in Chapter 3, where the relative fractions of the AHs in the middle ice sections and top ice sections on day 15 showed positive relationships with log K_{OW} and negative relationships with log K_H. A greater number of methyl substitutions contributes to a reduced vapour pressure (lower K_H values) and greater hydrophobicity (greater K_{OW}) of a compound, thus leading to its lower propensity for evaporation. As a result, more profound persistence of higher-substituted alkylnaphthalenes in the upper ice is promoted.

On the other hand, the R_{BM} ratios show negative correlations with both properties on each sampling day, except on day 77, when the fitting produced insignificant relationships ($R^2 = 0.04$; Table 4.3). The observed here negative correlations between the R_{BM} values and log K_{OW} and log K_H agree with the regression directions reported in Chapter 3. Negative relationships between both properties and the R_{BM} ratios indicate that the content of the AHs in the bottom ice relative to the middle ice will be greater for less hydrophobic compounds characterized by greater potential for dissolution in sea ice fluids (Table C3). Dissolution of hydrophobic higher-substituted alkylnaphthalenes in saline brine (Figure 4.2b) will be more profoundly reduced due to a salting-out effect (Berkowitz, 2008; Whitehouse, 1984). Therefore, their potential for dissolution in brine will be lower than that of lower-substituted alkylnaphthalenes or alkylbenzenes, which subsequently will lead to a smaller fraction of the hydrophobic alkylnaphthalenes in the bottom ice and the underlying seawater.

Poor relationship between the R_{BM} ratios and log K_{OW} and log K_H on day 77, when the ice was deteriorating, may imply that the proposed here equations predicting the AH's distribution patterns across sea ice can be applicable only for actively growing sea ice.

Table 4.3. Dependence of the 39 aromatic hydrocarbons' R_{TM} and R_{BM} ratios on their respective octanol-water partition coefficient (K_{OW}) and Henry's Law Constant (K_H) values throughout the study, as fitted with the following equation (X represents top (T) or bottom (B) ice core sections, respectively:

$$R_{XM} = b_0 + b_1 log\ K_{OW} + b_2 log\ K_H \qquad (10)$$

where insignificant regressions ($p > 0.05$) are displayed in bold, R^2 represents the coefficient of determination, and SEE corresponds to the standard error of estimate. The 95% confidence intervals for the modelled regression equation coefficients are provided in Table C5.

Ratio	Date	b_0	b_1	b_2	p-Value	R^2	SEE
R_{TM} (Temperature: 263.6–272.7 K Salinity: 0.9–14.1)	Day 15	–3.332	0.982	–4.393	$p < 0.001$	0.84	0.98
	Day 34	–9.563	1.346	–2.832	$p < 0.001$	0.94	0.60
	Day 52	–6.266	1.546	–0.620	$p < 0.001$	0.77	0.65
	Day 77	–17.014	2.360	–2.708	$p < 0.001$	0.81	0.49
R_{BM} (Temperature: 268.7–272.7 K Salinity: 1.5–9.0)	Day 15	–0.061	–0.329	–0.730	$p < 0.001$	0.78	0.18
	Day 34	–14.155	–1.574	–2.496	$p < 0.001$	0.76	0.35
	Day 52	–43.890	–1.606	–24.664	$p < 0.001$	0.91	4.54
	Day 77	**2.322**	**0.013**	**0.433**	**p = 0.706**	**0.04**	0.11

4.4.3 Evolution of the vertical migration of aromatics in the mesocosm

A general schematic showing the distribution pathways affecting alkylbenzenes and alkylnaphthalenes of crude oil encapsulated in sea ice is presented in Figure 4.7. As the ice grows, AHs can separate from the entrapped crude oil lens and become distributed between the bulk ice compartments, such as sea ice brine, air bubbles, ice interstitial surfaces, or POM, depending on their properties. This is followed by their transport to the air-ice interface, downward movement to the underlying seawater or transport along the ice layer through horizontally distributed brine channels.

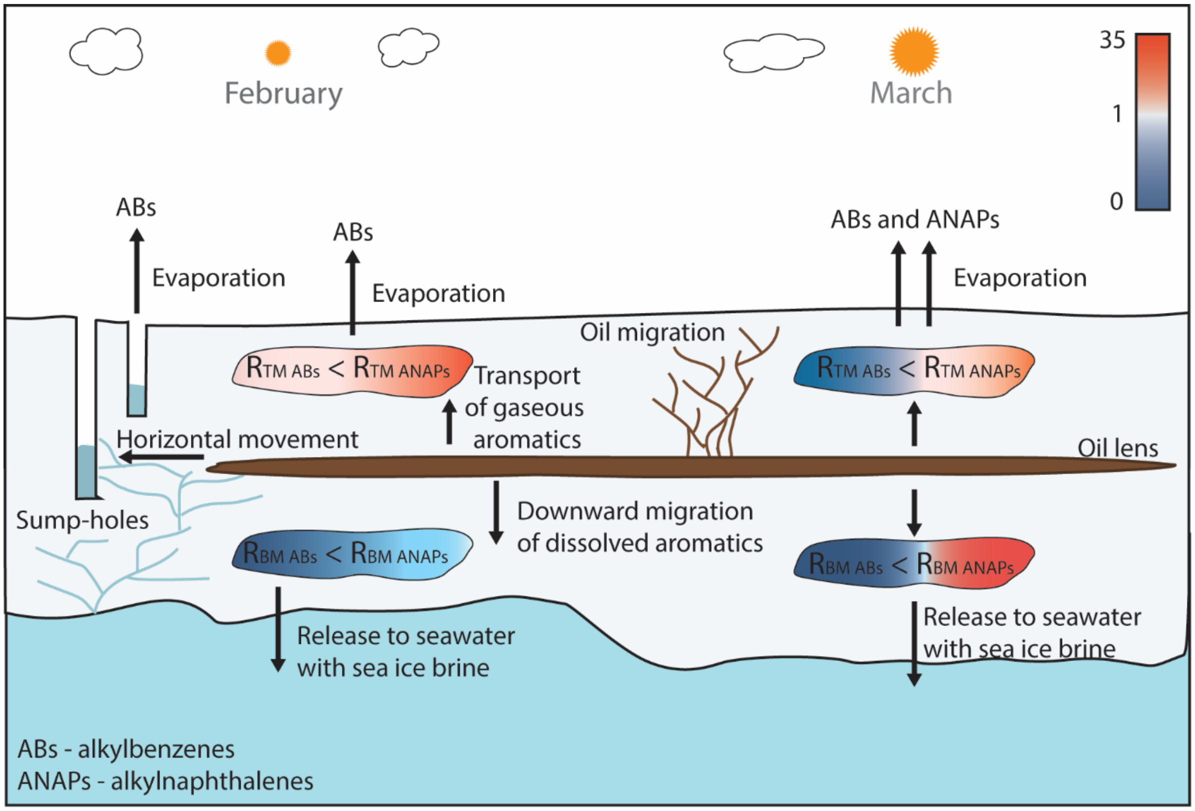

Figure 4.7. A schematic summary of the transport processes driving the distribution of crude oil alkylbenzenes and alkylnaphthalenes. R_{TM}: concentration ratio of a compound in the top ice section relative to that in the middle; R_{BM}: concentration ratio of a compound in the bottom ice section relative to that in the middle. (Blue: $R < 1$; red: $R > 1$).

With increasing ambient air temperature (Figure C3), sea ice becomes more porous (Figure 4.2c) due to the expansion of existing brine channels and generation of new brine connections in the ice (Golden et al., 2007). This facilitates more pathways for evaporative transport and contributes to the gradual depletion of alkylbenzenes in the upper ice (Figure 4.5) and in the 15-cm sump-hole (Figure 4.6). Meanwhile, alkylnaphthalenes become gradually retained in the upper ice with time, likely leading to their increased exposure for the ice-dwelling biota (Garnett et al., 2019).

Furthermore, increasing ambient air temperature contributes to the melting of the ice crystal matrix, which results in decreasing bulk ice salinity (Figure 4.2b). Since the salting-out effect decreases in lower salinity environments (Xie et al., 1997), less saline ice facilitates enhanced dissolution of alkylnaphthalenes in the brine channels. Subsequently, downward transport of dissolved alkylnaphthalenes to the water column can lead to their enrichment in the bottom-most ice depths (Figure 4.5), giving rise to the total concentration of alkylnaphthalenes close to 2.9 mg L^{-1} within 52 days of oil's residence in sea ice. Since detrimental effects on marine biota have been observed for PAH concentrations below 1 μg L^{-1} (Carls et al., 1999), the concentration value obtained in this study would be considered alarming. The leakage of water-soluble AHs through sea ice is particularly important given that the dissolved components of oil are readily bioavailable to sea ice communities, as opposed to bulk oil. Overall, in the actively growing sea ice, the fractions of alkylbenzenes and alkylnaphthalenes s in either top or bottom ice relative to those at the oil encapsulation depth (expressed as R_{TM} and R_{BM}, respectively) can be predicted from their log K_{OW} and log K_H values (Table 4.3). On the contrary, similar predictions cannot be applied to melting and deteriorating sea ice.

4.5 Conclusions

This study reports the temporal changes in the vertical distribution patterns of 39 alkylbenzenes and alkylnaphthalenes in the experimental FYI based on a crude oil-in-ice mesocosm study. Alkylbenzenes and alkylnaphthalenes originating from a crude oil lens encapsulated in a sea ice column were distributed throughout the ice through compound-specific movement processes. Specifically, alkylbenzenes tended to rapidly migrate to the air-ice interface, where they were subsequently released to the air. Therefore, they were depleted in the upper ice relative to the oil lens encapsulation depth and relative to alkylnaphthalenes. Conversely, alkylnaphthalenes in the upper ice tended to be retained and enriched relative to the oil lens depth. Moreover, due to their low potential for evaporation, they were also found to partition to sea ice brine and to migrate to the seawater-ice boundary layer in large concentrations (Σ_{ANAPs} = 2.9 mg L^{-1}). K_{OW} and K_H were assessed as good predictors of the alkylbenzene and alkylnaphthalene fractions in the top and bottom ice depths relative to the ice sections containing the oil lens (expressed as R_{TM} and R_{BM} ratios) during the ice growth period.

Supporting Information

The Supporting Information for this chapter is available in Appendix C.

References

Berkowitz, B. D., I.; Yaron, B. 2008. Contaminant partitioning in the aqueous phase. In Contaminant geochemistry; interactions and transport in the subsurface environment, 127–141. Springer Berlin Heidelberg.

Brandvik, P. J., & Faksness, L.-G. 2009. Weathering processes in Arctic oil spills; meso-scale experiments with different ice conditions. Cold Regions Science and Technology, 55: 160–166.

Carls, M. G., Rice, S. D., & Hose, J. E. 1999. Sensitivity of fish embryos to weathered crude oil: Part I. Low-level exposure during incubation causes malformations, genetic damage, and mortality in larval Pacific herring (Clupea pallasi). Environmental Toxicology and Chemistry, 18: 481–493.

Cox, G. F. N., & Weeks, W. F. 1983. Equations for Determining the Gas and Brine Volumes in Sea-Ice Samples. Journal of Glaciology, 29: 306–316.

Crabeck, O., Delille, B., Rysgaard, S., Thomas, D. N., Geilfus, N. X., Else, B., & Tison, J. L. 2014. First “in situ” determination of gas transport coefficients (D_{O2}, D_{Ar}, and D_{N2}) from bulk gas concentration measurements (O_2, N_2, Ar) in natural sea ice. Journal of Geophysical Research: Oceans, 119: 6655–6668.

Crabeck, O., Galley, R., Delille, B., Else, B., Geilfus, N.-X., Lemes, M., Des Roches, M., Francus, P., Tison, J.-L., & Rysgaard, S. 2016. Imaging air volume fraction in sea ice using non-destructive X-ray tomography. The Cryosphere, 10: 1125–1145.

Dawson, J., Pizzolato, L., Howell, S. E. L., Copland, L., & Johnston, M. E. 2018. Temporal and Spatial Patterns of Ship Traffic in the Canadian Arctic from 1990 to 2015. Arctic, 71: 15–26.

Desmond, D. S., Crabeck, O., Lemes, M., Harasyn, M. L., Mansoori, A., Saltymakova, D., Fuller, M. C., Rysgaard, S., Barber, D. G., Isleifson, D., & Stern, G. A. 2021a. Investigation into the geometry and distribution of oil inclusions in sea ice using non-destructive X-ray microtomography and its implications for remote sensing and mitigation potential. Marine Pollution Bulletin, 173: 112996.

Desmond, D. S., Saltymakova, D., Neusitzer, T. D., Firoozy, N., Isleifson, D., Barber, D. G., & Stern, G. A. 2019. Oil behavior in sea ice: Changes in chemical composition and resultant effect on sea ice dielectrics. Marine Pollution Bulletin, 142: 216–233.

Desmond, D. S., Saltymakova, D., Smith, A., Wolfe, T., Snyder, N., Polcwiartek, K., Bautista, M., Lemes, M., Hubert, C. R. J., Barber, D. G., Isleifson, D., & Stern, G. A. 2021b. Photooxidation and biodegradation potential of a light crude oil in first-year sea ice. Marine Pollution Bulletin, 165: 112154.

Faksness, L.-G., & Brandvik, P. J. 2008a. Distribution of water soluble components from Arctic marine oil spills — A combined laboratory and field study. Cold Regions Science and Technology, 54: 97–105.

Faksness, L.-G., & Brandvik, P. J. 2008b. Distribution of water soluble components from oil encapsulated in Arctic sea ice: Summary of three field seasons. Cold Regions Science and Technology, 54: 106–114.

Fingas, M. F., & Hollebone, B. P. 2003. Review of behaviour of oil in freezing environments. Marine Pollution Bulletin, 47: 333–340.

Gao, Z., Geilfus, N.-X., Saiz-Lopez, A., & Wang, F. 2022. Reproducing Arctic springtime tropospheric ozone and mercury depletion events in an outdoor mesocosm sea ice facility. Atmospheric Chemistry and Physics, 22: 1811–1824.

Gao, Z., Munson, K., & Wang, F. 2024. Temporal Evolution of Gaseous Mercury Across the Sea Ice-Seawater Interface: A Mesocosm Study. Journal of Geophysical Research: Oceans, 129: 1–13.

Garnett, J., Halsall, C., Thomas, M., Crabeck, O., France, J., Joerss, H., Ebinghaus, R., Kaiser, J., Leeson, A., & Wynn, P. M. 2021. Investigating the Uptake and Fate of Poly- and Perfluoroalkylated Substances (PFAS) in Sea Ice Using an Experimental Sea Ice Chamber. Environmental Science and Technology, 55: 9601–9608.

Garnett, J., Halsall, C., Thomas, M., France, J., Kaiser, J., Graf, C., Leeson, A., & Wynn, P. 2019. Mechanistic Insight into the Uptake and Fate of Persistent Organic Pollutants in Sea Ice. Environmental Science and Technology, 53: 6757–6764.

Golden, K. M., Ackley, S. F., & Lytle, V. I. 1998. The Percolation Phase Transition in Sea Ice. Science, 282: 2238–2241.

Golden, K. M., Eicken, H., Heaton, A. L., Miner, J., Pringle, D. J., & Zhu, J. 2007. Thermal evolution of permeability and microstructure in sea ice. Geophysical Research Letters, 34: 1–6.

Incardona, J. P., Swarts, T. L., Edmunds, R. C., Linbo, T. L., Aquilina-Beck, A., Sloan, C. A., Gardner, L. D., Block, B. A., & Scholz, N. L. 2013. Exxon Valdez to Deepwater Horizon: Comparable toxicity of both crude oils to fish early life stages. Aquatic Toxicology, 142-143: 303–316.

Johnson, W., Idowu, I., Francisco, O., Marvin, C., Thomas, P. J., Stetefeld, J., & Tomy, G. T. 2018. Enumeration of the constitutional isomers of environmentally relevant substituted polycyclic aromatic compounds. Chemosphere, 202: 9–16.

Kwok, R., & Cunningham, G. F. 2008. ICESat over Arctic sea ice: Estimation of snow depth and ice thickness. Journal of Geophysical Research. Oceans, 113: 1–17.

Liyana-Arachchi, T. P., Valsaraj, K. T., & Hung, F. R. 2012. Ice Growth from Supercooled Aqueous Solutions of Benzene, Naphthalene, and Phenanthrene. The Journal of Physical Chemistry A, 116: 8539–8546.

Notz, D., & Worster, M. G. 2009. Desalination processes of sea ice revisited. Journal of Geophysical Research, 114: 1–10.

Oggier, M., Eicken, H., Wilkinson, J., Petrich, C., & O'Sadnick, M. 2020. Crude oil migration in sea-ice: Laboratory studies of constraints on oil mobilization and seasonal evolution. Cold Regions Science and Technology, 174: 1–16.

Oliver-Pozo, C., Aparicio-Ruiz, R., Romero, I., & García-González, D. L. 2015. Analysis of Volatile Markers for Virgin Olive Oil Aroma Defects by SPME-GC/FID: Possible Sources of Incorrect Data. Journal of Agricultural and Food Chemistry, 63: 10477–10483.

Orazbayeva, D., Kenessov, B., Koziel, J. A., Nassyrova, D., & Lyabukhova, N. V. 2017. Quantification of BTEX in Soil by Headspace SPME–GC–MS Using Combined Standard Addition and Internal Standard Calibration. Chromatographia, 80: 1249–1256.

Payne, J. R., Hachmeister, L. E., McNabb, G. D., Sharpe, H. E., Smith, G. S., & Menen, C. A. 1991a. Brine-induced advection of dissolved aromatic hydrocarbons to Arctic bottom waters. Environmental Science and Technology, 25: 940–951.

Payne, J. R., McNabb Jr, G. D., & Clayton. Jr, J. R. 1991b. Oil-weathering behavior in Arctic environments. Polar Research, 10: 631–662.

Petrich, C., Karlsson, J., & Eicken, H. 2013. Porosity of growing sea ice and potential for oil entrainment. Cold Regions Science and Technology, 87: 27–32.

Polcwiartek, K., Stern, G. A., & Wang, F. 2025. Incorporation and Distribution of Polycyclic Aromatic Hydrocarbons in Experimental Sea-Ice. Environmental Science and Technology, 59: 7310–7319.

Riazi, M. R., & Edalat, M. 1996. Prediction of the rate of oil removal from seawater by evaporation and dissolution. Journal of Petroleum Science and Engineering, 16: 291–300.

Saltymakova, D., Desmond, D. S., Galley, R., Polcwiartek, K., Neusitzer, T. D., Firoozy, N., Barber, D. G., & Stern, G. A. 2024. The influence of sea-ice conditions on crude oil spill behaviour. Cold Regions Science and Technology, 221: 104160.

Saltymakova, D., Desmond, D. S., Isleifson, D., Firoozy, N., Neusitzer, T. D., Xu, Z., Lemes, M., Barber, D. G., & Stern, G. A. 2020. Effect of dissolution, evaporation, and photooxidation on crude oil chemical composition, dielectric properties and its radar signature in the Arctic environment. Marine Pollution Bulletin, 151: 110629.

Saltymakova, D., Desmond, D. S., Smith, A. F., Bautista, M. A., Collins, E., Polcwiartek, K., Snyder, N., Wolfe, T., Hubert, C., Isleifson, D., & Stern, G. 2025. Enhanced crude oil degradation observed in sea ice following bioaugmentation with arctic bacteria. Marine Environmental Research, 204: 106942.

Simmonds, I. 2015. Comparing and contrasting the behaviour of Arctic and Antarctic sea ice over the 35 year period 1979-2013. Annals of Glaciology, 56: 18–28.

Spaulding, M. L. 1988. A state-of-the-art review of oil spill trajectory and fate modeling. Oil & chemical pollution, 4: 39–55.

Ucan-Marin, F., & Dupuis, A. 2015. A literature review on the aquatic toxicology of petroleum oil: An overview of oil properties and effects to aquatic biota. Canadian Science Advisory Secretariat (CSAS), 007, 52.

Wang, F., Pućko, M., & Stern, G. 2017. Transport and transformation of contaminants in sea ice. In Sea Ice, 472–491.

Wang, Z. D., Fingas, M., Landriault, M., Sigouin, L., & Xu, N. N. 1995. Identification of Alkylbenzenes and Direct Determination of BTEX and (BTEX + C3-Benzenes) in Oils by GC/MS. Analytical Chemistry, 67: 3491–3500.

Whitehouse, B. G. 1984. The effects of temperature and salinity on the aqueous solubility of polynuclear aromatic hydrocarbons. Marine Chemistry, 14: 319–332.

Xie, W.-H., Shiu, W.-Y., & Mackay, D. 1997. A review of the effect of salts on the solubility of organic compounds in seawater. Marine Environmental Research, 44: 429–444.

Chapter 5 Conclusion

5.1 Summary of Research Findings and Scientific Contributions

The Arctic is undergoing substantial environmental and industrial changes, making the region more susceptible to oil spills. With the elevated threat of uncontrolled hydrocarbon release in the Arctic Ocean, there is an increasing need for in-depth knowledge of the fate and behaviour of toxic aromatic fractions of oil in this ecologically and culturally sensitive and vulnerable region.

Overall, this thesis provides new and in-depth insights into the understanding of the temporal and spatial distribution behaviour of aromatic hydrocarbons in the dynamic sea ice environment. The findings of this thesis point to the role of physicochemical properties of aromatic hydrocarbons on their partitioning behaviour in the multiphase sea ice environment, and, subsequently, on their transport pathways within sea ice and across the seawater-ice-atmosphere interface. These findings result from three interrelated and logically-connected microcosm and mesocosm studies (Chapters 2 to 4) specifically designed to fill critical knowledge gaps related to partitioning and transport pathways of petrogenic aromatic hydrocarbons in the sea ice environment. The major conclusions from addressing each of the proposed hypotheses (see Chapter 1), along with key contributions to the research area, are summarized below:

a) Polycyclic aromatic hydrocarbons of varying physicochemical properties interact with sea ice-associated particulate organic matter to different extents;

As indicated by the results reported in Chapter 2, PAHs of greater molecular weights, such as benzo(a)pyrene, were present in the particulate fractions at higher concentrations than LMW counterparts, such as naphthalene. With warming temperatures and decreasing salinity of sea ice, the concentrations of three- to five-ring PAHs in the particle-associated fractions in sea ice significantly increased over time, whereas particle-associated concentrations of two-ring naphthalene remained unchanged. Accumulation of higher-molecular-weight PAHs in sea ice with time and their retention during the ice growth period can contribute to their prolonged exposure and chronic adverse effects on local sea ice biota. Furthermore, the distribution of the MMW PAHs (e.g., phenanthrene, pyrene) between the aqueous phase and organic particles in sea ice was reasonably well explained by evolving temperature and salinity. Meanwhile, partitioning behaviours of highly volatile (e.g., naphthalene) and highly particle-reactive PAHs (e.g., benzo(a)pyrene) were found to be weakly correlated with changing temperature and salinity. Overall, the combined effect of temperature and salinity on the particle-aqueous phase partitioning of PAHs in freezing seawater and sea ice is more complex than that at above-water-freezing temperatures. This, in turn, implies that the thermodynamic equilibrium-based models that are commonly used in predicting a contaminant's environmental transport and behaviour are of limited applicability in cold environments and need to be revised.

b) Aromatic hydrocarbons of varying physicochemical properties in oils encapsulated in sea ice are distributed across the seawater-ice-atmosphere interface through different mechanisms;

The findings reported in Chapters 3 and 4 demonstrate that petrogenic aromatic hydrocarbons were distributed across the seawater-ice-atmosphere interface from an oil (crude oil or diesel fuel) lens encapsulated within a growing ice cover through different transport pathways. Specifically, volatile monoaromatic hydrocarbons (e.g., BTEX compounds) preferentially partitioned to air inclusions in sea ice and were subsequently transported to the air-ice interface through air bubble dynamics, resulting in their evaporation to the air in larger proportions than their less volatile counterparts. Conversely, LMW PAHs (e.g., alkylnaphthalenes) exhibiting greater potential for liquid phases (e.g., brine) preferentially dissolved in sea ice brine and were subsequently transported to the bottom ice and the underlying seawater *via* brine drainage, where they comprised the largest fraction among the studied aromatic hydrocarbons. Finally, MMW and HMW PAHs (e.g., phenanthrene, pyrene and their alkylated homologues) were found to be predominant in the ice sections containing bulk oil, resulting from their hydrophobic properties and lesser mobility in the sea ice environment. Furthermore, based on the multiple linear regression equations presented in Chapters 3 and 4, it can be concluded that the distributions of aromatic hydrocarbons of diesel and crude oil within the ice and across the seawater-ice-atmosphere interface are primarily driven by their physicochemical properties, in particular their octanol-water partition coefficient and

Henry's Law Constant. Therefore, the respective upward and downward distributions of aromatic hydrocarbons can be predicted with reasonable certainty from these parameters.

The progressive transport of AHs in oil-in-ice spills, especially atmospheric loss of volatile oil components, has implications for oil spill clean-up strategies, in particular *in-situ* burning. Specifically, ISB relies on the vaporization of volatile oil constituents and is more effective for fuel products characterized by a greater content of volatile hydrocarbons. Therefore, a substantial atmospheric loss of the most volatile oil components may hinder the applicability of oil ISB in the environment. Furthermore, the fractionation of oil constituents in sea ice and their subsequent removal to the overlying atmosphere and/or underlying seawater alter the chemical and spectral fingerprints of the spilled product. The latter refers to the unique absorption and reflection characteristics of a specific petroleum product, which are key features that remote sensing-based oil monitoring and detection technologies rely on. Thus, compound-specific transport processes affecting the chemical composition of a spilled oil further impact the applicability and effectiveness of oil spill detection and monitoring technologies. Finally, continuous downward seepage of water-soluble aromatic hydrocarbons down the ice cover, followed by their release to the water column, pose hazard to local sea ice and seawater organisms.

c) The type of spilled petroleum product (crude oil *vs* diesel fuel) does not impact the distribution patterns of individual aromatic hydrocarbons in an oil-in-ice spill scenario.

Based on the results reported in Chapters 3 and 4, the respective individual aromatic hydrocarbons originating from either diesel fuel (Chapter 3) or crude oil (Chapter 4) lens encapsulated in the growing experimental sea ice followed the same distribution behaviours and transport pathways in the microcosms and mesocosm. Specifically, the multiple linear regression models derived in Chapters 3 and 4 indicate that the respective upward and downward distributions of the studied aromatic hydrocarbons from their original injection location were influenced by their respective K_{OW} and K_H in the same way, regardless of the used oil product, varying timelines of the studies, and the differing sizes of the microcosms *vs* the mesocosm. This emphasizes the role of the physicochemical properties of aromatic hydrocarbons in their distribution in sea ice-covered environments.

Overall, this thesis contributes to our better appreciation of the mechanisms and transport pathways of aromatic hydrocarbons in sea ice infested with petroleum oil. My thesis also delivers datasets that will benefit the re-evaluation, advancement and development of oil spill weathering and toxicity assessment models, therefore aiding in the development of a suitable oil spill response strategy in ice-covered Arctic waters. Lastly, this study validates the use of novel sea ice microcosm and mesocosm approaches to the study of the behaviour of petrogenic aromatic hydrocarbons and oil spills in the sea ice environment.

5.2 Challenges and Future Directions

While the findings in this thesis serve as a valuable contribution to our current knowledge of oil spills in ice-covered waters, this study also recognizes the challenges encountered during the experimental part of this thesis. Here, we point to improvements that could address some of these limitations and indicate future research directions in order to enhance our understanding of petrogenic aromatic hydrocarbon behaviour in the sea ice environment.

One of the biggest limitations of this research is the lack of direct measurements of volatile aromatic hydrocarbon concentrations in the air just above the microcosms (Chapters 2 and 3) and mesocosm (Chapter 4). Potential losses of the aromatic hydrocarbons were assessed based on the difference between the injected and detected masses of the monitored compounds. However, it would be more desirable for the loss to the air to be characterized better than is currently the case.

Moreover, the transformation of aromatic hydrocarbons in sea ice or sub-ice seawater, such as microbial degradation, was deemed to play a negligible role in the overall mass balance of the studied compounds. However, since past studies in the field demonstrated a potential for aromatic hydrocarbons to be affected by biodegradation and photooxidation in natural sea ice environments (Garneau et al., 2016; Vergeynst et al., 2019), future research should acknowledge the effects of these processes on the fate of aromatic oil fractions.

Another substantial limitation of the experiments presented in Chapters 2 to 4 is the unusual design of the microcosm containers and the mesocosm tub. Specifically, the small size of the micro- and mesocosm, as well as the funnel-like shape of the microcosms, led to more rapid heat loss in the seawater and growing sea ice, resulting in substantially altered ice growth rate, geophysical properties of the ice, and the underlying seawater compared to natural conditions.

Furthermore, large heterogeneity of sea ice on both a spatial and temporal scale presents a unique challenge in studying the behaviour of oil spills and oil-related chemicals in the sea ice environment. This is reflected in the high heterogeneity of lateral and vertical oil transport, giving rise to uneven distribution within the growing sea ice medium. As a result, collected ice samples can vary considerably in their hydrocarbon content.

Limitations pertaining to the sample preparation and analytical challenges identified throughout this study include: 1) a probability of PAH repartitioning between the dissolved and particulate phases during the sample collection, melting and filtration steps (Chapter 2), implying that the determined K_d values should be interpreted with some caution; 2) multiple-step sample processing protocols accompanied by low recovery values for the volatile compounds (e.g., alkylbenzenes, alkylnaphthalenes; Chapters 2 and 3) potentially contributing to possible inaccuracies in the results of compound mass balance calculations; 3) lastly, a lack of sample replicates for each of the ice core sections (due to an oversight in the sampling protocol), and small size of headspace samples (~10 mL) collected throughout the experiment reported in Chapter 4 may have contributed to the limited representativeness of the small-sized headspace samples for the entire sea ice core sections As such, the development and improvement of sample processing protocols and sample analysis techniques eliminating these challenges, while still providing simplicity and reliability, is highly recommended.

In this thesis research, I did not aim to recreate or mimic natural environments, but rather, my goal was to probe the fundamental mechanisms and processes driving the distribution behaviour of aromatic hydrocarbons in the sea ice environment in partially controlled experimental studies. While the main advantage of small-scale experiments is the ability to study isolated processes that cannot always be investigated in real-world conditions, a question arises whether, and to what extent, the findings retrieved from those studies can be translated to the natural Arctic environment. Since we demonstrated that the distribution of aromatic hydrocarbons within and out of the ice was driven largely by their physicochemical properties, we conclude that the overall distribution patterns exhibited by the studied aromatic hydrocarbons would likely apply to natural environments as well. Meanwhile, the rate and extent of their transport and dynamics are more likely to be scenario-specific and should therefore be extrapolated to the real world with caution.

Having said that, such small-scale studies involving artificial seawater would be more representative of natural environments and tremendously improved by the employment of the larger outdoor pools (30 ft by 30 ft by 10 ft deep, each pool; two pools in total) such as the ones available at the Ocean-Sea Ice Mesocosm Facility (OSIM) located at the recently opened, highly innovative and multidisciplinary research facility, The Churchill Marine Observatory (CMO). Sea ice forming and growing from natural seawater drawn directly from the Churchill estuary in such a large-scale mesocosm facility would more accurately represent natural conditions.

Ultimately, the OSIM facility is well-suited to carry out future studies investigating the transport and fate of petrogenic aromatic hydrocarbons originating from different petroleum products throughout the whole sea ice growth-melt cycle and under various environmental conditions, such as freshwater *vs* seawater, turbulent *vs* quiescent, very low temperatures *vs* just below freezing, and different types of organic particulate matter. Results delivered by such postulated comprehensive studies would provide substantial insights into a better understanding of oil and transport-related aromatic hydrocarbon distribution mechanisms under differing circumstances. This is of particular importance in dynamically changing environments, such as marine Arctic waters. Additionally, microorganisms naturally occurring in the local seawater would also be incorporated, so that the interplay between transport and transformation processes of aromatic hydrocarbons could be understood better than is currently the case. Those determinations would be of enormous benefit in terms of the validation and improvement of existing modelling studies.

References

Garneau, M.-È., Michel, C., Meisterhans, G., Fortin, N., King, T. L., Greer, C. W., & Lee, K. 2016. Hydrocarbon biodegradation by Arctic sea-ice and sub-ice microbial communities during microcosm experiments, Northwest Passage (Nunavut, Canada). FEMS Microbiology Ecology, 92: 1–18.

Vergeynst, L., Christensen, J. H., Kjeldsen, K. U., Meire, L., Boone, W., Malmquist, L. M. V., & Rysgaard, S. 2019. In situ biodegradation, photooxidation and dissolution of petroleum compounds in Arctic seawater and sea ice. Water Research (Oxford), 148: 459–468.

Appendix A

Supporting information for Chapter 2

Table of Contents

Figure A5. Relationship between the bulk salinity of sea ice and the total concentrations of the PAHs in young experimental sea ice on day 2.

Text A1. Solid-phase extraction and ultrasonication procedures

Liquid fractions obtained upon filtration were loaded onto SPE cartridges (Sep-Pak C18, 3cc, 500 mg sorbent, Waters) pre-conditioned with methanol (Thermo Scientific) and equilibrated with a 40% aqueous solution of methanol. Following the sample loading step, the cartridges were rinsed with MQ water and dried with N_2. The 4 PAH compounds were eluted off the cartridge using 5 mL of hexane (Thermo Scientific). The extracts were evaporated to 0.5 mL using a rotary evaporator, then solvent-exchanged to 1 mL of iso-octane (Thermo Scientific).

Following the filtration, the glass microfiber filters were placed into 20 mL amber glass vials and stored in a fridge at 4 °C. Sample extraction was done using 15 mL of dichloromethane (Thermo Scientific) and subsequent ultra-sonification of the vials was conducted in an ultrasonicating bath (Branson 1800) for 30 min. Solvents from the vials were filtered through 0.45 µm PTFE membrane syringe filters to separate extracts with accommodated PAHs and the GF/F filter residue. Next, the extracts were concentrated to 0.5 mL and solvent-exchanged to 1 mL of iso-octane. The extracts resulting from both SPE and ultra-sonification were stored in a freezer at –20 °C until the analysis.

Text A2. Instrumental method details

The GC-MS/MS was operated in the SIM mode. A sample volume of 1 µL was injected in splitless mode. The electron ionization energy was 70 eV. The oven regime was set as follows: 40 °C (1 min hold), 30 °C min^{-1} to 140 °C, 5 °C min^{-1} to 180 °C, and then 10 °C min^{-1} to 320 °C with a 10 min hold.

Text A3. Quality control

Seawater (1 L; n = 2) was collected from each experimental microcosm on February 24, before the injection of humic acid and PAHs, to determine background concentrations of particles and PAHs in the artificial seawater. The four PAHs were not detected in the seawater, and the average concentration of background particles was 0.7 ± 0.2 mg L^{-1}. Seawater and bulk ice samples were also retrieved from the control microcosm to monitor background concentrations of PAHs (n = 3 each for water and ice) and particles (n = 3 each for water and ice). Background pyrene concentration in the bulk ice blanks was 0.8 ± 0.2 ng L^{-1}, whereas the remaining PAHs were not detected in either control seawater or sea-ice. The background particle concentrations in the control seawater and ice were 0.6 ± 0.3 mg L^{-1} and 0.9 ± 0.4 mg L^{-1}, respectively. Field blanks (1 L of Milli-Q water; n = 4; and 1 L of artificial seawater from the main SERF pool; n = 3) and laboratory blanks (1 L of MQ water; n = 14) were collected throughout the sampling events and sample processing, respectively, to assess potential contamination. The concentrations of PAHs in the field and laboratory blanks ranged from 1.1 to 1.5 ng L^{-1} and from 0.6 to 1.3 ng L^{-1}, respectively (see Table A4). The particles in the corresponding blanks were not detected. Blank samples were processed following the same protocols as the regular samples.

The recoveries of the SPE and ultrasonification extraction of PAHs were monitored by the surrogated mixture of deuterated PAHs added prior to the extraction. The recoveries of deuterated standards reached 24, 67, 75 and 91% for NAP-D_8, PHE-D_{10}, PYR-D_{10} and BaPYR-D_{12}, respectively for the liquid fractions, whereas the recoveries for the particulate fractions reached 77, 87, 95 and 101% for the corresponding compounds, respectively (Table A5). Since the recovery values for the respective deuterated PAHs were consistent within the population of samples, the recoveries are assessed acceptable. Low recoveries observed for naphthalene could be attributed to its high volatility.

Reported concentrations of all compounds were recovery corrected. Pre-concentrated extracts were also spiked with 2-fluorobiphenyl (Restek) as a recovery standard to compensate for variances in the final extract volume and injection volume.

The external calibration curves for each compound contained at least 10 concentrations and exhibited R^2 values higher than 0.99. The MDLs, calculated based on U.S.EPA (2016), ranged from 0.9 to 2.1 ng L^{-1} (Table A5).

Text A4. Brine dynamics in sea ice

Movement of liquids (brine) in sea ice can occur through brine rejection, convective drainage, flushing, as well as upward migration to the snow (Notz and Worster, 2009; Petrich and Eicken, 2017; Wang et al., 2017). During ice formation and growth, salts are rejected from the ice matrix to the underlying seawater due to size restrictions throughout a process of brine rejection (freeze rejection). On the other hand, convective drainage occurs when more concentrated and denser brine in the ice is replaced with the adjacent less saline seawater at the base of the ice. Brine flushing is a gravity-mediated process and is a result of surface ice melt or the presence of snow. In addition, brine can also migrate upwards through the ice to the overlying snow.

Table A1. Physicochemical properties of the four studied PAHs at freezing temperatures.

PAH	Molecular weight (g mol^{-1})	Vapour pressure @ –12 °C (µBar)	Solubility @ –2.4 °C (g L^{-1})		log K_{OW} (–12 °C)
			Freshwater^{b}	Seawater (S = 35)^{c}	
Naphthalene	128.2	101.0^{a}	1.7×10^{-1}	1.2×10^{-1}	3.3^{c}
Phenanthrene	178.2	0.40^{a}	1.7×10^{-2}	1.1×10^{-2}	4.4^{c}
Pyrene	202.3	0.06^{a}	6.4×10^{-3}	4.1×10^{-3}	4.9^{d*}
Benzo[a]pyrene	252.3	1.20^{a}	1.2×10^{-3}	7.0×10^{-4}	5.7^{d*}

* Values at 0 °C

[b] (Saltymakova et al., 2020)

[c] (Desmond et al., 2021)

[d] (Meyer et al., 2006)

Table A2. Filtration recoveries.

PAH	Representative surrogate	Recovery (%) (n = 6)
Naphthalene (NAP)	NAP-D$_8$	73 ± 15
Phenanthrene (PHE)	PHE-D$_{10}$	87 ± 8
Pyrene (PYR)	PYR-D$_{10}$	84 ± 11
Benzo(a)pyrene (BaPYR)	BaPYR-D$_{12}$	91 ± 13

Table A3. Ions targeted during the GC-MS analysis with the SIM mode.

Compound	Qualifier	Quantifier 1	Quantifier 2
Naphthalene	128	108	102
Naphthalene-D$_8$	136	137	134
2-Fluorobiphenyl	172	152	170
Phenanthrene	178	176	152
Phenanthrene-D$_{10}$	188	184	160
Pyrene	202	200	101
Pyrene-D$_{10}$	212	208	106
Benzo(a)pyrene	252	250	126
Benzo(a)pyrene-D$_{12}$	264	260	

Table A4. Background concentrations of PAHs and particles in the microcosms and blanks.

Parameter	NAP (ng L^{-1})	PHE (ng L^{-1})	PYR (ng L^{-1})	BaPYR (ng L^{-1})	Background particles (mg L^{-1})
Experimental seawater	n/d	n/d	n/d	n/d	0.7 ± 0.2
blanks (n = 10)	n/d	n/d	n/d	n/d	0.6 ± 0.3
Control seawater blanks (n = 3)	n/d	n/d	0.8 ± 0.2	n/d	0.9 ± 0.4
Control ice blanks (n = 3)					
Field blanks	n/d	1.1 ± 0.2	1.5 ± 1.1	1.4 ± 0.1	n/d
Laboratory blanks (n = 14)	0.6 ± 0.4	0.7 ± 0.2	1.1 ± 0.2	1.3 ± 0.5	n/d

n/d: not detected

Table A5. Solid-phase extraction and ultra-sonication recoveries and method detection limits.

Parameter	NAP	PHE	PYR	BaPYR
Solid-phase extraction/liquid recovery (%)	24 ± 7%	67 ± 7%	75 ± 9%	91 ± 11%
Ultrasonication/particulate recovery (%)	77 ± 14%	87 ± 13%	95 ± 9%	101 ± 8%
Method Detection Limit (ng L^{-1})	0.9	1.1	1.2	2.1

Table A6. Mean and standard deviations (n = 3) total masses of the four PAHs in the microcosms throughout the experiment. Day 0 corresponds to the day of PAH mixture injection.

Day	NAP (μg)	PHE (μg)	PYR (μg)	BaPYR (μg)
0	511	505	498	506
2	460 ± 11	501 ± 8	495 ± 10	502 ± 6
5	419 ± 22	497 ± 25	490 ± 26	504 ± 11
9	360 ± 15	468 ± 20	489 ± 24	501 ± 11
14	288 ± 14	449 ± 18	484 ± 24	499 ± 13
19	213 ± 9	417 ± 17	474 ± 12	501 ± 10

Table A7. Mean apparent distribution coefficients (log K_d) and standard deviations for the four PAHs in the ice and the seawater media over time.

	Sea Ice				Seawater			
Day	NAP	PHE	PYR	BaPYR	NAP	PHE	PYR	BaPYR
2	3.8 ± 0.3	3.7 ± 0.1	5.1 ± 0.1	5.8 ± 0.2	2.3 ± 0.0	3.4 ± 0.2	4.6 ± 0.1	6.2 ± 0.1
5	3.9 ± 0.1	4.8 ± 0.3	5.4 ± 0.2	6.3 ± 0.1	2.2 ± 0.1	4.4 ±0.2	4.5 ± 0.1	5.7 ± 0.0
9	3.9 ± 0.2	4.7 ± 0.3	5.5 ± 0.1	6.3 ± 0.1	2.3 ± 0.1	4.8 ± 0.1	5.0 ± 0.0	6.0 ± 0.1
14	4.1 ± 0.1	4.9 ± 0.3	6.2 ± 0.1	6.5 ± 0.1	2.4 ± 0.1	3.5 ± 0.1	4.0 ± 0.0	4.8 ± 0.1
19	4.5 ± 0.0	5.7 ± 0.1	6.3 ± 0.0	6.7 ± 0.1	2.4 ± 0.1	3.9 ± 0.2	4.5 ± 0.0	5.2 ± 0.4

Table A8. Average ice thickness and ice growth rate throughout the experiment.

	Ice formation (February 24)	Day 0	Day 2	Day 5	Day 9	Day 14	Day 19
Average ice thickness (cm)	0	8.0	12.5	14.3	14.8	17.3	19.3
Average ice growth rate (cm day^{-1})	0	4.0	2.3	0.6	0.1	0.5	0.4

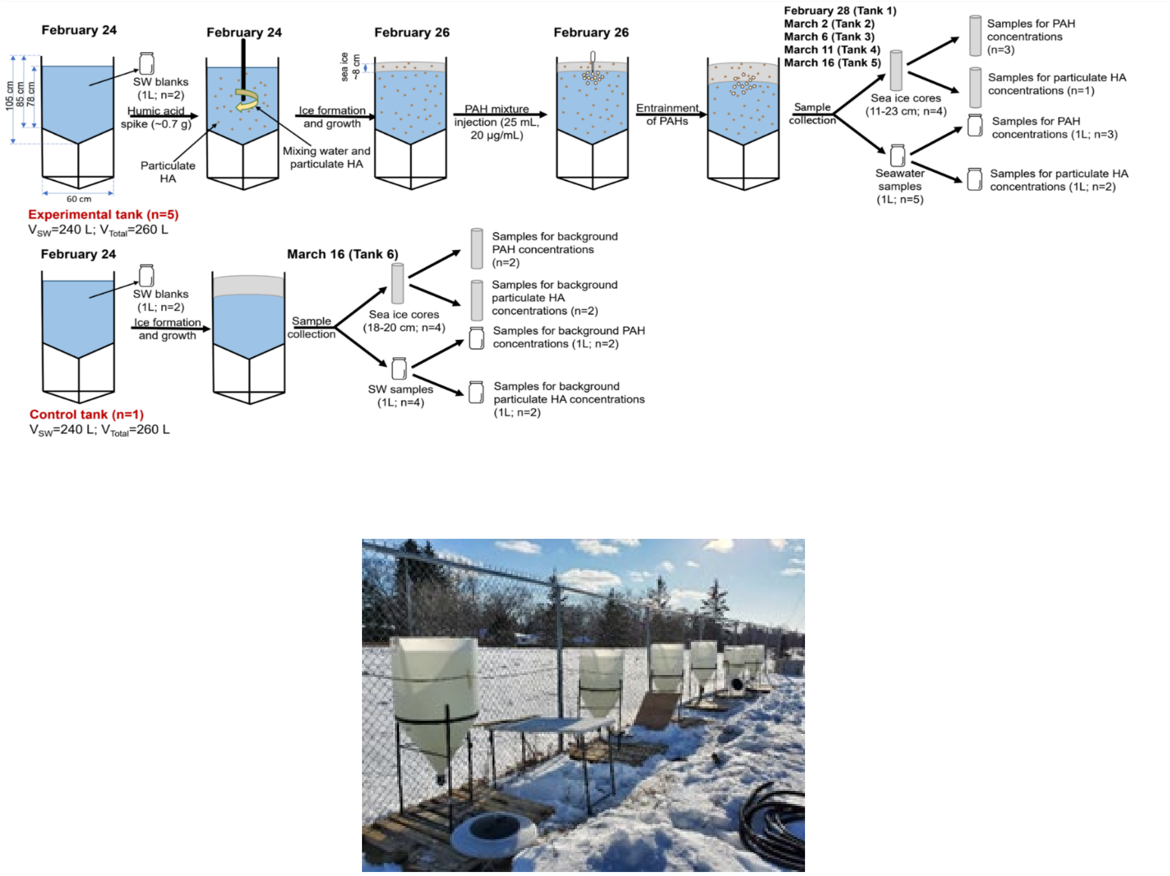

Figure A1. Schematic of the experimental design, key steps of the study, and sample collection plan (upper panel), and a picture of the microcosm set-up (lower panel).

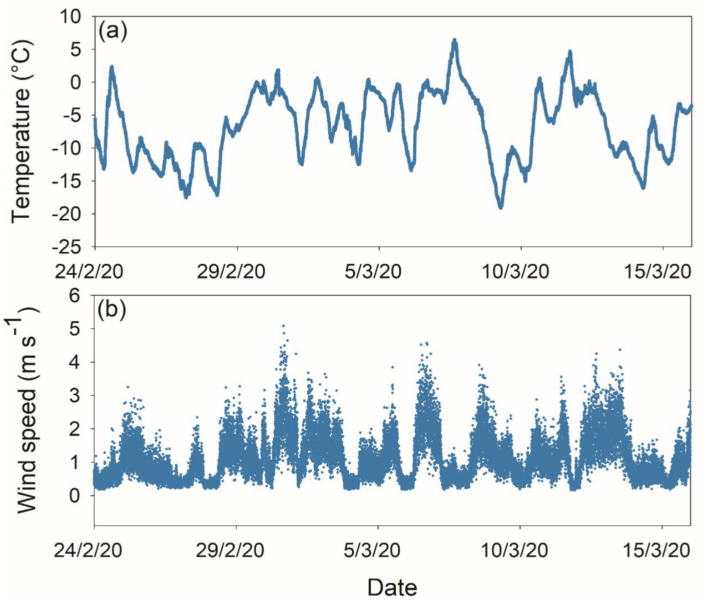

Figure A2. Variabilities of the in-situ a) ambient air temperature and b) wind speed during the experiment, as measured at 1.5 m above the ground.

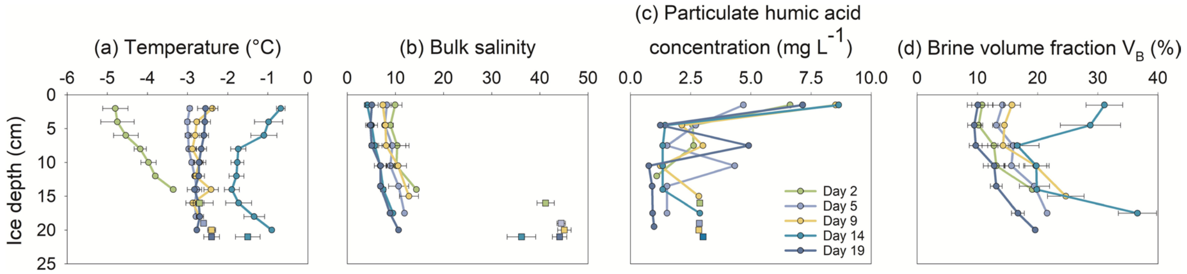

Figure A3. Vertical profiles of (a) temperature, (b) bulk salinity, (c) concentration of particulate humic acid, and (d) brine volume fraction across the bulk ice (circle symbols) and in the water column (square symbols) in the experimental microcosms at various days after the addition of particulate humic acid and PAHs. The uppermost point on the y-axis corresponds to the atmosphere-ice interface. Note that the particulate humic acid concentration in seawater on day 14 overlaps with that of day 19.

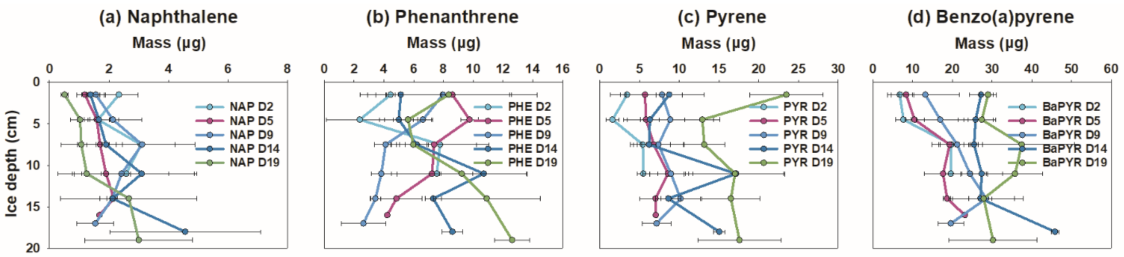

Figure A4. Vertical profiles of the respective PAHs in the ice column throughout the experiment.

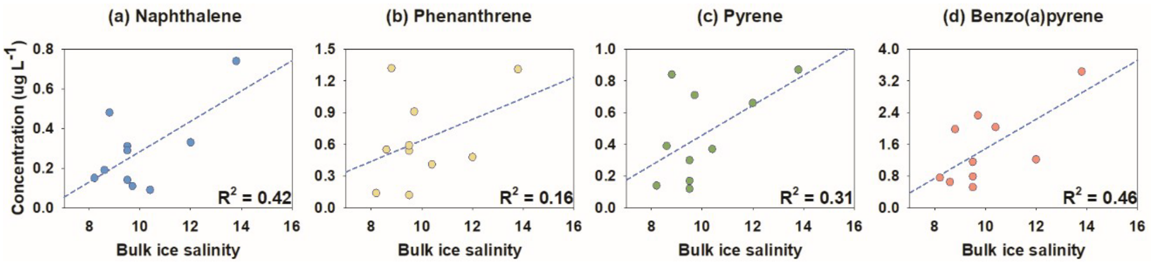

Figure A5. Relationship between the bulk salinity of sea ice and the total concentrations of the PAHs in young experimental sea ice on day 2.

References:

Desmond, D. S., Saltymakova, D., Smith, A., Wolfe, T., Snyder, N., Polcwiartek, K., Bautista, M., Lemes, M., Hubert, C. R. J., Barber, D. G., Isleifson, D., & Stern, G. A. 2021. Photooxidation and biodegradation potential of a light crude oil in first-year sea ice. Marine Pollution Bulletin, 165: 112154.

Meyer, T., Lei, Y. D., & Wania, F. 2006. Measuring the Release of Organic Contaminants from Melting Snow under Controlled Conditions. Environmental Science and Technology, 40: 3320–3326.

Notz, D., & Worster, M. G. 2009. Desalination processes of sea ice revisited. Journal of Geophysical Research, 114: 1–10.

Petrich, C., & Eicken, H. 2017. Overview of sea ice growth and properties. In Sea Ice, 1–41.

Saltymakova, D., Desmond, D. S., Isleifson, D., Firoozy, N., Neusitzer, T. D., Xu, Z., Lemes, M., Barber, D. G., & Stern, G. A. 2020. Effect of dissolution, evaporation, and photooxidation on crude oil chemical composition, dielectric properties and its radar signature in the Arctic environment. Marine Pollution Bulletin, 151: 110629.

Wang, F., Pućko, M., & Stern, G. 2017. Transport and transformation of contaminants in sea ice. In Sea Ice, 472–491.

Appendix B

Supporting information for Chapter 3

Table of Contents

Text B1. Solid-phase extraction and liquid-liquid extraction procedures.

Table B1. Solid-phase extraction (SPE) and liquid-liquid extraction (LLE) recoveries (rec.) for Naphthalene-D_8 (NAP-D_8), Acenaphthylene-D_8 (ACY-D_8), Acenaphthene-D_{10} (ACE-D_{10}), Fluorene-D_{10} (FLE-D_{10}), Phenanthrene-D_{10} (PHE-D_{10}), and Pyrene-D_{10} (PYR-D_{10}).

Table B2. List of the identified compounds, representative surrogates, ions targeted during the GC-MS analysis and Method Detection Limits.

Table B3. Background concentrations of aromatics (ng L^{-1}) in the microcosms and blanks.

Table B4. List of identified compounds and their quantitative structure-activity relationship (QSAR)-estimated physicochemical properties at 25 °C and salinity of freshwater.

Table B5. Average sea ice thickness and ice growth rate during the experiment.

Table B6. Mean and standard deviations (n = 4) total volume of diesel fuel and mass of total aromatics (m_{TArom}) mass in the microcosms throughout the study. Day 0 represents the day of diesel injection.

Table B7. 95% confidence intervals (CI) for the multiple linear regression coefficients determined for the equations predicting the relative fractions of the 46 aromatic hydrocarbons from their respective octanol-water partition coefficient (K_{OW}) and Henry's Law Constant (K_H) values.

Figure B1. Schematic of the experimental design, key steps of the study and sample collection protocol.

Figure B2. Variabilities of the ambient air temperature retrieved from the Winnipeg International Airport meteorological station (a) and *in situ* wind speed throughout the experiment (b), as measured at 1.5 m above the ground.

Figure B3. Vertical profiles of temperature (a), bulk salinity (b), and brine volume fraction (c) throughout the sea ice column (circle symbols) and in the underlying seawater (square symbols) in the control microcosm. The value of 0 on the y-axis corresponds to the air-ice interface.

Figure B4. Vertical distribution profiles of 1,3-diethylbenzene (a), 1,2-dimethylnaphthalene (b), Phenanthrene (c) and 2-methylpyrene (d) in the ice throughout the study. Relative % values of each compound were estimated relative to the initial amounts of each compound on day 0.

Figure B5. Chemical composition profile of the studied aromatic hydrocarbons in fresh diesel fuel.

Text B1. Solid-phase extraction and liquid-liquid extraction procedures.

Seawater samples were loaded onto SPE cartridges (Sep-Pak C18, 35 cc, 10 g sorbent, Waters) pre-conditioned with methanol (Fisher Chemical, Optima Grade) and equilibrated with a 40% aqueous solution of methanol. Then, the cartridges were rinsed with Milli-Q water and dried with N_2. The AHs were eluted from the cartridges with two portions of 10 mL of hexane (Fisher Chemical, Optima Grade) and followed by two portions of 10 mL of dichloromethane (Thermo Scientific). The collected extracts were concentrated down using a rotary evaporator and solvent-exchanged to 1 mL of iso-octane (Thermo Scientific).

LLE extraction of melted sea ice samples was performed using 1 L separatory funnels. Each sample was treated with a minimum of three 50 mL portions of hexane (Thermo Scientific/Fisher Chemical) followed by three 50 mL portions of dichloromethane (Fisher Chemical) or until the aqueous fraction was completely clear/colourless. The collected extracts were evaporated using a rotary evaporator. The extracts resulting from both SPE and LLE were stored in a freezer at –20 °C until the analysis.

The sample extracts that contained visible diesel fuel were then subsampled and diluted with iso-octane to a concentration of 0.3% (vol.%) before the instrumental analysis to avoid instrument oversaturation.

Table B1. Solid-phase extraction (SPE) and liquid-liquid extraction (LLE) recoveries (rec.) for Naphthalene-D_8 (NAP-D_8), Acenaphthylene-D_8 (ACY-D_8), Acenaphthene-D_{10} (ACE-D_{10}), Fluorene-D_{10} (FLE-D_{10}), Phenanthrene-D_{10} (PHE-D_{10}), and Pyrene-D_{10} (PYR-D_{10}).

Parameter	NAP-D_8	ACY-D_8	ACE-D_{10}	FLE-D_{10}	PHE-D_{10}	PYR-D_{10}
SPE rec. (%)	48 ± 9%	64 ± 12%	68 ± 15%	75 ± 7%	79 ± 8%	101 ± 11%
LLE rec. (%)	35 ± 16%	44 ± 11%	49 ± 18%	52 ± 12%	74 ± 13%	88 ± 15%

Table B2. List of the identified compounds, representative surrogates, ions targeted during the GC-MS analysis and Method Detection Limits.

Compound	Representative surrogate	Quantifier	Qualifier 1	Qualifier 2	Method Detection Limit (ng L^{-1})
1,3-DEB	NAP-D$_8$	119	105	134	0.5
1,2-DEB	NAP-D$_8$	105	119	134	0.7
1,2,4,5-TeMB	NAP-D$_8$	119	134	91	1.7
1,2,3,4-TeMB	NAP-D$_8$	119	134	91	1.0
NAP	NAP-D$_8$	128	102	75	1.2
NAP-D$_8$	Surrogate	136	137	134	0.8
2-MN	NAP-D$_8$	142	141	115	0.9
1-MN	NAP-D$_8$	142	141	115	1.5
2-FB	N/A	172	170	152	1.8
ACY	ACY-D$_8$	152	150	76	1.7
ACY-D$_8$	Surrogate	160	158	80	1.5
ACE	ACE-D$_{10}$	153	154	76	2.4
ACE-D$_{10}$	Surrogate	162	164	80	1.6
2-EN/1-EN	NAP-D$_8$	141	156	115	2.0
2,6-DMN	ACE-D$_{10}$	156	141	155	2.3
2,7-DMN	ACE-D$_{10}$	156	141	155	2.7
1,3-DMN	NAP-D$_8$	156	141	155	1.9
1,7-DMN	NAP-D$_8$	156	141	155	2.4
1,6-DMN	NAP-D$_8$	156	141	155	3.2
1,4-DMN	NAP-D$_8$	156	141	155	2.5
2,3-DMN	ACE-D$_{10}$	156	141	155	1.9
1,5-DMN	ACE-D$_{10}$	156	141	155	3.7
1,2-DMN	NAP-D8	156	141	155	3.1
1,8-DMN	ACE-D$_{10}$	156	141	155	2.5
FLE	FLE-D$_{10}$	165	166	82	4.3
FLE-D$_{10}$	Surrogate	176	174	86	2.0
1,3,7-TMN	ACE-D$_{10}$	155	170	115	5.2
1,3,6-TMN	ACE-D$_{10}$	155	170	115	4.7
1,4,6-TMN	ACE-D$_{10}$	155	170	115	3.6
2,3,6-TMN	ACE-D$_{10}$	155	170	115	5.6
2,3,5-TMN	ACE-D$_{10}$	155	170	115	5.1
1,2,6-TMN	ACE-D$_{10}$	155	170	115	4.4
1,2,4-TMN	ACE-D$_{10}$	155	170	115	3.4
1,2,5-TMN	ACE-D$_{10}$	155	170	115	2.0
2,4,5-TMN	ACE-D$_{10}$	155	170	115	2.6
1,2,3-TMN	ACE-D$_{10}$	155	170	115	4.8
1,4,5-TMN	ACE-D$_{10}$	155	170	115	4.1
PHE	PHE-D$_{10}$	178	176	152	5.7
PHE-D$_{10}$	Surrogate	188	184	160	5.2
1,4,6,7-TeMN	PHE-D$_{10}$	184	169	170	7.0
1,2,5,6-TeMN	PHE-D$_{10}$	184	169	170	5.1
3-MPHE	PHE-D$_{10}$	192	191	165	6.6
2-MPHE	PHE-D$_{10}$	192	191	165	6.1
9-MPHE	PHE-D$_{10}$	192	191	165	6.3
2-MANT	PHE-D$_{10}$	192	191	165	7.5
1-MANT	PHE-D$_{10}$	192	191	165	6.9
1-MPHE	PHE-D$_{10}$	192	191	165	6.0
PYR	PYR-D$_{10}$	202	200	101	7.6
PYR-D$_{10}$	Surrogate	212	208	106	8.3
2-MPYR	PYR-D$_{10}$	216	215	108	6.1
4-MPYR	PYR-D$_{10}$	216	215	108	5.4
1-MPYR	PYR-D$_{10}$	216	215	108	7.9

Table B3. Background concentrations of aromatics (ng L^{-1}) in the microcosms and blanks.

Compound	Seawater blank concentration (ng L^{-1}) (n=13)	Control ice blank concentration (ng L^{-1}) (n=3)	Field blank concentration (ng L^{-1}) (n=12)	Laboratory blank concentration (ng L^{-1}) (n=16)
1,3-DEB	*n/d*	*n/d*	0.8	*n/d*
1,2-DEB	*n/d*	*n/d*	0.7	*n/d*
1,2,4,5-TeMB	*n/d*	*n/d*	1.1	*n/d*
1,2,3,4-TeMB	*n/d*	*n/d*	1.2	*n/d*
NAP	*n/d*	*n/d*	1.4	*n/d*
2-MN	*n/d*	*n/d*	0.6	1.5
1-MN	*n/d*	*n/d*	0.9	1.8
ACY	*n/d*	*n/d*	*n/d*	2.3
ACE	*n/d*	*n/d*	*n/d*	*n/d*
2-EN	*n/d*	*n/d*	0.5	*n/d*
1-EN	*n/d*	*n/d*	*n/d*	2.1
2,6-DMN	*n/d*	*n/d*	*n/d*	1.4
2,7-DMN	*n/d*	*n/d*	1.2	*n/d*
1,3-DMN	*n/d*	*n/d*	*n/d*	*n/d*
1,7-DMN	*n/d*	*n/d*	0.8	*n/d*
1,6-DMN	*n/d*	*n/d*	0.7	*n/d*
1,4-DMN	*n/d*	*n/d*	1.1	3.3
2,3-DMN	*n/d*	*n/d*	*n/d*	1.8
1,5-DMN	*n/d*	*n/d*	*n/d*	3.0
1,2-DMN	*n/d*	*n/d*	0.5	*n/d*
1,8-DMN	*n/d*	*n/d*	*n/d*	1.5
FLE	*n/d*	*n/d*	*n/d*	*n/d*
1,3,7-TMN	*n/d*	*n/d*	*n/d*	*n/d*
1,3,6-TMN	*n/d*	*n/d*	*n/d*	3.2
1,4,6-TMN	*n/d*	*n/d*	*n/d*	1.7
2,3,6-TMN	*n/d*	*n/d*	*n/d*	*n/d*
2,3,5-TMN	*n/d*	*n/d*	0.6	*n/d*
1,2,6-TMN	*n/d*	*n/d*	*n/d*	*n/d*
1,2,4-TMN	*n/d*	*n/d*	1.0	*n/d*
1,2,5-TMN	*n/d*	*n/d*	*n/d*	*n/d*
2,4,5-TMN	*n/d*	*n/d*	*n/d*	*n/d*
1,2,3-TMN	*n/d*	*n/d*	*n/d*	2.5
1,4,5-TMN	*n/d*	*n/d*	*n/d*	3.2
PHE	*n/d*	*n/d*	*n/d*	*n/d*
1,4,6,7-TeMN	*n/d*	*n/d*	*n/d*	*n/d*
1,2,5,6-TeMN	*n/d*	*n/d*	*0.9*	*n/d*
3-MPHE	*n/d*	*n/d*	*n/d*	*n/d*
2-MPHE	*n/d*	*n/d*	*n/d*	*n/d*
9-MPHE	*n/d*	*n/d*	*n/d*	*n/d*
2-MANT	*n/d*	*n/d*	*n/d*	*n/d*
1-MANT	*n/d*	*n/d*	*n/d*	*n/d*
1-MPHE	*n/d*	*n/d*	*n/d*	*n/d*
PYR	*n/d*	*n/d*	*n/d*	*n/d*
2-MPYR	*n/d*	*n/d*	*n/d*	*n/d*
4-MPYR	*n/d*	*n/d*	*n/d*	*n/d*
1-MPYR	*n/d*	*n/d*	*n/d*	*n/d*

n/d: not detected

Table B4. List of identified compounds and their quantitative structure-activity relationship (QSAR)-estimated physicochemical properties at 25 °C and salinity of freshwater.

Compound	Molecular weight (g mol^{-1})	Vapour pressure (mmHg)	Aqueous solubility (mg L^{-1})	Henry's Law Constant (atm m^3 mol^{-1})	$\log K_{OW}$	$\log K_{AO}$
1,3-DEB	134.2	1.30	11.1	1.16×10^{-2}	4.07	5.04
1,2-DEB	134.2	1.13	58.9	1.16×10^{-2}	4.07	4.69
1,2,4,5-TeMB	134.2	1.80×10^{-1}	33.9	7.99×10^{-3}	4.18	4.49
1,2,3,4-TeMB	134.2	4.22×10^{-1}	33.9	7.99×10^{-3}	4.18	4.49
NAP	128.2	4.66×10^{-2}	142.0	3.70×10^{-4}	3.17	4.84
2-MN	142.2	5.87×10^{-2}	41.4	5.80×10^{-4}	3.72	5.53
1-MN	142.2	6.29×10^{-2}	40.6	5.80×10^{-4}	3.72	5.55
ACY	152.2	1.12×10^{-3}	2.49	1.54×10^{-5}	3.94	6.27
ACE	154.2	1.17×10^{-3}	2.53	5.87×10^{-5}	4.15	6.04
2-EN	156.2	3.15×10^{-2}	12.9	7.71×10^{-4}	4.21	6.04
1-EN	156.2	3.06×10^{-2}	12.4	7.71×10^{-4}	4.21	5.71
2,6-DMN	156.2	4.29×10^{-3}	14.8	6.41×10^{-4}	4.26	5.89
2,7-DMN	156.2	4.29×10^{-3}	14.8	6.41×10^{-4}	4.26	5.89
1,3-DMN	156.2	2.45×10^{-2}	12.0	6.41×10^{-4}	4.26	6.03
1,7-DMN	156.2	2.33×10^{-2}	11.5	6.41×10^{-4}	4.26	6.02
1,6-DMN	156.2	2.33×10^{-2}	11.5	6.41×10^{-4}	4.26	6.02
1,4-DMN	156.2	1.90×10^{-2}	13.2	6.41×10^{-4}	4.26	6.17
2,3-DMN	156.2	3.07×10^{-3}	12.4	6.41×10^{-4}	4.26	5.83
1,5-DMN	156.2	6.04×10^{-3}	12.9	6.41×10^{-4}	4.26	6.22
1,2-DMN	156.2	1.20×10^{-2}	14.8	4.25×10^{-4}	4.26	5.84
1,8-DMN	156.2	6.04×10^{-3}	12.9	6.41×10^{-4}	4.26	6.22
FLE	166.2	2.68×10^{-4}	1.34	3.46×10^{-5}	4.02	6.19
1,3,7-TMN	170.3	8.95×10^{-3}	4.78	7.07×10^{-4}	4.81	6.35
1,3,6-TMN	170.3	4.27×10^{-3}	4.78	4.55×10^{-4}	4.81	6.35
1,4,6-TMN	170.3	4.45×10^{-3}	4.78	7.07×10^{-4}	4.81	6.35
2,3,6-TMN	170.3	4.45×10^{-3}	5.60	7.07×10^{-4}	4.81	6.27
2,3,5-TMN	170.3	3.98×10^{-3}	4.78	7.07×10^{-4}	4.81	6.35
1,2,6-TMN	170.3	8.95×10^{-3}	4.78	7.07×10^{-4}	4.81	6.35
1,2,4-TMN	170.3	4.46×10^{-3}	4.78	7.07×10^{-4}	4.81	6.35
1,2,5-TMN	170.3	3.58×10^{-3}	4.78	4.55×10^{-4}	4.81	6.35
2,4,5-TMN	170.3	4.45×10^{-3}	4.78	7.07×10^{-4}	4.81	6.35
1,2,3-TMN	170.3	2.22×10^{-3}	4.78	4.55×10^{-4}	4.81	6.35
1,4,5-TMN	170.3	4.45×10^{-3}	4.01	7.07×10^{-4}	4.81	6.44
PHE	178.2	2.28×10^{-5}	0.68	2.56×10^{-5}	4.34	7.03
1,4,6,7-TeMN	184.3	6.17×10^{-4}	1.39	7.80×10^{-4}	5.36	6.86
1,2,5,6-TeMN	184.3	6.17×10^{-4}	1.39	7.80×10^{-4}	5.36	6.86
3-MPHE	192.3	3.11×10^{-5}	0.26	2.74×10^{-5}	4.89	7.50
2-MPHE	192.3	3.11×10^{-5}	0.26	2.74×10^{-5}	4.89	7.50
9-MPHE	192.3	2.65×10^{-5}	0.25	2.74×10^{-5}	4.89	7.53
2-MANT	192.3	2.65×10^{-6}	0.20	2.74×10^{-5}	4.89	6.59
1-MANT	192.3	2.65×10^{-6}	0.25	2.74×10^{-5}	4.89	7.53
1-MPHE	192.3	1.29×10^{-5}	0.17	2.74×10^{-5}	4.89	7.53
PYR	202.3	6.77×10^{-8}	0.23	2.94×10^{-6}	4.93	8.19
2-MPYR	216.3	4.99×10^{-7}	0.06	3.15×10^{-6}	5.48	8.19
4-MPYR	216.3	4.99×10^{-7}	0.06	3.15×10^{-6}	5.48	8.19
1-MPYR	216.3	4.99×10^{-7}	0.06	3.15×10^{-6}	5.48	8.19

Table B5. Average sea ice thickness and ice growth rate during the experiment.

	Ice formation (Feb 19)	Day 0 (Feb 24)	Day 3a	Day 3b	Day 5	Day 8	Day 15
Average ice thickness (cm)	0	15.0	29.8	30.3	31.8	41.3	47.8
Average ice growth rate (cm day^{-1})	0	3.0	4.9	5.1	0.5	3.2	0.9

Table B6. Mean and standard deviations (n = 4) total volume of diesel fuel and mass of total aromatics (m_{TAHs}) mass in the microcosms throughout the study. Day 0 represents the day of diesel injection.

Day	Diesel fuel (mL)	m_{TAHs} (mg)
0	100	963.6
3a	93 ± 18	916 ± 57
3b	91 ± 20	901 ± 43
5	86 ± 24	844 ± 70
8	82 ± 15	714 ± 30
15	68 ± 12	480 ± 27

Table B7. 95% confidence intervals (CI) for the multiple linear regression coefficients determined for the equations predicting the relative fractions of the 46 aromatic hydrocarbons from their respective octanol-water partition coefficient (K_{OW}) and Henry's Law Constant (K_H) values.

Date	**Coefficient**	**Microcosm compartments**									
		Loss CI		**Top CI**		**Middle CI**		**Bottom**		**Water**	
		Lower 95%	**Upper 95%**	**Lower 95%**	**Upper 95%**	**Lower 95%**	**Upper 95%**	**Lower 95%**	**Upper 95%**	**Lower 95%**	**Upper 95%**
Day 3	b_0	0.090	0.176	0.260	0.432	0.099	0.313	0.176	0.322	0.040	0.092
	b_1	–0.026	–0.004	–0.033	–0.003	0.050	0.103	–0.053	–0.017	–0.014	–0.002
	b_2	0.005	0.017	0.025	0.048	–0.068	–0.039	–0.009	–0.001	**–0.002**	**0.000**
Day 5	b_0	0.246	0.396	0.277	0.574	–0.385	–0.161	0.260	0.480	0.097	0.216
	b_1	–0.054	–0.018	–0.039	–0.005	0.109	0.164	–0.085	–0.031	–0.034	–0.005
	b_2	0.014	0.034	0.030	0.070	–0.100	–0.070	–0.012	–0.002	**–0.011**	**0.005**
Day 8	b_0	0.459	0.820	–0.235	0.055	–0.276	–0.079	0.163	0.373	0.256	0.473
	b_1	–0.114	–0.025	–0.114	–0.043	0.057	0.106	–0.065	–0.013	–0.078	–0.025
	b_2	0.030	0.078	0.001	0.013	–0.088	–0.061	–0.012	–0.001	**–0.023**	**0.006**
Day 15	b_0	0.971	1.476	–0.354	–0.106	–0.905	–0.670	0.099	0.292	0.449	0.761
	b_1	–0.179	–0.055	0.044	0.104	0.126	0.184	–0.050	–0.002	–0.125	–0.048
	b_2	0.083	0.150	–0.052	–0.019	–0.111	–0.080	**–0.013**	**0.012**	**–0.037**	**0.005**

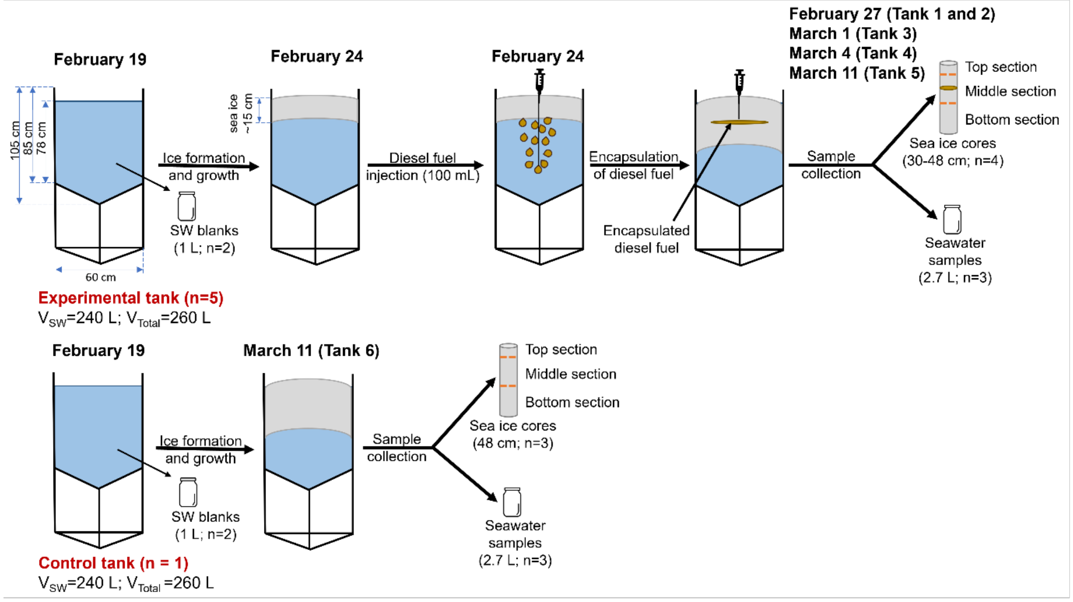

Figure B1. Schematic of the experimental design, key steps of the study and sample collection protocol.

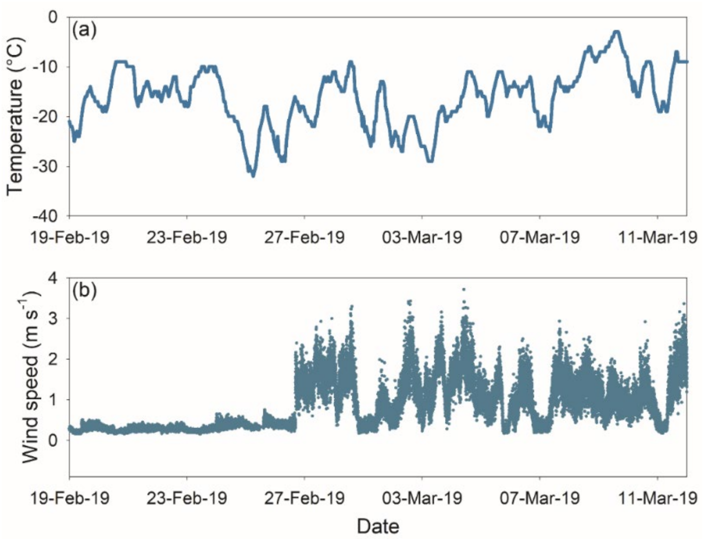

Figure B2. Variabilities of the ambient air temperature retrieved from the Winnipeg International Airport meteorological station (a) and *in situ* wind speed throughout the experiment (b), as measured at 1.5 m above the ground.

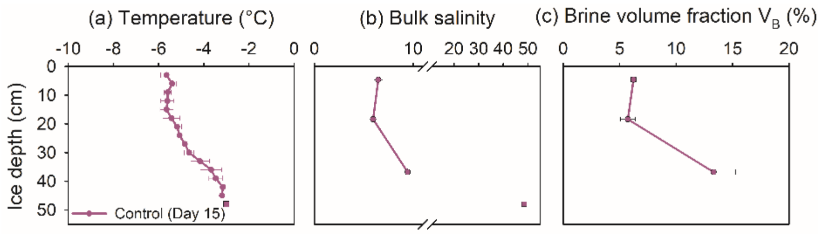

Figure B3. Vertical profiles of temperature (a), bulk salinity (b), and brine volume fraction (c) throughout the sea ice column (circle symbols) and in the underlying seawater (square symbols) in the control microcosm. The value of 0 on the y-axis corresponds to the air-ice interface.

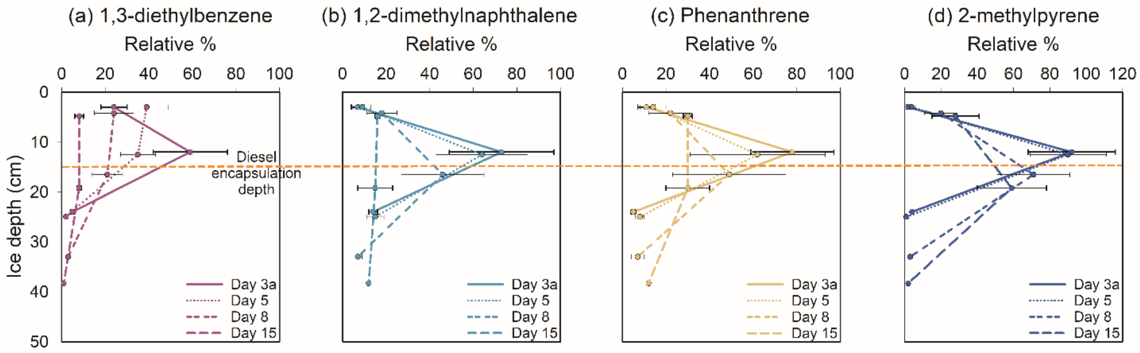

Figure B4. Vertical distribution profiles of 1,3-diethylbenzene (a), 1,2-dimethylnaphthalene (b), Phenanthrene (c) and 2-methylpyrene (d) in the ice throughout the study. Relative % values of each compound were estimated relative to the initial amounts of each compound on day 0.

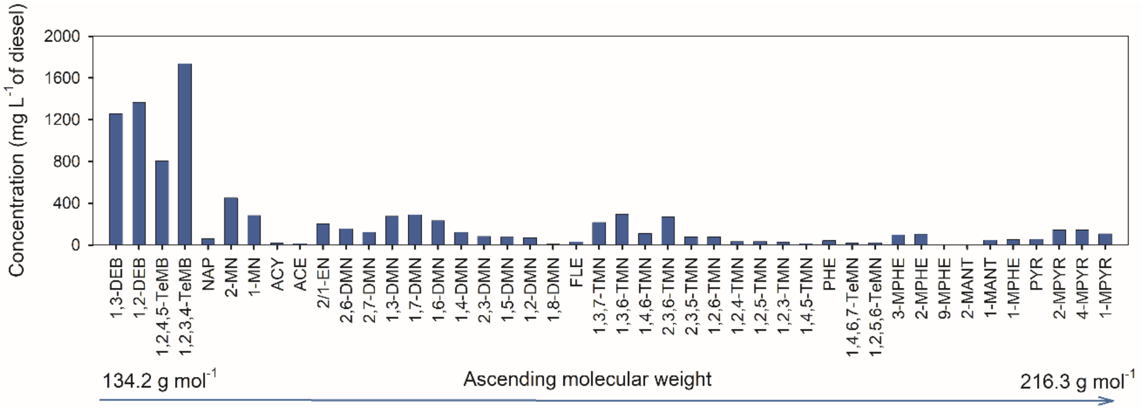

Figure B5. Chemical composition profile of the studied aromatic hydrocarbons in fresh diesel fuel.

Appendix C

Supporting information for Chapter 4

Table of Contents

Table C1. Analytical method acquisition parameters.

Method name	Type of samples	Injection volume (mL)	Injection mode	Calibration concentration range (ng mL^{-1})	Limit of quantification (ng L^{-1})
M1 (Oily samples)	Sea ice core samples with visible oil	0.25	Split mode 100:1	3.9–2000	4.1–6.8
M2 (Clean samples)	Sea ice core samples without visible oil Brine samples Surface ice samples*	1.25	Splitless	0.5–1000	0.8–1.7

** Surface ice samples were not quantified in this study*

Table C2. List of the monitored compounds and ions targeted during the instrumental analysis with selected ion monitoring mode.

Compound	Quantifier	Qualifier 1	Qualifier 2
IS	84	52	56
EB	91	106	77
m-X	91	106	105
p-X	91	106	105
o-X	91	106	105
iso-PB	105	120	77
n-PB	91	120	92
3-ET	105	120	91
4-ET	105	120	91
1,3,5-TMB	105	120	119
2-ET	105	120	91
1,2,4-TMB	105	120	119
1,2,3-TMB	105	120	119
sec-BB	105	132	91
1,3-DEB	119	105	134
n-BB	91	92	134
1,4-DEB	119	105	134
1,2-DEB	105	119	134
1,2,4,5-TeMB	119	134	91
1,2,3,5-TeMB	119	134	91
2-MN	142	141	115
1-MN	142	141	115
2-EN	141	156	115
1-EN	141	156	115
2,6-DMN	156	141	155
2,7-DMN	156	141	155
1,8-DMN	156	141	155
1,3-DMN	156	141	155
1,7-DMN	156	141	155
1,6-DMN	156	141	155
2,3-DMN	156	141	155
1,4-DMN	156	141	155
1,5-DMN	156	141	155
1,3,7-TMN	170	155	169
2,3,6-TMN	170	155	169
1,4,6-TMN	170	155	169
1,4,5-TMN	170	155	169
2,4,5-TMN	170	155	169
2,3,5-TMN	170	155	169
1,2,6-TMN	170	155	169
1,2,4-TMN	170	155	169
1,4,6,7-TeMN	184	169	170
1,2,5,6-TeMN	184	169	170

Table C3. List of identified compounds and their quantitative structure-activity relationship (QSAR)-estimated physicochemical properties at 25 °C and salinity of freshwater.

Compound	Molecular weight (g mol^{-1})	Vapour pressure @ 25 °C (mmHg)	Aqueous solubility @ 25 °C (mg L^{-1})	Henry's Law Constant @ 25 °C (atm m^3 mol^{-1})	log K_{OW} @ 25 °C	log K_{AO} @ 25 °C
EB	106.2	9.83	229.0	7.89×10^{-3}	3.03	3.52
p-X	106.2	8.96	229.0	6.56×10^{-3}	3.09	3.66
m-X	106.2	8.62	207.0	6.56×10^{-3}	3.09	3.66
o-X	106.2	8.85	224.0	6.56×10^{-3}	3.09	3.83
Iso-PB	120.2	4.79	75.0	1.05×10^{-2}	3.45	3.99
n-PB	120.2	3.53	70.7	1.05×10^{-2}	3.52	4.06
4-ET	120.2	3.21	40.0	8.71×10^{-3}	3.58	4.43
3-ET	120.2	3.21	40.0	8.71×10^{-3}	3.58	4.03
1,3,5-TMB	120.2	2.75	120.0	7.24×10^{-3}	3.63	3.87
2-ET	120.2	2.69	96.9	8.71×10^{-3}	3.58	4.18
1,2,4-TMB	120.2	2.23	79.6	7.24×10^{-3}	3.63	4.23
1,2,3-TMB	120.2	1.63	75.0	7.24×10^{-3}	3.63	4.41
sec-BB	134.2	1.84	11.1	1.39×10^{-2}	3.94	4.71
1,3-DEB	134.2	1.30	11.1	1.16×10^{-2}	4.07	5.04
n-BB	134.2	1.17	16.1	1.39×10^{-2}	4.01	4.57
1,4-DEB	134.2	1.30	10.8	1.16×10^{-2}	4.07	5.09
1,2-DEB	134.2	1.13	58.9	1.16×10^{-2}	4.07	4.69
1,2,4,5-TeMB	134.2	1.80×10^{-1}	33.9	7.99×10^{-3}	4.18	4.49
1,2,3,4-TeMB	134.2	4.22×10^{-1}	33.9	7.99×10^{-3}	4.18	4.49
2-MN	142.2	5.87×10^{-2}	41.4	5.8×10^{-4}	3.72	5.53
1-MN	142.2	6.29×10^{-2}	40.6	5.8×10^{-4}	3.72	5.55
2-EN	156.2	3.15×10^{-2}	12.9	7.71×10^{-4}	4.21	6.04
1-EN	156.2	3.06×10^{-2}	12.4	7.71×10^{-4}	4.21	5.71
2,6-DMN	156.2	4.29×10^{-3}	14.8	6.41×10^{-4}	4.26	5.89
2,7-DMN	156.2	4.29×10^{-3}	14.8	6.41×10^{-4}	4.26	5.89
1,8-DMN	156.2	6.04×10^{-3}	12.9	6.41×10^{-4}	4.26	6.22
1,3-DMN	156.2	2.45×10^{-2}	12.0	6.41×10^{-4}	4.26	6.03
1,7-DMN	156.2	2.33×10^{-2}	11.5	6.41×10^{-4}	4.26	6.02
1,6-DMN	156.2	2.33×10^{-2}	11.5	6.41×10^{-4}	4.26	6.02
2,3-DMN	156.2	3.07×10^{-3}	12.4	6.41×10^{-4}	4.26	5.83
1,4-DMN	156.2	1.9×10^{-2}	13.2	6.41×10^{-4}	4.26	6.17
1,5-DMN	156.2	6.04×10^{-3}	12.9	6.41×10^{-4}	4.26	6.22
1,3,7-TMN	170.3	8.95×10^{-3}	4.78	7.07×10^{-4}	4.81	6.35
2,3,6-TMN	170.3	4.45×10^{-3}	5.60	7.07×10^{-4}	4.81	6.27
1,4,6-TMN	170.3	4.45×10^{-3}	4.78	7.07×10^{-4}	4.81	6.35
1,4,5-TMN	170.3	4.45×10^{-3}	4.01	7.07×10^{-4}	4.81	6.44
2,4,5-TMN	170.3	4.45×10^{-3}	4.78	7.07×10^{-4}	4.81	6.35
2,3,5-TMN	170.3	3.98×10^{-3}	4.78	7.07×10^{-4}	4.81	6.35
1,2,6-TMN	170.3	8.95×10^{-3}	4.78	7.07×10^{-4}	4.81	6.35
1,2,4-TMN	170.3	4.46×10^{-3}	4.78	7.07×10^{-4}	4.81	6.35
1,4,6,7-TeMN	184.3	1.40×10^{-3}	1.39	7.80×10^{-4}	5.36	6.86
1,2,5,6-TeMN	184.3	1.40×10^{-3}	1.39	7.80×10^{-4}	5.36	6.86

Table C4. Average ice thickness and ice growth rate throughout the experiment.

Parameter	Ice formation (January 8)	Oil injection (January 23; day 0)	Sampling 1 (day 15)	Sampling 2 (day 34)	Sampling 3 (day 52)	Sampling 4 (day 77)
Average ice thickness (cm)	0	25	37.8 ± 1.9	49.3 ± 2.1	51.0 ± 0.1	22.5 ± 9.2
Average ice growth rate (cm day^{-1})	0	1.7	0.9 ± 0.2	0.6 ± 0.1	0.1 ± 0.1	–1.1 ± 0.4*

**Average ice decay rate (cm day^{-1})*

Table C5. 95% confidence intervals (CI) for the multiple linear regression coefficients determined for the equations predicting the R_{TM} and R_{BM} ratios of the 39 aromatic hydrocarbons from their respective octanol-water partition coefficient (K_{OW}) and Henry's Law Constant (K_H) values:

$$R_{XM} = b_0 + b_1 log\ K_{OW} + b_2 log\ K_H$$

where insignificant variable coefficients are displayed in bold.

Ratio	**Date**	**Coefficient**	**CI**		**Ratio**	**Date**	**Coefficient**	**CI**	
			Lower 95%	**Upper 95%**				**Lower 95%**	**Upper 95%**
R_{TM}	Day 15	b_0	–5.662	–1.002	**R_{BM}**	Day 15	b_0	–0.570	0.447
		b_1	0.252	1.711			b_1	–0.480	–0.178
		b_2	–5.134	–3.653			b_2	–0.874	–0.586
	Day 34	b_0	–10.980	–8.145		Day 34	b_0	–45.774	17.464
		b_1	0.902	1.790			b_1	–2.319	–0.830
		b_2	–3.282	–2.382			**b_2**	**–11.559**	**6.566**
	Day 52	b_0	–7.799	–4.733		Day 52	b_0	–55.358	–33.185
		b_1	1.066	2.026			b_1	–3.149	–0.063
		b_2	–1.107	–0.133			b_2	–28.553	–21.409
	Day 77	b_0	–60.593	26.566		Day 77	b_0	–7.801	12.445
		b_1	1.333	3.388			**b_1**	**–0.226**	**0.251**
		b_2	–5.198	–0.218			**b_2**	**–2.460**	**3.326**

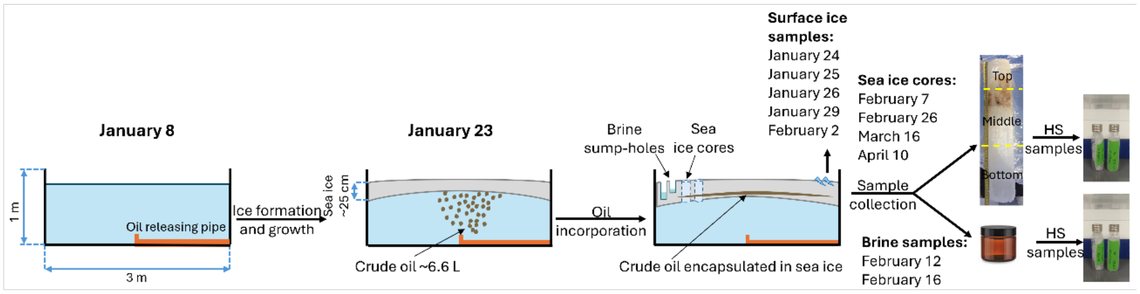

Figure C1. Schematic of the experimental design, the key steps of the study and the sample collection plan.

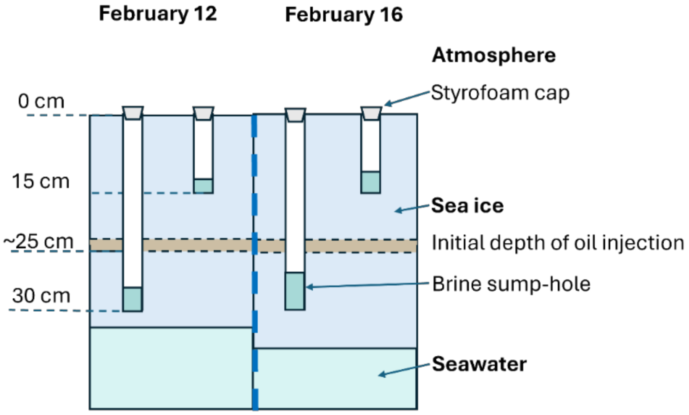

Figure C2. Schematic of brine sampling using a sump-hole technique. Note that the sump-holes were not directly drilled above or below the oil lens due to heterogeneity in oil encapsulation.

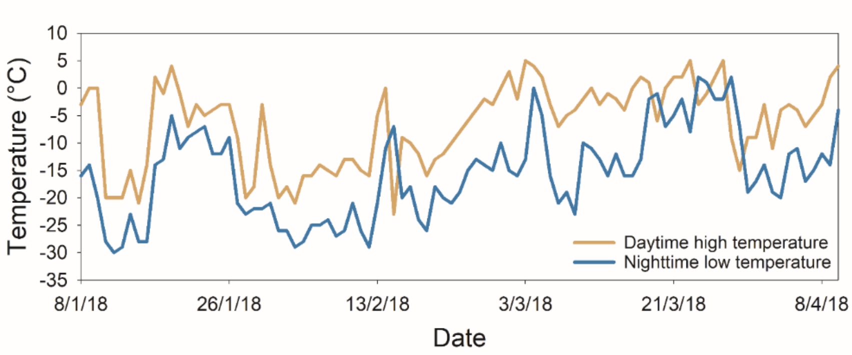

Figure C3. Ambient air temperature during the experiment (data retrieved from the Winnipeg International Airport meteorological station).

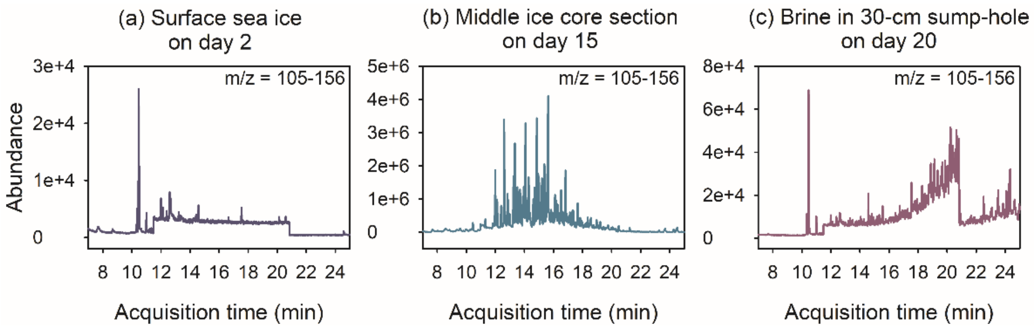

Figure C4. Example chromatograms of a representative surface sea ice sample (a), middle ice core section sample (b), and brine sample (c).

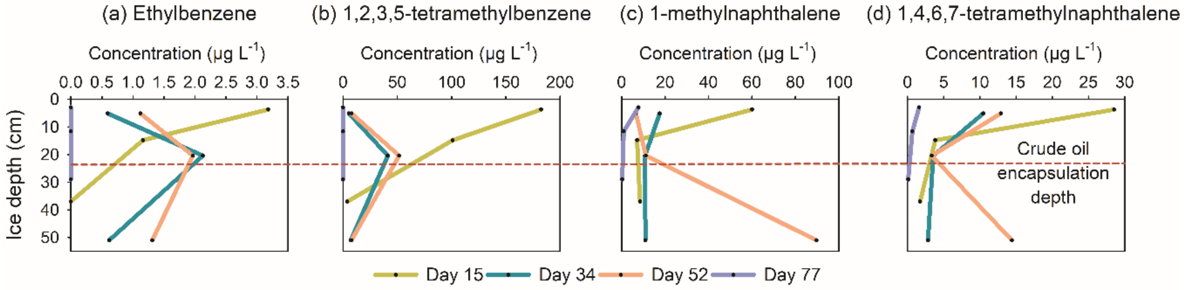

Figure C5. Vertical distribution concentration profiles of ethylbenzene (a), 1,2,3,5-tetramethylbenzene (b), 1-methylnaphthalene (c) and 1,4,6,7-tetramethylnaphthalene (d) in young experimental sea ice.

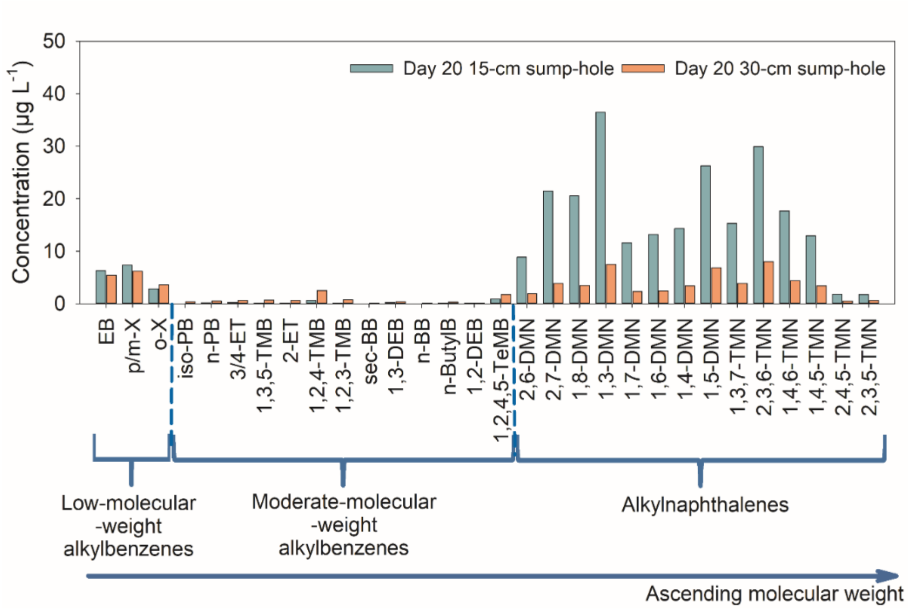

Figure C6. Concentrations of the studied aromatics in the brine samples collected on day 20.

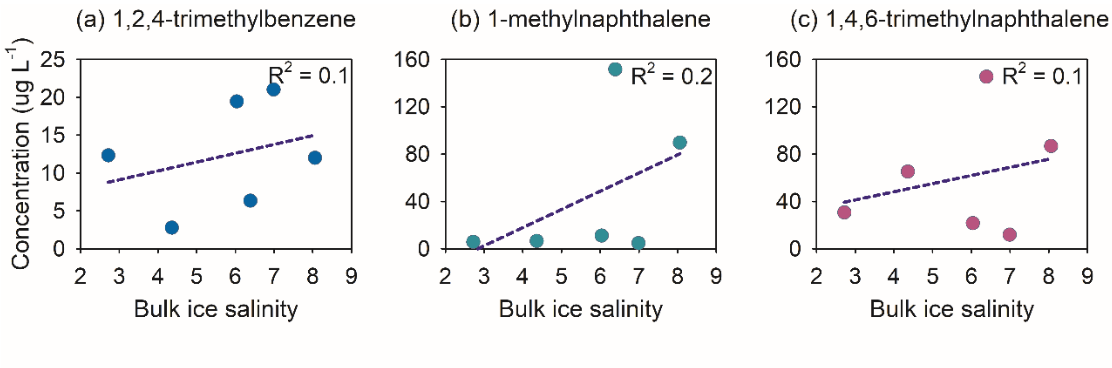

Figure C7. Relationship between the bulk ice salinity and the concentrations (µg L^{-1}) of three representative aromatic compounds: 1,2,4-trimethylbenzene (a), 1-methylnaphthalene (b), and 1,4,6-trimethylnaphthalene (c) on day 52 in young experimental sea ice.